2011-04-21

Three-Dimensional Numerical Simulations of Liquid Laminar Flow Over Superhydrophobic Surfaces with Post Geometries

Abolfazl Amin
Brigham Young University - Provo

Three-Dimensional Numerical Simulations of Liquid Laminar Flow over Superhydrophobic Surfaces with Post Geometries

Abolfazl Amin

A dissertation submitted to the faculty of
Brigham Young University
in partial fulfillment of the requirements for the degree of

Doctor of Philosophy

R. Daniel Maynes, Chair
Brent W. Webb
Julie C. Vanderhoff
Ken A. Solen
Aaron R. Hawkins

Department of Mechanical Engineering

Brigham Young University

June 2011

ABSTRACT

Three-Dimensional Numerical Simulations of Liquid Laminar Flow over Superhydrophobic Surfaces with Post Geometries

Abolfazl Amin

Department of Mechanical Engineering, BYU
Doctor of Philosophy

Frictional resistance reduction of liquid flow over surfaces has recently become a more important topic of research in the field of fluid dynamics. Scientific and technological progress and continued interest in nano and micro-technology have required new developments and approaches related to reducing frictional resistance, especially in liquid flow through nano and micro-channels. The application of superhydrophobic surfaces could be very effective in achieving the desired flow through such small channels. Superhydrophobic surfaces are created by intentionally creating roughnesses on the surface and applying a uniform hydrophobic coating to the entire surface. Liquid droplet tests have revealed that because of the trapped air within the cavities such surfaces could have contact angles as high as 179º. Such a property gives superhydrophobic surfaces liquid repelling characteristics making them very suitable for frictional resistance reduction in liquid flow through nano or micro-channels, provided wetting of the cavities could be avoided. This study presents 3-D numerical simulation results of liquid laminar flow over post patterned superhydrophobic surfaces. The research was performed in three phases, 1) pressure-driven flow with square micro-posts, 2) Couette flow with square micro-posts, and 3) pressure-driven flow with rectangular micro-posts at various aspect ratios. In phases (1) and (2) the influences of important parameters such as the cavity fraction, in the range of 0.0-0.9998, and the relative module width, from 0.01 to 1.5, on frictional resistance reduction in the creeping flow regime were explored. Phase (1) also addressed the effect of varying Reynolds number from 1 to 2500 on frictional resistance. Phase (3) was conducted for aspect ratios of 1/8, 1/4, 1/2, 2, 4, and 8 also in the creeping flow regime.

The obtained results suggest that important parameters such as cavity fraction (relative area of the cavities), relative module width (combined post and cavity width relative to the channel hydraulic diameter), and the Reynolds number have great influence on the frictional resistance reduction. For pressure-driven flow at cavity fraction 0.9998, reductions as high as 97% in the frictional resistance were predicted compared with the classical channel flow. This reduction is directly related to the significant reduction in liquid-solid contact area. With respect to the effect of relative module width on the overall frictional resistance, a reduction of 93% in the frictional resistance was observed as the relative module width was increased from 0.1 to 1.5. This is indicative of the importance of the relative spacing size of the posts/cavities compared to the channel size in micro-channel liquid flow. The overall frictional resistance for post-patterned superhydrophobic surfaces was found to be independent of the Reynolds number up to a value of nominally 40 after which the non-dimensional frictional resistance increased at high values of the Reynolds number. However, at very high cavity fractions the frictional resistance was independent of Reynolds number only up to about 4.

When the driving mechanism was a Couette flow, similar to the pressure-driven flow, as the cavity fraction and the relative module width increased the frictional resistance on the superhydrophobic surface decreased. At a cavity fraction of 0.9998 the reduction in the non-dimensional frictional resistance was approximately 96%, which was only 1% different from the similar pressure-driven scenario. However, a more significant difference was observed between the slip velocities for the two flow types, and it was determined that the pressure-driven flow resulted in greater apparent slip velocities than Couette flow. A maximum difference in normalized slip between the two scenarios of approximately 20% was obtained at relative module width 0.1 and Reynolds number 1.

Results for superhydrophobic surfaces with rectangular micro-posts approached those reported in the literature for micro-ribs as the aspect ratio of the posts increased. When the flow was perpendicular to the long side of the posts, and as the aspect ratio increased, the frictional resistance approached previously published transverse rib results. Similarly, when the liquid flow direction was parallel to the long side of the posts, the frictional resistance results also approached those of the previously published longitudinal ribs as the aspect ratio increased.

Keywords: Abolfazl Amin, superhydrophobic, post, friction reduction

ACKNOWLEDGEMENTS

With my heart full of gratitude to our Lord and creator for granting me the required strength, health, and stamina to pursue my childhood dream and goal, to fulfill the rigorous and demanding requirements, and to successfully complete such a great task while accepting the responsibility of a full-time employment; I would like to sincerely express my utmost appreciation to my wonderful advisors, teachers, mentors, and friends Dr. Maynes and Dr. Webb for their unforgettable cooperation and extremely valuable guidance throughout my graduate studies and education. It was an honor for me to be able to work with such talented and intelligent individuals. The genuine care and helpful direction provided by my committee members throughout this research deserve to be recognized and sincerely appreciated. Words cannot express how thankful I am to the great institution, BYU, and the fantastic department of Mechanical Engineering for providing a superb environment and opportunity for students like me to obtain an invaluable and high quality education. I will never forget my great and wonderful professors at BYU and will always admire their unselfish service and sacrifice to this amazing university. Some have retired and a few have passed away, but it is appropriate for me at this time to thank Drs. Heaton, Chase, Ulrich, Willie, Smith, and Polve. I don't know how to thank the department graduate advisor Miriam Busch for her kindness, efficiency, and the unimaginable assistance she provides students with. I would also like to thank Claire DeWitt at the graduate school and Mr. Jensen at the library for their patience with me and their willingness to listen and help me whenever possible. This work could not have been possible without the assistance of Lloyd Brown and Ryan Cox in the Supercomputer Lab and Dean Anderson at the CAEDM Lab as I spent long hours behind computers and sought their assistance and experience regularly. Although my entire education has required a lot of commitment and hard work,

without the help of these wonderful individuals it would have been impossible. Finally, I would like to dedicate this work to my lovely family. I am very grateful to them for the moral support and words of encouragement they have always given me. Such persons make life even more meaningful. Thank you!! Go Cougars!!

"What we are is God's gift to us. What we become is our gift to God."

Eleanor Powell

TABLE OF CONTENTS

LIST OF TABLES

LIST OF FIGURES

NOMENCLATURE

Symbol	Definition
A_c	Projected cavity surface area
A_s	Projected post surface area
A	Total projected surface area $A = A_c + A_s$
A_R	Aspect ratio
A_{cs}	Cross sectional area
A_{cr}	Cross sectional area for the computational domain
C_f	Fanning friction factor
D	Surface drag force
D_h	Hydraulic diameter
d	Cavity depth
F_c	Cavity fraction
F_s	Solid fraction
F_{shear}	Shear force
f_r	Contact area fraction
f	Darcy friction factor
fRe	Friction factor-Reynolds number product
H	Channel height
$\dot{m}$	Mass flow rate
P_w	Liquid static pressure
P_a	Vapor static pressure
ΔP	Stramwise pressure difference
Δp	Liquid-vapor pressure difference
p_{cs}	Wetted perimeter for the cross sectional area
R_c	Cavity width ratio
R_s	Solid width ratio
Re	Reynolds number
Re_c	Couette flow Reynolds number
Re_w	Width based Reynolds number
t	Time
u	Streamwise velocity (x-direction)
u_s	Slip velocity
$\bar{U}$	Area-weighted average streamwise velocity
U	Plate velocity in Couette flow
U_m	Mean velocity in Couette flow

v	Wall normal velocity (y-direction)
w	Transverse velocity (z-direction)
W_c	Cavity width
W_s	Solid (post) width
W	Total width $W = W_s + W_c$
W_m	Relative module width
W_{ch}	Channel width
θ	Contact angle
θ_{CB}	Cassie-Baxter contact angle
μ	Fluid viscosity
ν	Kinematic viscosity
ρ	Fluid density
$\dot{\gamma}$	Strain rate
γ_{sl}	Solid-liquid interface energy
γ_{sg}	Solid-gas interface energy
γ_{gl}	Gas-liquid interface energy
λ	Apparent slip length
τ	Shear stress
τ_w	Wall shear stress
τ_w	Average wall shear stress
φ	Meniscus angle
σ	Surface tension

1 INTRODUCTION

In channel flow, frictional resistance or drag reduction is of primary concern. Common knowledge in fluid mechanics indicates that for 2-D planar channel flow the pressure drop is inversely proportional to the third power of the hydraulic diameter. Therefore, in situations where length scales are very small such as micro- or nano-channel scenarios significant pressure drop is required. One solution is to reduce the frictional resistance by using superhydrophobic surfaces for channel walls. In order to explain the details of the research described here on micro-posts and their effects on frictional resistance reduction in liquid laminar micro-channel flow, it is important to present an overview of the nature of the problem with a brief introduction of some engineering and scientific solutions. This chapter provides the motivation and background related to the application of superhydrophobic surfaces in micro- and nano-channel flows, includes a brief explanation of friction in channel flow for Newtonian fluids, defines superhydrophobic surfaces and some important parameters, and describes the wetting and non-wetting conditions. At the end, the contributions of this study and a list of the topics covered in the remaining chapters are included.

1.1 Background and Motivation

Advancement of micro- and nano-scale technology has recently sparked a great deal of interest in the development of superhydrophobic surfaces in the area of fluid mechanics. Examples of the need for such surfaces are found in Micro-Electro-Mechanical-Systems

(MEMS), Nano-Electro-Mechanical-Systems (NEMS), water repellant materials, and liquid flow through micro-channels. The behavior of lotus leaves and rose petals with water droplets can be explained by the physics behind superhydrophobic surfaces.

For liquid flow in micro- or nano-channels, due to increases in frictional resistance with a decrease in channel size, large driving forces or applied pressures are required. In such small-scale applications superhydrophobic surfaces can provide, if the right conditions are met, reduced overall frictional resistance. Therefore, it is important to better understand the influence that certain conditions and parameters have on hydrophobicity and frictional resistance of surfaces in micro- or nano-fluidic flows.

The primary objective of this research is to numerically examine the effects of important parameters on surface friction for laminar flow of liquids over superhydrophobic surfaces exhibiting post type patterning on the channel walls. For validation purposes the results will be compared with previously published data obtained by other researchers for micro-ribs. The results of this work will be of use to others in the field of superhydrophobic surfaces.

1.2 Friction in Laminar Channel Flow

For fully developed liquid laminar flow in channels the shear stress varies linearly from a maximum at the wall surface to zero at the channel centerline, due to the high velocity gradient that prevails near the channel wall surface. In classical continuum flow the liquid has to attain the same velocity as the wall without slipping. This condition is referred to as the no-slip condition. For a flow with a single velocity component the shear stress within a Newtonian fluid is defined as:

$$\tau = \mu \frac{du}{dy} \tag{1.1}$$

In this equation τ is the shear stress, μ is the fluid viscosity, u is the streamwise velocity, and y is the spatial variable normal to the streamwise direction. At the fluid-solid interface region this shear stress exerts a tangential force on the contacting surface and according to Newton's third law of motion the surface also exerts an equal and opposite shearing force on the fluid. This force is referred to as frictional resistance or drag and it is calculated by integrating the wall shear stress over the wall area in question from the following relation:

$$D = \int \tau dA = \int \mu \frac{du}{dy} dA \tag{1.2}$$

where D is the surface drag force or friction, τ_s is the shear stress at the surface acting over a differential fluid-solid surface contact area, dA. From Eq. 1.2 the surface friction can be reduced by decreasing the fluid viscosity, the velocity gradient, or the fluid-solid surface contact area. Of these three factors only reducing the fluid-solid contact area is practical for most applications.

For highly viscous flow and small-scale channels where large driving forces or high pressure gradients are required to deliver a volume of fluid, reduction of frictional resistance is very desirable. Theory shows that the pressure difference across a given length of 2-D parallel plate laminar flow is inversely proportional to the third power of channel hydraulic diameter. Thus, as the channel decreases in size the required pumping pressure increases significantly. As mentioned above, a reduction in frictional force leading to the pumping pressure can be achieved by reducing the total fluid-solid contact area at the channel walls.

1.3 Hydrophilic, Hydrophobic, and Superhydrophobic Surfaces

The natural shape of liquid droplets on a solid substrate is due to the strong cohesive forces between the liquid molecules. These cohesive forces acting between molecules on the surface of a liquid droplet are referred to as surface tension. In the absence of gravity or for very small droplets, this force pulls the liquid into a spherical shape which minimizes the surface area. Considering the energy aspect, droplets naturally minimize their surface energy by assuming a spherical feature. A liquid droplet resting on a solid surface makes a specific angle with the surface at the point of contact. This angle which is referred to as the contact angle, θ, is defined in Fig. # 1.1.

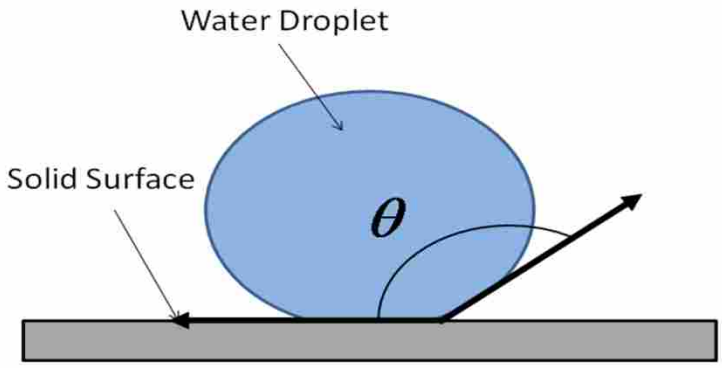

Figure 1.1: Illustration of the contact angle a liquid droplet attains on a solid surface.

The magnitude of the contact angle depends on the physical characteristics of the surface and properties and the state of the liquid and the gas involved. Young was able to derive a relationship for the contact angle in terms of three interfacial energies namely the solid-liquid, γ_{sl}, solid-gas, γ_{sg}, and liquid-gas, γ_{gl} surface energies [1]. At equilibrium this relationship is expressed as:

$$\cos\theta = \frac{\gamma_{sg} - \gamma_{sl}}{\gamma_{gl}} \tag{1.3}$$

This is referred to as Young's equation. Surfaces can be classified as hydrophilic, hydrophobic, or superhydrophobic and the contact angle of a water droplet on a surface is used as a measure of hydrophobicity. Fig. # 1.2 illustrates hydrophilic (wetted), hydrophobic, and superhydrophobic surfaces.

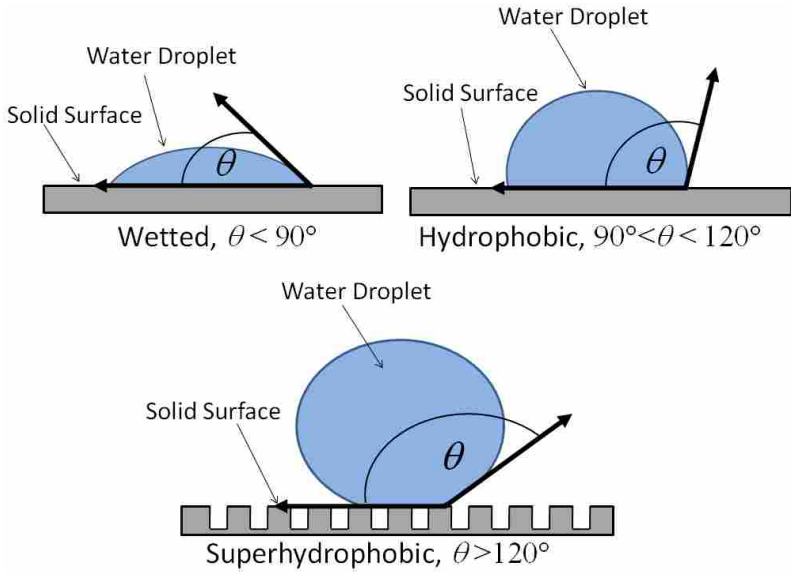

Figure 1.2: Schematic illustration of the contact angle for hydrophilic, hydrophobic, and superhydrophobic liquid-gas-solid surfaces.

A water droplet on a hydrophilic surface wets the surface and resembles the first illustration on the left in Fig. # 1.2 where angle θ is smaller than 90°. On a hydrophilic surface a water droplet wets the surface and spreads out because the adhesive forces between the droplet and the surface are higher than its internal cohesive forces. The amount of wetting is characterized in terms of the contact angle, θ. Treating a surface with a hydrophobic coating can reduce the wettability of the surface and change it to a hydrophobic one as shown in the top right hand corner of the figure. The higher the contact angle, greater than 90°, the higher the degree of

hydrophobicity. Carefully patterning a solid surface, or making it rougher, and applying a hydrophobic coating, trapping gas in the cavities, and preventing liquid from entering the cavities can produce a superhydrophobic surface as presented on the bottom of Fig. # 1.2. The contact angle for such a surface is sometimes referred to as the Cassie-Baxter angle, θ_{CB}. An ultra- or superhydrophobic surface is a surface that provides a contact angle, θ, greater than 120° for a liquid droplet. An example of a superhydrophobic surface is a hydrophobically coated and carefully structured or patterned surface. On a hydrophobic surface the adhesive forces between the liquid and the solid surface are reduced and the droplet exhibits a much higher contact angle than on a hydrophilic surface.

As explained previously, fluid flow through micro- and nano-channels requires large driving pressure forces. A particular solution for overcoming this difficulty is by reducing the frictional resistance. Recent progress in research and development of fluid systems in MEMS and NEMS has resulted in a greater need for the production of superhydrophobic surfaces. One way to make a superhydrophobic surface is by carefully etching away part of the solid surface, creating patterns or structures such as ribs or posts. Subsequently, the solid surface is coated with a hydrophobic solution. A review of the literature indicates that the amount of frictional resistance reduction depends on several important factors. These include surface geometry, nature of the flow (laminar or turbulent), and whether the liquid enters (wets) the cavities or not.

A SEM picture of a micro-engineered surface created in the microfabrication facility at Brigham Young University is shown in Fig. # 1.3(b), [2]. The ribs have a width of 4 μm, a height of 25 μm, and a rib spacing of 36 μm. These ribs were etched directly into the silicon substrate using the Deep Reactive Ion Etching (DRIE) process.

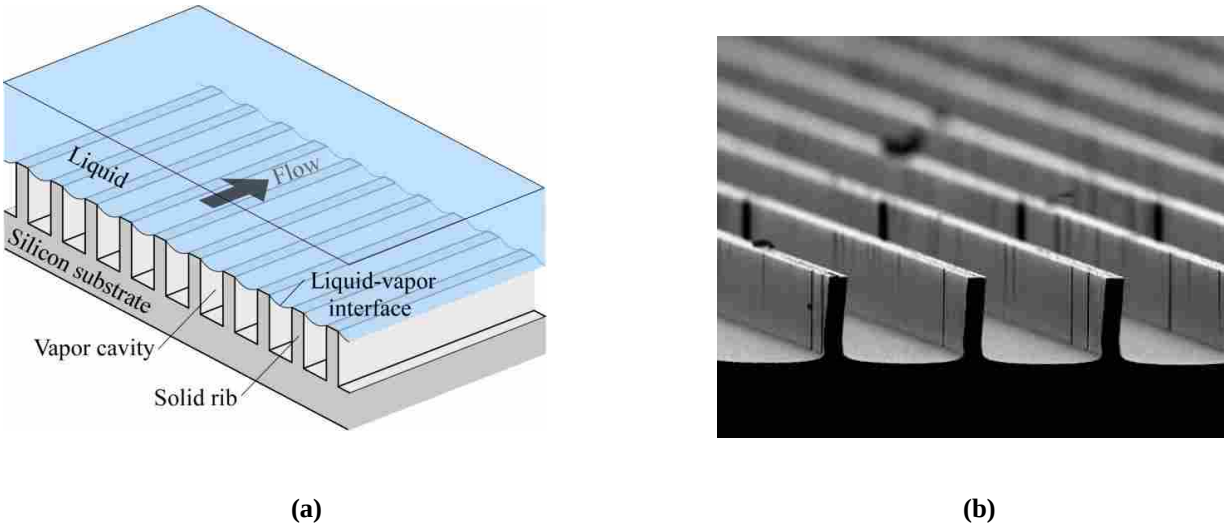

(a) **(b)**

Figure 1.3 (a) Schematic diagram illustrating a superhydrophobic surface exhibiting micro-ribs oriented longitudinal to the liquid flow direction, (b) SEM image of a micro-fabricated surface.

Previous works have shown that for the case of continuously flowing liquid through a micro-channel a superhydrophobic surface can result in reduced wettability and frictional resistance. By trapping air in cavities and preventing liquid from entering the cavities in a systematic and controlled manner as shown in Fig. # 1.3(a) both the frictional resistance and the required pressure drop can be greatly reduced. In this situation no-slip and slip flow conditions exist at the liquid-solid and liquid-air interfaces, respectively, if wetting of the cavities is avoided.

On a superhydrophobic surface the contact angle, θ_{CB}, is an apparent contact angle since some amount of gas, usually air, trapped in cavities also supports the droplet. This results in reduced liquid-solid surface energy causing the droplet to attain an even more spherical shape. Cassie and Baxter developed the following relationship for the apparent contact angle [1]:

$$\cos\theta_{CB} = f_r(\cos\theta + 1) - 1 \tag{1.4}$$

where f_r is the contact area fraction, θ is the contact angle on a smooth surface, and θ_{CB} is the (Cassie-Baxter) contact angle on a superhydrophobic surface. One implication of Eq. 1.4 is that as $f_r \rightarrow 0$, the $\theta_{CB} \rightarrow 180°$.

1.4 Wetting and Non-wetting Conditions for Superhydrophobic Surfaces

As the spacing between the ribs or the posts increases, the possibility of liquid entering and wetting the cavities also increases. In order to achieve frictional reduction at the liquid-solid interface, wetting needs to be avoided. The state and shape of the liquid-vapor interface over the cavities depend on the pressure difference, Δp, between the liquid and the vapor. Usually the liquid forms a meniscus at the interface trapping the vapor within the cavity. Young's law provides a relationship between this pressure difference and the meniscus angle [1]:

$$\Delta p = p_w - p_a = \frac{2\sigma}{W_c}\cos(\pi - \phi) \tag{1.5}$$

In the above expression p_w is the liquid static pressure, p_a is the static pressure in the vapor phase, σ is the surface tension, W_c is the cavity width, and ϕ is the meniscus angle. The pressure difference when the angle $\phi = 0$ is referred to as the Laplace pressure. When this pressure is exceeded the liquid will enter and wet the cavity. This wetting state is referred to as the Wenzel state, whereas the non-wetting case is referred to as the Cassie state.

1.5 Important Parameters for Superhydrophobic Surfaces

As mentioned previously the slip length, λ, is another quantity used for analyzing frictional resistance reduction in micro or macro-channel flow. The slip length, λ, is determined

from an overall macro-level qualitative velocity distribution on a superhydrophobic surface as shown in Fig. # 1.4, [3]. This figure illustrates the physics of the liquid flow near a superhydrophobic surface from a macroscopic point of view.

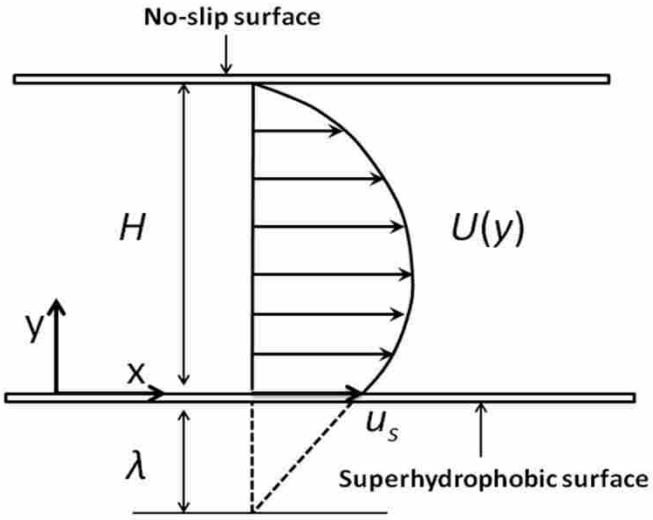

Figure 1.4 Qualitative representation of the velocity profile over a superhydrophobic surface and the apparent slip length, λ.

A qualitative velocity profile for a fully-developed liquid laminar flow in a channel between two infinite parallel plates is shown. For comparison purposes the top plate illustrates a no-slip surface, whereas the bottom plate exhibits a non-wetting superhydrophobic surface. Even though both plates are presumed to be fixed, the liquid velocity at the top plate is zero, but at the superhydrophobic surface of the bottom plate an overall or apparent slip velocity, u_s, prevails.

The schematic diagram in Fig. # 1.5 demonstrates qualitative velocity distributions in regions where both slip and no-slip conditions exist. The illustration represents a 2-D image of a portion of a channel with a bottom surface that has been patterned with micro-posts. On this

figure d is the cavity depth, $H/2$ is half the channel height, W_s, W_c, and W represent the solid micro-post width, the cavity width, and their sum (pitch), respectively. This illustration is for the non-wetting (superhydrophobic) scenario where liquid does not enter the cavity. Further, the liquid-vapor interface is assumed to be flat and the effect of the meniscus is neglected.

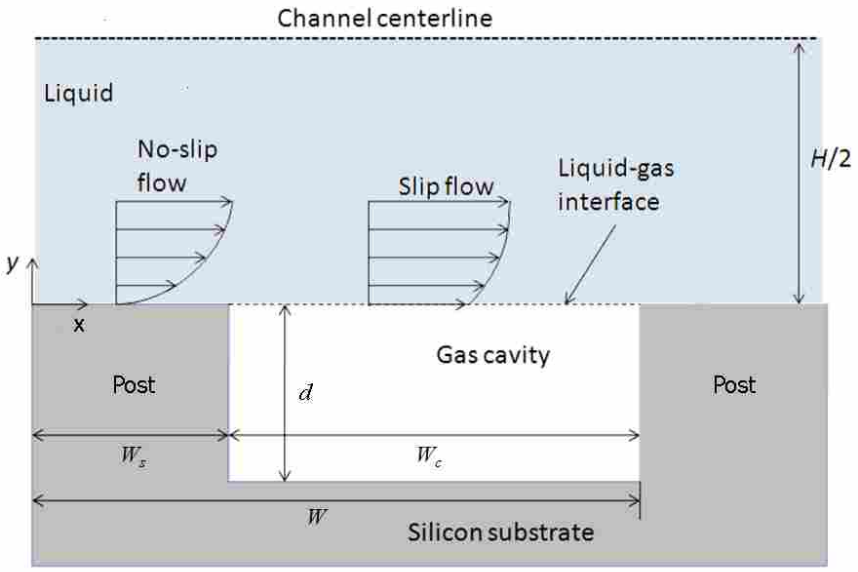

Figure 1.5 Illustration identifying channel regions, dimensions, and notations used in relation to superhydrophobic surfaces. Qualitative velocity distributions are also shown.

Several parameters that are known to be relevant to superhydrophobic surfaces are the cavity fraction, F_c, relative module width, W_m, and Reynolds number. These are defined by the equations below:

$$F_c = A_c/A \tag{1.6}$$

$$W_m = W/D_h \tag{1.7}$$

$$Re = (\bar{U}D_h)/\nu \tag{1.8}$$

In the above expressions, A_c is the projected surface area of the cavity surface, A_p is the projected surface area of the post surface, and A is the total projected surface area (A_c+A_p). D_h is the channel hydraulic diameter and it can be shown that $D_h = 2H$ for infinite parallel plates, $\bar{U}$ is the average streamwise velocity, and v is the liquid kinematic viscosity. Channel height H is the distance between top of the posts on the two infinite parallel plates. Frictional resistance is usually quantified in terms of the Darcy friction factor, f, and Reynolds number product. Since this product, fRe, is equal to a constant in channel flow, it is useful for comparison purposes for various flow scenarios.

Figure 1.5 illustrated a microscopic point of view of a liquid flow over a surface exhibiting a periodic array of solid/cavity patterning. The figure demonstrates alternating regions of no-slip and slip flow over the superhydrophobic surface. The integral average velocity at $y = 0$ over the solid/cavity region results in the non-zero area averaged or apparent slip velocity, u_s depicted in Fig. # 1.4. As it will be shown in Chapter 3, this macroscopic slip velocity is directly related to slip length and the velocity gradient normal to the surface. The slip length is defined by calculating the normal distance obtained by linear extrapolation of velocity profile at the superhydrophobic surface to where the streamwise velocity would vanish. Since the velocity gradient in the normal direction over a superhydrophobic surface is decreased, a reduction in wall shear stress and surface frictional resistance is observed and the overall liquid flow rate is enhanced. Depending on certain parameters, the reduction in frictional resistance can be significant.

1.6 Contributions

The general contribution of this study is a better understanding of the influence that superhydrophobic surfaces have on the reduction in frictional resistance for liquid flow through micro-channels. More specifically it provides an increased knowledge for current deficiencies in areas related to flow over post-patterned superhydrophobic surfaces. A detailed description based on the numerical results reveals how the influences of different parameters affect the reduction of drag in micro-channels. The results also provide a valuable reference for others in this field since there have been relatively few studies of 3-D numerical work for surfaces with micro-post geometries. The numerical results for an extended range of cavity fraction, relative module width, and Reynolds number for liquid flow over superhydrophobic surfaces exhibiting micro-posts will be added to the academic knowledge base in this area.

1.7 Division and Topics of the Remaining Chapters

Chapter 2 includes a thorough literature review of superhydrophobic surfaces with micro-post geometries. A brief literature review of droplet dynamics and surfaces with micro-rib structures is also provided. These include experimental, analytical, and numerical results for 2-D and 3-D cases.

Chapter 3 addresses the analysis and the physics of liquid laminar flow over superhydrophobic surfaces including micro-ribs and micro-posts. Important expressions for various parameters are derived and discussed. The limitations and validity of these expressions are presented.

In Chapter 4 the procedures, conditions, and approach, including assumptions for the 3-D numerical model, are presented. The differential equations governing the flow of fluid are presented and the solution approach is outlined. The boundary conditions and the approach for examining effects of various parameters are discussed. Convergence criteria, mesh independency, accuracy, the type of solver used, and pressure coupling are covered in detail.

Chapter 5 presents the results from the research. These include velocity and shear contours, and graphs showing the effects of the key parameters on the overall frictional resistance. Comparisons between the previously explored micro-rib and micro-post geometries are provided.

Chapter 6 contains the conclusion and contributions of the work and provides recommendations for future work.

2 LITERATURE REVIEW

Fluid behavior in nature, like many other fields of science, has sparked the interest and curiosity of mankind over the past several and even thousands of years. It is known that ancient civilizations built sailing ships and irrigation systems. Archimedes was able to formulate laws of buoyancy and experimentally applied them to submerged and floating bodies. Presently, the field of fluid mechanics is extremely broad and consists of many areas that deal with very large and extremely small length scales. Scientific research, testing, and technological developments in macro- and micro-scale fluid mechanics have increased significantly in recent years. Many practical applications have resulted from these developments. For instance, the study of the dynamics of liquid droplets and streams at small length scales has led to new commercial applications such as MEMS and NEMS. Availability of powerful and fast computers has enabled researchers to obtain approximate numerical solutions to problems that would be otherwise impossible to solve. Analytical, numerical, and experimental research has been conducted by many scholars at micro-and nano-scale levels. One such example is the study of liquid droplets and streams on superhydrophobic surfaces. This chapter summarizes some of the most important and recent works pertaining to the reduction of frictional resistance over superhydrophobic surfaces that have appeared in the open literature. It includes literature reviews related to the dynamics of liquid droplets over superhydrophobic surfaces and liquid laminar flow through micro-channels with rib and post patterned walls.

2.1 Liquid Droplets on Superhydrophobic Surfaces

The study of liquid droplets on hydrophilic, hydrophobic, and superhydrophobic surfaces is not an objective of this research. Review of the literature related to liquid droplets, however, provides some valuable insights into determining important surface geometrical parameters and their effects on frictional resistance reduction. The equilibrium state and spreading of water droplets over superhydrophobic surfaces were examined numerically by Dupuis and Yeomans [4]. The surfaces they employed consisted of arrays of micro-post patterning. A Lattice Boltzmann algorithm was utilized to obtain solution of the equations of motion that described the static or equilibrium and the dynamic behavior of droplets on superhydrophobic substrates. The dynamic behavior consisted of characterizing the transition of the droplets from the non-wetting (Cassie) to wetting (Wenzel) states. It was determined that such superhydrophobic surfaces at static equilibrium with the post height, spacing, and width of 5, 8, and 4 μm and for a droplet with a radius of 30 μm and kinematic viscosity of $\nu = 3\text{x}10^{-5}$ m/s^2, respectively, could result in contact angles as high as 156°.

Simple surface tilting experiments have been performed by several researchers to characterize the decrease in droplet motion resistance due to the influence of superhydrophobic surfaces [3, 5, 6]. Oner and McCarthy [6] experimentally examined the effects of various shapes, sizes, and spacing of posts on hydrophobicity or wettability of surfaces coated with three different treatments. This was accomplished by measuring the force required to move a droplet on each surface considered. They observed that surfaces featuring square posts with dimensions of less than or equal to 32 μm exhibited very noticeable superhydrophobic behavior. They indicated that the spacing between the posts and the shape of the posts greatly affected the contact angle as expected. However, it was shown that the post height exhibited only small

influence on the contact angle. The scenario that yielded the highest observed contact angle consisted of 40 μm high rhombus shaped posts that exhibited a spacing of 40 μm between posts.

Kim and Kim also performed surface tilting experiments to measure flow resistance for water droplets on superhydrophobic surfaces [5] in both an open and a confined micro-channel. Their surfaces consisted of micro-ribs aligned transverse and parallel to the path that the droplet was to follow. They also explored the effect of micro-posts and nano-posts on the flow resistance and used a smooth surface as a reference. Experiments were performed for both an open and a confined channel on five different surfaces, as explained above, with water droplets of four different volumes 12, 17, 22, and 27 μl. A Teflon coating was applied to all surfaces they considered. Their results indicate that surfaces with nano-posts and micro-posts provide less flow resistance when compared to surfaces using ribs oriented parallel or transverse to the path of the droplet. Nano-post patterned surfaces provided the minimum flow resistance of approximately 0.01. They reported over 99% and 95% reductions in frictional resistance for open and confined micro-channels, respectively. For instance, in their experimental research of a water droplet motion in a micro-channel obtained frictional resistance of 0.05 and 0.35 for nano-posts and micro-posts, respectively. With the nano-post design the water droplet was found to roll off the surface at nearly 0° tilting angle. They were able to obtain contact angles of about 160° on micro-post surfaces and over 175° on surfaces with nano-post features at the cavity fraction of about 0.99.

In another experimental investigation Zhu *et al*. tuned the wettability of a solid surface by changing its roughness [7]. These researchers used square micro-post (or pillar) arrays and determined that the apparent contact angle of a hydrophobic surface can be continuously

adjusted from the intrinsic contact angle to a superhydrophobic contact angle. They claimed that the largest apparent contact angle in their experiment was 162° with square posts of 9.45 μm in width, 16 μm high and a spacing of 26.34 μm having $F_c \approx 0.93$.

Miwa *et al.* [8] developed various superhydrophobic films with different surface roughness consisting of various boehmite-ethanol ratios and measured the sliding angle for water droplets. The smallest sliding angle measured was about 1° for a 7 mg water droplet. They concluded that by trapping air, surface structures can result in very low sliding angles.

In summary, for both the static state where a droplet rests on a surface and the dynamic state where the droplet motion is considered, superhydrophobic surfaces provide significantly lower frictional resistance than a non- superhydrophobic surface and result in very high contact angles. The important parameters such as cavity fraction and cavity depth directly affect both the contact angle and the sliding angle of a droplet on a superhydrophobic surface. However, the influence of cavity depth on the contact angle and the frictional resistance is not as significant as other parameters such as cavity fraction. The overall conclusion indicates as cavity fraction increases both the sliding angle and the frictional resistance decrease, whereas the contact angle increases. Also, all the literature reviewed related to the physics of a droplet on a superhydrophobic surface concluded that the size of the droplet affects its static and dynamic behavior over such surfaces. As a result, the relative size of the droplet with respect to the geometric dimensions of surface structures is important.

2.2 Liquid Laminar Flow in Superhydrophobic Micro-channels

There are several types of superhydrophobic surfaces for which liquid laminar flow have been explored. The remainder of this chapter includes a general review of literature related to flow in channels with superhydrophobic surfaces featuring both micro-rib and micro-post structures. It is important to note that while the focus of this research was micro-channel liquid laminar flow on superhydrophobic surfaces consisting of micro-post geometries, many of underlying physics of the flow are similar to liquid flow over micro-rib geometries. The main purpose of most previous studies has been on characterizing the influence of the important parameters on the overall frictional resistance reduction, slip velocity, and/or slip length.

2.2.1 Surfaces with Micro-rib Structures

For flow over surfaces exhibiting alternating rib and cavity features, the liquid can flow at various orientations with respect to the micro-ribs. Principally two flow orientations have been considered 1) liquid flow parallel or longitudinal to the ribs and 2) perpendicular or transverse to the ribs. Philip [9] analytically explored the scenario of creeping viscous flow through a two dimensional channel for vanishing Knudsen number, *Kn*, exhibiting alternating ribs (or strips) of no-slip and no-shear with flat interface boundary conditions. Solutions of the Navier-Stokes equations for both longitudinal and transverse array of ribs were obtained analytically. This work showed an increase in the effective fluid slip length with increasing cavity fraction.

Lauga and Stone [10] analytically investigated steady pressure-driven Stokes flow ($Re \rightarrow 0$) through a circular micro-channel. Their studies were also limited to two-dimensional liquid flow and flat liquid-vapor interface over the cavities. They examined both longitudinal

and transverse rib configurations and results in each case were compared with the results of Philip. For a general flow with mixed slip/no-slip wall boundary condition an "effective slip length" was defined. The experimental data for pressure drop and dimensionless total flow rate were converted to a dimensionless effective slip length. This quantity was then written in terms of geometric parameters for both longitudinal and transverse cases. It will be shown in chapter 3 that the slip length is inversely proportional to the channel friction factor. Therefore, as the effective slip length increases the friction factor decreases which is a very sought after goal in micro-channel liquid flow. One of their important conclusions was that the effective slip length for the longitudinal rib configuration was twice that of the transverse case, $\lambda_{\parallel}=2\lambda_{\perp}$, where $\lambda_{\parallel}$ and $\lambda_{\perp}$ are the effective or apparent slip lengths for the two respective rib configurations. As a result, the longitudinal ribs should provide less frictional resistance to the flow than the transverse ribs.

Ou *et al*. [11] performed an experimental investigation to characterize the pressure drop reduction for water flow through micro-engineered superhydrophobic channels. Hydraulic diameters for the channels ranged from 152 to 508 μm. The top surface of the rectangular channel was hydrophilic glass and the bottom surface was a superhydrophobic surface. Their study used two different roughness patterns, micro-ribs (or ridges) oriented longitudinal to the flow direction and cylindrical micro-posts. Cavity fractions of 50%, 66.7%, and 80% were explored. They calculated apparent slip lengths as large as 20 μm and pressure drop reductions of up to 40% in a creeping flow regime.

In a follow-on study Ou and Rothstein [12] used μ-PIV (Micro-Particle Image Velocimetry) techniques to show that the decrease in shear stress along a micro-cavity interface is the actual mechanism for pressure drop reduction in a micro-channel. The commercial

software package FLUENT was used to numerically validate their experimental results. They created a 3-D model for an array of micro-ribs and assumed no shear at the water-cavity interface. They found that a maximum slip velocity of more than 60% of the average velocity in the micro-channel occurred at the center of the shear-free air-water interface. Their numerical results under-predicted the pressure drop reduction in comparison to the experimental data.

Choi *et al*. [13] performed drag reduction experiments in micro-channels of various heights ranging between 2 μm and 12 μm that consisted of Teflon-coated nano-grated hydrophobic and nano-grated hydrophilic surfaces. The nano-grates were analogous to ribs in micro scale levels and were designed to be very dense, about 230 nm pitch, but very deep, about 500 nm. The pitch is defined as the total width W illustrated in Fig. # 1.5. Their results showed pressure drop reductions as high as 30% and slip lengths up to 200 nm in a 3 μm high channel for water flowing parallel to the nano-grates. The slip length of 200 nm for the channel used in their experiment is equivalent to a relative slip length, λ/W, of only 0.87 which is not very significant. They also confirmed that flow parallel to the nano-grating pattern produces a larger effective (or apparent) slip length than transverse flow does.

Davies *et al.* [14] performed a numerical study of the fluid flow across superhydrophobic ribs transverse to the flow direction. Their results showed that for flow across ribs oriented transverse to the direction of flow the magnitude of the reduction in the friction factor is dependent on the Reynolds number. The results also indicated that at small cavity fractions, F_c, the reduction in the fRe is influenced insignificantly by cavity depth, but as the F_c increases the influence that the cavity depth has on fRe also increases. Including the vapor cavity in the model by matching the shear stress and velocities in the liquid and vapor phases of the interface

increased the predicted value of the friction factor when compared to models that assumed no-shear at the interface. They also showed that the influence of the cavity asymptotically approaches a limit as the cavity depth increases such that when the vapor cavity depth is greater than 25% of its width the effect on overall friction factor becomes insignificant. They also discovered that the zero-shear model consistently under-predicted the overall flow resistance by about 6% compared with the liquid-vapor cavity coupled model. The deviation between the two models was larger for increasing values of cavity fraction and relative module width. Reductions in the friction factor as high as 80% were reported for flow across transverse ribs in a micro-channel with very small hydraulic diameter.

An experimental/analytical investigation of the laminar flow in a parallel-plate micro-channel with superhydrophobic top and bottom walls was performed by Maynes *et al.* [15]. The walls were fabricated with micro-ribs and cavities oriented parallel to the flow direction. They assumed the liquid-vapor meniscus in cavities were flat in their analysis. They considered and compared two models regarding the liquid-vapor interface. One was a zero-shear model and the other was a liquid-vapor cavity coupled model. In the latter case an analytical model of the vapor cavity was obtained and coupled with a numerical model of the liquid flow above the liquid-vapor interface. This was accomplished by matching the liquid and vapor velocity and shear stress at the interface. The deviation between these models was more pronounced at large values of cavity fraction and relative module width. The results showed that the effective slip length and the reduction in the friction factor increased with increasing cavity width, increasing cavity depth, and decreasing relative module width. For all scenarios tested, the predicted slip velocity was smaller for the liquid-vapor cavity model than for the zero-shear model. It was further discovered that the influence of vapor cavity depth was stronger at large values of F_c and

W_m. The effect of meniscus shape was also explored numerically by allowing the meniscus to penetrate into the cavity region in a parabolic form. The results were compared with the flat liquid-vapor interface scenario. It was discovered that the magnitude of *fRe* marginally increased as the meniscus penetration into the cavity region increased. The maximum increase in *fRe* was approximately 4.2%.

Sbragaglia *et al.* [16] analyzed the effects of the meniscus at the liquid-vapor interface on the slip length and were able to theoretically characterize corrections to the effective slip length. Liquid flow through a rectangular channel with equally spaced ribs parallel to the flow direction was considered. The results were compared with those reported by Ou *et al*. [11]. The correction factor for cavity width of about 60 μm was on the order of 0.03-0.06 which is very small indicating the curvature effect of the meniscus is insignificant, whereas for cavity width of about 10 μm it was on the order of 0.1 verifying a stronger influence in this case. They also observed that when all flow conditions are the same, micro-ribs oriented parallel to the flow were more susceptible to wetting than transverse oriented ribs.

A recent work by Woolford *et al.* [17] compared two limiting cases of complete wetting and non-wetting for laminar liquid flow through a micro-channel. The top and bottom walls of the micro-channel featured micro-ribs for two scenarios, parallel and perpendicular to the direction of the flow. They concluded that the reduction to flow friction is more significant when liquid does not enter the cavities (Cassie state). From the collected data they introduced mathematical expressions that would best fit the data for four different cases of wetting and non-wetting scenarios, for both longitudinal and transverse oriented micro-ribs. Their experimental data also indicated that it is more difficult to maintain the superhydrophobic state (*i.e*. prevent

wetting) when micro-ribs are aligned parallel to the flow as opposed to the transverse rib/cavity configuration.

Analytical solutions for Stokes flow through micro-channels using longitudinal and transverse micro-ribs were obtained by Teo and Khoo [18]. They quantified the fluid resistance reduction in terms of the normalized effective slip length. It was also concluded that the effective slip length increased with cavity fraction for both the longitudinal and transverse rib orientation scenarios. The comparison of the two types confirmed greater reduction in frictional resistance in the case of longitudinal flow, consistent with the results of other investigators. Cheng *et al*. [19] studied the effects of *Re* on longitudinal and transverse micro-ribs. They showed that at high *Re* transverse ribs resulted in deteriorating influence on effective slip length which was similar to the conclusions of Davies *et al*. [14]. They also showed the effective slip length was independent of *Re* for the longitudinal micro-ribs scenario. The validity of their results was confirmed by comparison with results obtained from derived scaling laws for pressure-driven flows.

Gao and Feng numerically simulated shear flow over a superhydrophobic surface with transverse micro-ribs for four different flow regimes [20]. These regimes were: air trapped and trapped (or pinned) inside the cavities; air released (or depinned) and free to move onto the ribs; air released and totally covering the solid surface, creating a continuous layer of air cushion over the entire surface; and a scenario with periodic movement of air bubbles over the solid surface. The scenario with the continuous air film produced the largest apparent or effective slip length.

From the review of the literature it is evident that superhydrophobic surfaces with micro-rib configurations can reduce frictional resistance and the required driving force in liquid micro-

channel flow. The focus of the recent research by the scholars in this field is mainly on fabrication of superhydrophobic surfaces in general and to a lesser degree on determining what and how certain factors could affect frictional resistance reduction in micro-channels with superhydrophobic surfaces. The following list summarizes the highlights of the reviewed literature regarding micro-rib patterned superhydrophobic surfaces:

1. Micro-rib patterned superhydrophobic surfaces can reduce frictional resistance significantly.
2. Reduction in frictional resistance translates directly into a decrease in the required driving force especially in liquid micro-channel flow.
3. Micro-ribs oriented both parallel and perpendicular to the flow direction reduce frictional resistance.
4. In general, superhydrophobic surfaces with longitudinal micro-ribs reduce frictional resistance more than superhydrophobic surfaces with transverse oriented micro-ribs.
5. Longitudinal micro-ribs are more susceptible to wetting than transverse oriented micro-ribs.
6. Reduction of shear stress at the liquid-vapor interface over the cavities is the cause of frictional resistance reduction.
7. An increase in cavity fraction results in a greater amount of apparent slip length and a reduction in friction factor.
8. The slip length increases and the frictional resistance decreases as the relative module width is increased which implies that in short channels the effect of superhydrophobic surfaces with micro-rib configurations is more significant as far as frictional resistance is concerned.

9. The effect of cavity depth on frictional resistance is not as significant as other parameters such as cavity fraction and relative module width, but some effect is observed up to a cavity depth of 25% of its width. However, the cavity depth influence increased with increasing F_c and W_m.
10. The effect of meniscus curvature on frictional resistance in bulk liquid flow is insignificant. A maximum increase of about 4.2% in *fRe* has been observed compared with the flat liquid-vapor interface scenarios.
11. For the longitudinal micro-ribs no dependence on *Re* has been observed, but in the transverse oriented micro-ribs stronger influence has been noticed at high *Re* values.

2.2.2 Surfaces with Micro-Post Structures

Superhydrophobic surfaces exhibiting micro-posts of different shapes have also been considered, but to a much smaller extent. Obviously, in order to reduce frictional resistance smaller liquid-solid contact area is desirable while maintaining non-wetting condition within the cavities. Therefore, significantly larger cavity fractions should be obtained by using superhydrophobic surfaces with micro-post features. As far as frictional resistance reduction is concerned, it is useful to determine answers to the following questions:

1. Do micro-post patterned surfaces generally perform better than micro-rib patterned surfaces?
2. Are micro-post features more susceptible to wetting than micro-rib features at the same cavity fraction?
3. What are the qualitative effects of the important parameters F_c, W_m, and *Re* on the frictional resistance for micro-post patterned surfaces?

4. Do the shapes of micro-posts and their arrangements affect their overall performance?
5. Are there any differences between pressure-driven versus Couette flows for micro-post patterned surfaces?
6. Is there any lower limit as the size of the micro-posts is concerned? Considering the fabrication issue, what is the smallest post that can be manufactured with the present technology?

Although quantitative solutions and comprehensive understanding of liquid slip in flow over superhydrophobic surfaces have not been completely obtained, some experimental and analytical studies have been performed. A limited amount of previous studies addressing post patterned superhydrophobic surfaces were found in the literature, but none provided convincing answers to all the above questions. Because analytical solutions for the 3-D governing equations are not possible for the micro-post configuration, the analytical studies performed appear to be limited to scaling law relations. The remainder of this chapter is devoted to studies performed thus far by other researchers related to superhydrophobic surfaces with micro-post configurations.

Choi and Kim [21] fabricated superhydrophobic surfaces consisting of conical posts and experimentally measured the slip length in a Couette flow environment. Four different surfaces were prepared and tested with water and 30% weight glycerin as the flowing liquid at constant room temperature and approximately 1 atm pressure. The superhydrophobic surfaces which were referred to as nano-turf were developed from a silicone substrate having needle/conical shaped posts about 1-2 μm high arranged in a square array approximately 0.5-1 μm apart. However, the presented SEM image of such surfaces did not show a uniform arrangement. The

surfaces tested were smooth hydrophilic, smooth hydrophobic, hydrophilic nano-turf, and hydrophobic nano-turf. The apparent contact angles of more than 175° were observed on the hydrophobic nano-turf surfaces. For the design of the nano-turf surfaces two equations were developed for the post height and the pitch in terms of surface tension of the liquid, liquid-vapor pressure difference, cone angle, and the meniscus angle. A cone-and-plate rheometer was used to measure the torque applied to the liquid confined between the superhydrophobic substrate and the rheometer. This torque was then used to mathematically calculate the corresponding apparent slip length. They observed slip lengths of approximately 20 μm for water and 50 μm for a 30% weight glycerin. For instance, they postulated that such a slip length for water would translate into over 66% drag reduction. The flow was laminar with *Re* in the range of 10-1000.

Laminar drag reduction in micro-channels with micro-post designs was also studied by Ou *et al*. [11]. A smooth hydrophobic silicon surface and four superhydrophobic surfaces featuring 30 μm square micro-posts with 15, 30, 60, and 150 μm spacing were prepared and tested. A 2.54 mm wide 127 mm high and 50 mm long rectangular channel with water as the flowing liquid was used. The aspect ratio of 20 was maintained throughout the tests. The test surfaces were fit into the bottom of the channel and the top and side surfaces were made of glass. Pressure drop results were plotted with respect to the volume flow rate and compared with the theoretical pressure drop for a no-slip boundary condition situation. These results indicated that the superhydrophobic surface with the largest spacing between micro-posts did indeed require the least amount of pressure drop to obtain the same flow rate as other surfaces. The shear-free fractions for the surfaces mentioned above ranged from 55.5% to 97%. They obtained reductions in the viscous drag and the required pressure drop of up to 40% for the surface featuring micro-posts spaced 150 μm apart. A linear dependence of the pressure drop reduction

on the shear free fraction at moderate values was reported. It was concluded that the maximum pressure drop reduction reached a plateau of 0.37 as $F_c \rightarrow 1$, but the maximum F_c used was 0.97. The slip length appeared to increase with increasing micro-post spacing and the maximum slip length of 21 μm was obtained for micro-posts spaced 150 μm apart. The effect of channel height was also included in their study. The superhydrophobic surface having micro-posts spaced 30 μm apart was selected and the channel height was varied from 76.2 μm to 254 μm keeping the aspect ratio fixed at 20. In this case the pressure drop reduction was found to decrease linearly with increasing channel height. The largest pressure drop reduction obtained was about 0.35. Their investigation was extended to testing micro-ribs which was covered in the previous section, 2.2.1.

Salamon *et al*. [22] performed a three-dimensional numerical simulation of a Newtonian fluid flow through a micro-channel with superhydrophobic walls. Using finite-element analysis the conservation of mass and momentum equations were solved for the 3-D steady fully developed incompressible flow with appropriate boundary conditions. The channel was patterned with square posts on both the top and the bottom surfaces. The liquid-vapor interface was assumed to be flat for the two scenarios considered. One scenario was non-wetting and the other was partial wetting with liquid intersecting the posts at a distance (d_{wet}) from the top of the posts. In all situations Reynolds number was based on the channel height making certain that $Re < 100$, the channel height was small relative to the channel length and width, and side wall effects were neglected. The influences of post size, post spacing, channel height, and partial wetting on bulk liquid flow through the channel were explored. A sharp gradient of streamwise velocity within 0.5 of the post surface was observed. The apparent slip length was found to be independent of the channel height for the range between 50 μm and 80 μm considered. As post

spacing increased the flow enhancement which was defined in terms of volume flow rate increased and did not appear to asymptote for large values of cavity fraction in contrast to the results obtained by Ou *et al*. [11], where it was discovered that pressure drop reduction asymptote out at about 40%. As expected, both increasing post size and wetting depth had significant adverse effects on flow enhancement. A flow enhancement of about 40% and an apparent slip length of 5.4 μm were obtained for the 80 μm high channel comprised of surfaces with 0.2 μm square posts and 2 μm spacing at a 1 psi/cm axial pressure drop. From the numerical results it was concluded that the apparent slip length can indeed be used to characterize the macroscopic flow behavior of superhydrophobic surfaces.

Ybert *et al*. [23] used an analytical/numerical approach for determining effective slip length. They analytically obtained scaling laws for effective slip length at the surface for two extreme limits as $F_c \rightarrow 0$ and $F_c \rightarrow 1$. Using the expressions for these two limits they derived a general scaling law or formula by interpolation of these two limiting case results. They compared the scaling laws with results obtained numerically for three different geometries: grooves, posts, and holes. They also examined the effects of the gas phase and meniscus curvature on the slip length for surfaces consisting of post, rib, and grate patterns. It was discovered that surfaces with large slip lengths or cavity fractions are more sensitive to meniscus curvature effects or wetting. Also, surfaces patterned with holes were more prone to destabilization of the liquid-vapor interface. The scaling laws predicted that as the cavity fraction increased the apparent slip length increased. The largest effective (or relative) slip length of about 2 was observed for the square posts and it was also concluded that achieving very large slip lengths (about 100 μm) is more possible with surfaces featuring posts than other configurations.

Experiments performed by Lee *et al.* [24] to study the effects of two important geometric parameters, cavity fraction and pitch, on the apparent slip length produced noteworthy results. The pitch was defined as the distance between two similar points on the neighboring posts or ribs which is analogous to the total width, *W*, described in Fig. # 1.5. A rotating cone rheometer was used to drive the flow over two different microstructured surfaces consisting of cylindrical posts and concentric grates (or ribs). The design of superhydrophobic surfaces was based on the force balance to ensure the existence of Cassie state or stability of the meniscus at the liquid-vapor interface over the cavities. For such stability situation two different mathematical expressions were employed for surfaces with post and rib configurations. The maximum sustainable cavity fraction at a fixed pitch and four different liquid pressures 200, 300, 500, and 1000 Pa were calculated. In order to investigate the effect of cavity fraction on the apparent slip length the pitch and the depth were kept constant at 50 μm for both surfaces. For the posts 50, 85, 95, 98, and 99% and for the ribs 50, 85, 95, and 98% cavity fractions were considered. The results of the posts and the ribs were compared with the scaling laws of Ybert *et al*. [23] and the theoretical predictions of Lauga and Stone [10], respectively. It was concluded that the apparent slip length over superhydrophobic surfaces increases exponentially with gas (or cavity) fraction and linearly with another important surface parameter, pitch. The slip length increased more significantly for posts than for ribs at high cavity fractions, $F_c > 90\%$, but this phenomenon was reversed at low cavity fractions. This result was similar to the analytical scaling law predictions of Ybert *et al*. [23]. In their investigation of the effect of pitch on the slip length, it was discovered that at the same pressure and cavity fraction posts were more susceptible to wetting than the ribs. For instance, at the $F_c = 0.98$ and the liquid pressure of about 300 Pa, the transition to the Cassie state occurred at 60 μm pitch for the posts compared with 230 μm pitch for the ribs. The

maximum effective slip length of about 185 μm was reported for the ribs at 98% cavity fraction, 200 μm pitch, and 300 Pa liquid pressure which was achieved by carefully delaying the transition from the non-wetting or Cassie state to wetting or Wenzel state.

Ng and Wang [25] presented a mathematical model for an array of circular and square posts for two cases of no-slip and partial-slip over the solid areas. They used previously published scaling laws and derived an expression for effective slip length as a function of cavity fraction. They obtained a larger slip length for the asymmetric case where the cavity width in the transverse direction is greater than the longitudinal one.

Recently Govardhan *et al*. [26] has explored the transient nature of liquid flow over superhydrophobic surfaces. They experimentally studied the reduction of air within the cavities due to diffusion and its effect on hydrophobicity of a surface over time. The width and the height of the channel were 0.64 and 20 mm, respectively. Direct shear stress measurements of water flow over randomly textured superhydrophobic surface were made. The average cavity or crevice size was about 50 m. The two cases of hydrophilic and hydrophobic surfaces were tested and compared. The surfaces were immersed in water and the decay of trapped air pockets over time was visually observed. They concluded that the effective slip length also decreased with time. This phenomenon was observed at a wide range of water pressure from 600 Pa to 4500 Pa. At a given time as the shear stress values increased the apparent slip length decreased verifying the diminishing presence of trapped air within the cavities. This study provides an insight and a way to measure the time period through which a superhydrophobic surface with trapped air in the cavities can provide pressure drop decrease through a micro-channel.

In summary, it appears that superhydrophobic surfaces featuring micro-post configurations also reduce frictional resistance for liquid laminar flow in micro-channels. As far as the bulk liquid flow in micro-channels is concerned and from a macroscopic viewpoint surfaces with micro-ribs and micro-posts exhibit similar characteristics. In addition to the summary list provided at the end of the previous section for micro-ribs, the following list emphasizes the effectiveness of surfaces exhibiting micro-posts in reducing frictional resistance and the required driving force:

1. Certain parameters such as cavity fraction, cavity depth, and the spacing of micro-posts affect the apparent slip length and frictional resistance reduction.
2. Surfaces with micro-post features could be more susceptible to wetting than micro-ribs.
3. If Cassie state can be maintained, at very high cavity fractions micro-posts provide the least amount of frictional resistance compared with other surface configurations.
4. The effect of cavity depth on the apparent slip length is not as pronounced as the cavity fraction or the post spacing.
5. At low cavity fractions longitudinal micro-ribs result in greater apparent slip length than micro-posts.
6. The apparent slip length increases exponentially with cavity fraction and linearly with pitch.
7. There is a linear dependence of pressure drop reduction on the cavity fraction.

It is also important to note the following general conclusions for liquid laminar flow in micro-channels: 1) superhydrophobic surfaces, regardless of the type of the micro-structure used,

can reduce the overall frictional resistance, 2) surface roughness could increase the hydrophobicity of a surface, 3) as the cavity fraction increases the frictional resistance decreases, and 4) in order to reduce frictional resistance wetting needs to be avoided. Therefore, an important question would be, for the same amount of liquid-solid contact should micro-post geometries provide greater decrease in frictional resistance or increase in slip length than other types of micro-structures? It is important to realize that fewer studies on micro-posts have been conducted than on other types of geometries such as micro-ribs. Not only will our studies provide answers to some unaddressed and important questions pertaining to superhydrophobic surfaces, but also they will fill in gaps found in the literature as listed below:

1. All the previous work has been limited to either specific values or a very narrow range of cavity fraction and relative module width. This work covers a very wide range of cavity fraction $0.0 \leq F_c \leq 0.9998$ and relative module width $0.01 \leq W_m \leq 1.5$.
2. Previous studies on micro-posts have either considered only creeping flow regimes $Re \leq 1$ or situations with $Re \leq 100$, whereas our research was extended to very high Reynolds numbers $1 \leq Re \leq 2500$.
3. Issues such as the difference between pressure-driven flow and Couette flow and their effects on fRe and slip length λ have not been addressed by anyone yet. Comparisons over a wide range of cavity fractions and relative module widths have not been performed.
4. Rectangular posts and their influence on fRe and λ have not been explored to this date.
5. The outcome of this study could be used as a benchmark for further studies on superhydrophobic surfaces.

Two discrepancies have been discovered in the literature and it would be helpful to realize how our results compare with the conclusions arrived at by other researchers concerning these issues. Some groups such as Ou *et al*. [11, 12] claimed that the effect of cavity fraction on frictional resistance asymptotically levels off at about 40% as cavity fraction increases; whereas Salamon *et al*. [22], Ybert *et al*. [23], and Lee *et al*. [24] have concluded that it decreases exponentially. The other issue involved how micro-posts are the best candidate for achieving very high frictional resistance, Ybert *et al*. [23], but Lee *et al*. [24] discovered that obtaining very large apparent slip lengths was possible with micro-ribs not micro-posts.

3 ANALYSIS

This chapter presents fundamental analysis related to steady laminar viscous flow through channels where apparent slip at the wall exists. The overall purpose is to discuss expressions that will be used in comparing and evaluating the results of the present numerical simulations. These expressions will also show the relationship between certain important parameters and frictional resistance. In the following analysis it is assumed that the geometrical dimensions of surface structures are very small relative to the size of the channel while determining the overall effect of these micro-structures on the entire flow and frictional resistance reduction is of utmost importance. For that reason a macroscopic viewpoint in the analysis where apparent slip exists at the walls will be considered. This apparent slip is an overall average of the real microscopic phenomenon prevalent at the channel surface. This phenomenon consists of periodically occurring slip and no-slip conditions over the cavity regions and the micro-structure surfaces, respectively. The developments of some important relations for certain parameters such as the slip length and the friction factor Reynolds number product *fRe* are included to demonstrate what other parameters indirectly affect frictional resistance and how *fRe*, slip length, and other parameters are related. It is important to emphasize that the governing equations of the considered 3-D models for the liquid channel flow with micro-post patterned walls are not solvable in closed form. Since from a macroscopic perspective all micro-structures to various degrees have similar effects on the bulk liquid flow through the channel, previously

developed relations for micro-ribs are included to underline the importance of certain parameters and to analyze and compare results. The physics of liquid flow through micro-channels with micro-post patterned walls is similar in many regards to flow through micro-channels with micro-rib patterned walls. More comprehensive attention has been devoted to experimental and numerical analysis of micro-channels with ribs than those consisting of surfaces with posts or pillars. Therefore, it is useful to consider micro-ribs prior to explaining the physical aspect of liquid flow near a superhydrophobic surface with micro-post geometries. The main purpose of this chapter is to use some fundamental definitions and relationships in fluid dynamics to derive several useful expressions for certain important parameters. The developments in this chapter will also illustrate the physics involved in both pressure-driven and Couette liquid flow through micro-channels with slip boundary conditions. The derived equations will then be utilized in chapter 5 to further analyze and discuss the results obtained from simulations. As mentioned before, liquid can flow either parallel or perpendicular to the rib structures. Some interesting similarities and differences between these two situations have been observed by scholars in the field. Expressions have been developed for the normalized apparent slip length λ/w and fRe for both non-wetting and wetting conditions with ribs oriented longitudinal and transverse to the flow [1] and these will be discussed in more detail later in this chapter. It is imperative to first define a few important and basic parameters and explain their relevance to liquid flow in micro-channels with superhydrophobic walls.

A geometric parameter used quite often in channel flow is the hydraulic diameter D_h which is defined according to the following equation

$$D_h = \frac{4A_{cs}}{p_{cs}} \tag{3.1}$$

where A_{cs} and p_{cs} are cross sectional area and the wetted perimeter for the cross section, respectively. In the case of two infinite parallel plates separated by distance H, the width is infinite, $W_{ch} >> H$, and thus Eq. 3.1 reduces to $D_h = 2H$. When a small rectangular element of fluid is subjected to shearing forces the element deforms continuously as illustrated in Fig. # 3.1.

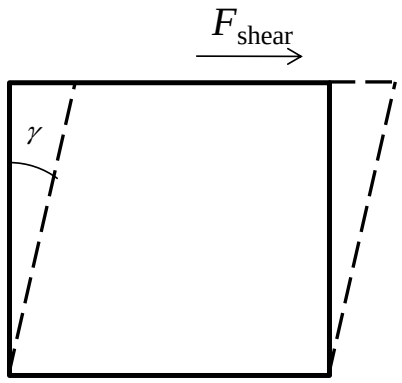

Figure 3.1: Liquid element subjected to a shearing force F_{shear} causing an angular deformation or strain γ.

This angular deformation or shear strain γ is related to shearing stress according to the well known Hooke's law $\tau = G\gamma$. In this equation τ is the shear stress and G is the shear modulus. The rate of this angular deformation is referred to as shear strain rate or simply stain rate $\dot{\gamma}$. For the case of single velocity component u the strain rate can be defined as shown in Fig. # 3.2.

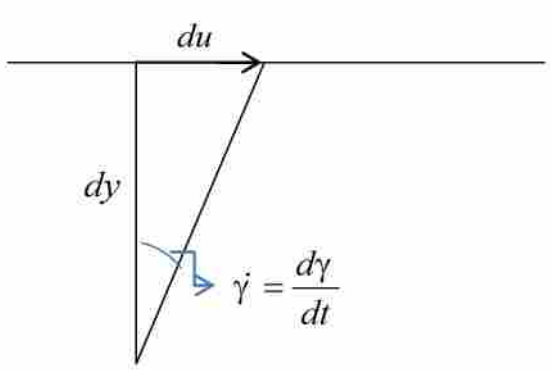

Figure 3.2: Relationship between strain rate $\dot{\gamma}$, differential velocity component *du*, and vertical distance *dy*.

For small angles $\frac{d\gamma}{dt} \approx \frac{du}{dy}$ and thus the strain rate can be expressed as $\dot{\gamma} = \frac{du}{dy}$. As illustrated in Fig. # 1.5, from a macroscopic viewpoint an apparent slip length can exist at superhydrophobic walls and because a linear extrapolation is used to obtain the apparent slip length, the following relationship between slip velocity and slip length can be written

$$\frac{du}{dy} = \frac{u_s}{\lambda} \tag{3.2}$$

Recall u_s is the apparent slip velocity and λ is the apparent slip length. Equation 3.5 can be rearranged to obtain a useful relationship between the apparent slip velocity, slip length, and strain rate as expressed below

$$u_s = \lambda \left.\frac{du}{dy}\right|_w = \lambda \dot{\gamma} \tag{3.3}$$

The above expression and Equation 1.1 can be combined to obtain a new expression for shear stress at the wall τ_w in terms of the apparent slip velocity u_s and slip length λ

$$\tau_w = \frac{\mu u_s}{\lambda} \tag{3.4}$$

Eq. 3.4 can be substituted into a fundamental relationship between the wall shear stress τ_w and the Darcy friction factor f to obtain the following expression for the friction factor f in terms of u_s and λ

$$f = \frac{8\tau_w}{\rho \bar{U}^2} = \frac{8\mu u_s}{\rho \lambda \bar{U}^2} \tag{3.5}$$

where ρ is the liquid density and $\bar{U}$ is the average channel velocity. Since in classical laminar channel flow, the product of the Darcy friction factor and Reynolds number *fRe* is a constant and equal to 96 it would be very useful to obtain the same product for a channel with superhydrophobic surfaces. Multiplying Eq. 3.5 by the Reynolds number results in an expression for *fRe* product in terms of u_s and λ.

$$f\,\mathrm{Re} = \frac{8\tau_w D_h}{\mu \bar{U}} = \frac{8u_s D_h}{\lambda \bar{U}} \tag{3.6}$$

The above equation is important since it can be modified to obtain various expressions for slip length or slip velocity and will be utilized further below.

3.1 Pressure-Driven Flow

The definition of Darcy friction factor for fluid flow through a channel in terms of the applied pressure drop can be found in any undergraduate fluid mechanics textbook. It can also be used in micro-channels with any surface geometry. Although it can be written in many forms, a common expression for a fully developed channel flow is [15]

$$f = -\frac{2D_h}{\rho \bar{U}^2}\frac{\Delta P}{W} \tag{3.7}$$

where ΔP is the pressure difference and W is the streamwise channel length-over which the pressure drop exists. The Darcy friction factor f is related to the Fanning friction factor C_f as $f = 4\,C_f$. Multiplying Eq. 3.7 by Re another expression for fRe in terms of pressure drop can be obtained as indicated below

$$f\,\mathrm{Re} = -\frac{2D_h^{\,2}}{\mu \bar{U}}\frac{\Delta P}{W} \tag{3.8}$$

Once the pressure drop over the channel W is known, the above expression can be used to determine the value of fRe.

The channel considered throughout this work consists of two infinite parallel-plates. An expression for the velocity profile for the fully developed flow between two infinite parallel-plates with apparent slip flow at the superhydrophobic surfaces as shown in Fig. # 3.3 can be obtained and is summarized below.

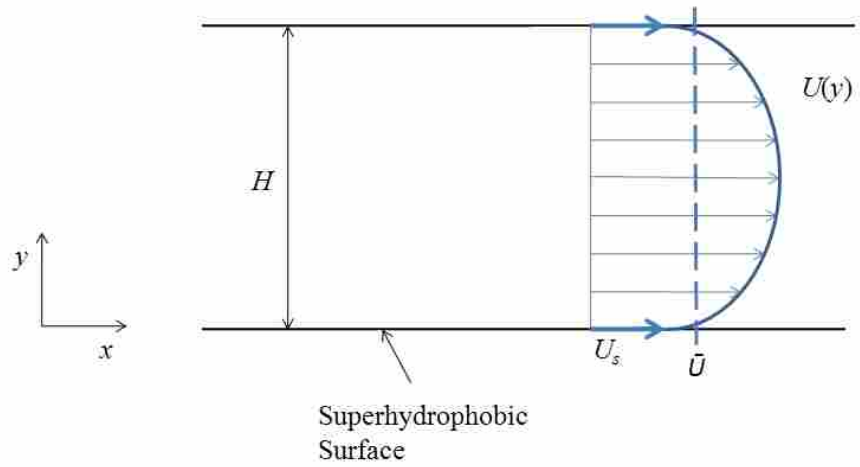

Figure 3.3: Fully developed flow between two infinite parallel-plates with superhydrophobic surfaces.

For fully developed pressure-driven flow between two infinite parallel-plates the velocity profile is parabolic and takes the form

$$u(y) = u_s + ay + by^2 \tag{3.9}$$

where u is the streamwise velocity, y is normal direction to the surface, a and b are constants, and u_s is the slip velocity at the surface. The constants can be determined from the x-momentum equation as shown below for a fully-developed steady laminar flow of a Newtonian fluid with constant viscosity

$$\frac{dP}{dx} = \mu \frac{d^2u}{dy^2} \tag{3.10}$$

Realizing that the pressure gradient dP/dx is constant, this expression can be integrated and solved for the velocity distribution. Applying the appropriate boundary conditions, $u = u_s$ at $y = 0$ and $y = H$ and $du/dy = 0$ at $y = H/2$, the velocity profile within the channel as a function of y can be derived and expressed as

$$u(y) = \frac{1}{2\mu}\frac{dP}{dx}y^2 - \frac{H}{2\mu}\frac{dP}{dx}y + u_s \tag{3.11}$$

This expression can also be used to obtain an area weighted average velocity $\bar{U}$

$$\overline{U} = -\frac{H^2}{12\mu}\frac{dP}{dx} + u_s \tag{3.12}$$

Applying the boundary conditions to Eq. 3.11 and evaluating it at the wall an expression for the slip velocity in terms of the slip length is obtained

$$u_s = -\frac{H}{2\mu}\frac{dP}{dx}\lambda \tag{3.13}$$

Combining the above equation with Eq. 3.6 will result in the expression for *fRe* in terms of the pressure gradient Eq. 3.8 mentioned previously which shows a direct relationship between *fRe* and the pressure gradient.

Substitution of Eq. 3.13 into Eq. 3.12 and combining the result with Eq. 3.6 yields the following useful expression for the *fRe* in terms of the slip length λ.

$$f\,\mathrm{Re} = \frac{8}{\left(\frac{1}{12} + W_m\frac{\lambda}{W}\right)} \tag{3.14}$$

Since the total width considered W corresponds to the width of one post (or rib) W_s and a cavity module width W_c as illustrated in Fig. # 1.5, and by using the definition of the relative module width W_m from Eq. 1.7 the above equation can also be written as

$$f\,\mathrm{Re} = \frac{96}{\left(1+12\frac{\lambda}{D_h}\right)} \tag{3.15}$$

where D_h is the hydraulic diameter. From this expression it is evident that *fRe* is indeed inversely proportional to both the slip length λ and the relative module width W_m. In the case of no-slip flow where $\lambda = 0$, the constant value of *fRe* = 96 is returned. It is important to note that Eq. 3.15 only holds for the non-wetting scenarios and that if the cavities are wetted one needs to consider the volume flow rate of liquid within the cavities to obtain a modified version of equation 3.15, [1].

3.1.1 Previously Developed Correlations for Non-wetting Micro-ribs

For further and future analysis the numerical simulation results from this study could be used to develop correlations for non-wetting micro-posts. Such correlations could serve as approximate or general relationships between some important parameters. Davies [2] and Jeffs [27] performed numerical studies in liquid laminar flow on superhydrophobic surfaces with micro-ribs oriented transverse and longitudinal to the flow direction, respectively. They examined the influence of cavity fraction, cavity depth, and Reynolds number on frictional resistance. Davies [2] obtained and compared results for two different models. As explained in chapter 2, one was zero shear model (ZS) and the other was the coupled liquid-vapor (CLV) model while flat liquid-vapor interface was assumed in both studies. Woolford *et al*. [17] determined the best curve fit and correlation for these results. He also determined Reynolds number based on total width or pitch *W* for Davies' results. He showed that $\mathrm{Re}_W = \frac{\rho \bar{U} W}{\mu}$ was more effective in determining the influence of *Re* on apparent slip length than Reynolds number based on hydraulic diameter. The apparent slip length correlations presented by Woolford *et al*. for the transverse and longitudinal cases were as follows:

$$\frac{\lambda_{\perp}}{W} = \frac{1}{2\pi} \ln[\sec(\frac{F_c \pi}{2})] \left[c_1 + c_2 \left(\frac{\mathrm{Re}_W{}^{c_3}}{\mathrm{Re}_W{}^{c_3} + c_4{}^{c_3}} \right) \right] \tag{3.16}$$

$$\frac{\lambda_{\parallel}}{W} = \frac{1}{\pi} \ln[\sec(\frac{\pi F_c}{2})] \left(1 - e^{-5\left(\frac{d}{W_c}\right)^{0.7}} \right) \tag{3.17}$$

where $\lambda_{\perp}$ and $\lambda_{\parallel}$ are apparent slip lengths for the transverse and longitudinal flow, respectively, d is the cavity depth, and c_1 through c_4 are constants. Woolford *et al*. [17] obtained similar relationships for the scenarios where the cavities are wetted. The values of the constants that were used by Woolford *et al*. are included in Table 3.1.

Table 3.1: Values for the coefficients in Eq. 3.16 for the ZS model, Woolford et al. [17].

	C1	C2	C3	C4
Zero Shear Stress Model (ZS)	1.08	-0.91	1.3	2.55

It is important to note that the reason Re_W does not appear in Eq. 3.16 is that in the longitudinal case the apparent slip length is independent of the Reynolds number. Similar correlations for micro-posts cannot be found presently in the literature and their future development would be a useful addition to this field of study.

3.2 Couette Flow

The differences between pressure- and shear-driven flows in macro-channels are well known. However, in order to illustrate the differences between Couette flow over superhydrophobic surfaces (slip flow) and hydrophilic surfaces (no-slip flow), it is helpful to review and develop some useful relationships for each case separately.

3.2.1 No-slip Flow

Figure 3.4 is a schematic diagram of a typical Couette flow scenario for two infinite parallel plates. The bottom plate is stationary while the top plate moves with a constant velocity,

U. The distance between the plates is *H*/2 which is equal to half the channel height used in the pressure-driven flow cases considered previously.

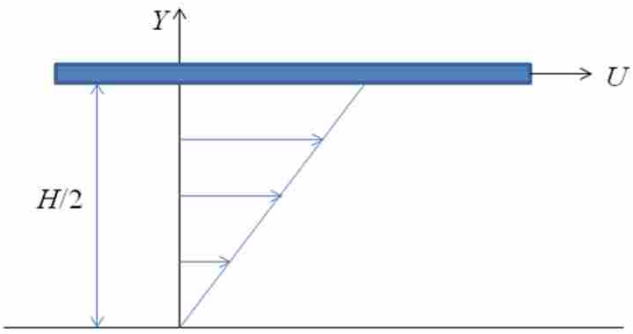

Figure 3.4: Schematic diagram of Couette flow between parallel plates with bottom plate fixed and upper plate moving.

Using the simplified x-momentum equation for steady laminar flow of a Newtonian fluid and appropriate boundary conditions the following linear velocity profile for the fluid is obtained:

$$u(y) = \frac{2y}{H}U \tag{3.18}$$

Deriving this equation with respect to *y* and combining it with equations 1.1 results in an expression for the wall shear stress

$$\tau_w = \frac{2\mu U}{H} \tag{3.19}$$

Substituting the above expression into the definition of the Darcy friction factor Eq. 3.5 and multiplying by the Reynolds number to obtain

$$f\,\mathrm{Re} = \frac{16D_h}{\mu}\frac{\tau_w}{U} \tag{3.20}$$

recognizing that the average fluid velocity for no-slip Couette flow is $\bar{U} = 0.5U$ (due to the linear velocity distribution) and $D_h = H$ yields $fRe = 32$ which is different from the fRe value of 96 for the pressure-driven flow cases.

3.2.2 Slip Flow

When the bottom plate is a superhydrophobic surface the liquid exhibits apparent slip and the no-slip condition no longer applies. The schematic diagram for this situation is illustrated in Fig. # 3.5:

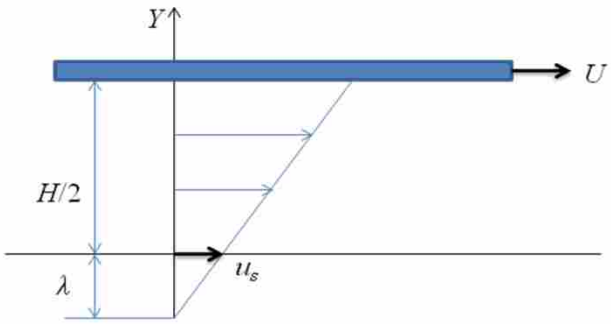

Figure 3.5: Schematic diagram of Couette flow between parallel plates where slip prevails at the stationary bottom plate while the top plate is moving and has no slip.

The average velocity in this case is $\bar{U} = 0.5(U + u_s)$ and the expression for velocity profile $u(y)$ as a function of wall-normal direction y is as follows:

$$u(y) = \frac{2y}{H}\left(U - u_s\right) + u_s \tag{3.21}$$

and the wall shear stress can be expressed as

$$\tau_w = \frac{2\mu(U - u_s)}{H} \tag{3.22}$$

Substituting this expression into Eq. 3.6 for τ_w yields a new equation for *fRe* in a slip Couette flow scenario in terms of plate velocity *U*, the slip velocity u_s, and the average velocity $\bar{U}$

$$f\,\mathrm{Re} = \frac{16(U - u_s)}{\bar{U}} \tag{3.23}$$

Using the fundamental relationship between u_s and λ given in Eq. 3.2 with the derivative of the velocity distribution Eq. 3.21, an expression for u_s in terms of λ for slip Couette flow can be obtained

$$u_s = \frac{2\lambda U}{2\lambda + H} \tag{3.24}$$

This equation and the expression for $\bar{U}$ mentioned above can be substituted into Eq. 3.23 to derive an equation for *fRe* in terms of the slip length and the relative module width for the slip Couette flow

$$f\,\mathrm{Re} = \frac{8}{\frac{1}{4} + W_m \frac{\lambda}{W}} \tag{3.25}$$

This expression is similar to Eq. 3.14 and it shows the relationship between *fRe* and the relative module width W_m and the normalized slip length λ/W for slip Couette flow, where $\lambda = 0$ returns the expected no-slip value of 32 for *fRe*.

The expressions 3.14 and 3.25 will be used in Ch. 5 to evaluate the effects of important parameters such as W_m and F_c on frictional resistance and the slip length in creeping flow regimes. They are also useful in determining the influence of *Re* on frictional resistance and for

comparison purposes with the previously published results for longitudinal and transverse micro-ribs. The validity of these relationships could also be investigated with the numerical simulation results obtained in this study.

4 METHODOLOGY

Three-dimensional numerical simulations were performed to investigate the influence of the governing parameters on the flow through parallel-plate micro-channels with post patterned superhydrophobic walls. Both pressure and shear driven flows were considered. The top and bottom walls of the channel were considered to exhibit micro-post features. The main parameters explored consisted of the cavity fraction F_c, the relative module width W_m, the Reynolds number *Re*, the post aspect ratio *AR*, and the type of driving force for the flow. The commercial software package FLUENT version 6.3 was used for all simulations. For cases where W_m was very small simulations were performed using the supercomputer Marylou as these cases required significant computation time. This chapter includes the assumptions used in the model development and addresses their validity and appropriateness. Further, the geometry, the boundary conditions, the governing equations, numerical grid, convergence criteria, grid independence process, and the solver employed are all discussed in this chapter.

4.1 Model Assumptions

Since there are no closed form exact solutions to the governing equations for the scenarios of interest here, a numerical approach with correct models and simplifying assumptions is employed to yield a solution. The following is a complete list of all the assumptions that were made in this work:

a. Constant transport properties (density and viscosity)

b. Steady laminar flow

c. No body forces

d. Newtonian fluid

e. Periodically fully developed flow

f. Flow through two symmetric infinitely wide parallel plates

g. Fluid behaves as a continuum

h. No-slip flow over solid surfaces

i. Shear-free flow at the liquid-gas interface over the cavities

j. Idealized flat liquid-gas interfaces

The above assumptions were carefully made to simplify the governing equations. Assumptions a-e are typically used for micro-channel flow and need no further discussion. Assumption f is appropriate since the height of the channel is usually more than two orders of magnitude smaller than other dimensions for micro-scale flows. Application of the Navier-Stokes equations requires continuum behavior of the fluid which implies that the Knudsen number, *Kn*, must be less than or equal to 0.1. The definition of *Kn* is $Kn = l/L$ where l for liquids is the distance between molecules and L is a characteristic length scale of the flow. For liquids the molecular mean free path, l, is of the order of 10^{-7} mm and for our purposes L is of the order of 10^{-3} mm. As a result *Kn* is of the order of 10^{-4} which confirms the validity of the continuum assumption.

It was mentioned in section 1.3 that the shear-free and the flat liquid-gas interface assumptions are related to the physics of liquid and gas behavior at the interface. In the non-

wetting or Cassie situation where a stable meniscus is formed at the liquid-gas interface the shear stress is not identically zero [15]. However, the work of Lee *et al*. showed that in the case of micro-rib patterned surfaces the average interfacial shear stress is more than two orders of magnitude smaller than the average shear stress at the liquid-solid interface [24]. Similar behavior is expected for micro-post patterned surfaces. Two different methods have been explored previously for the shear stress at the liquid-gas interface [15]. The first is by assuming zero-shear (ZS) at the interface and the other is by matching the shear stress and the velocity of the liquid and gas at the interface which is referred to as coupled liquid-vapor (CLV) model. As discussed in section 2.2.1, Maynes *et al*. [15] compared both methods in their investigation of parallel micro-ribs aligned transverse to the flow direction. They showed the zero-shear assumption always under-predicts the overall frictional resistance, and at high cavity fractions ($F_C \rightarrow 0.95$) this difference was more substantial. Although according to Maynes *et al*. the zero-shear model is not as accurate as the coupled liquid-vapor model, in our research the zero-shear assumption was applied at the liquid-gas interface since the number of previous works addressing the micro-post geometry is limited. The present results could serve as a basis for further analysis and consideration of the cavity dynamics. In their work Maynes *et al*. also demonstrated that the flat interface assumption was indeed justified and accurate for all realistic scenarios. They employed a parabolic meniscus interface model to account for meniscus curvature. This model resulted in a maximum increase of about 4.2% in the friction factor compared with that of a flat interface model. Therefore, it can be concluded that the flat interface assumption should be adequate for most cases. However, the difference between these two models could also be investigated in the future for surfaces with micro-post patterning.

4.2 Three-Dimensional Numerical Model

For all numerical simulations the 3-D computational domain as shown in Fig. # 4.1 was chosen. A finite volume approach was employed to model the periodically fully-developed flow through an infinitely wide (z-direction) parallel-plate channel for steady, laminar, and constant property conditions. The coupled continuity and Navier-Stokes equations given below for an incompressible Newtonian fluid were solved numerically.

$$\frac{\partial u}{\partial x}+\frac{\partial v}{\partial y}+\frac{\partial w}{\partial z}=0 \tag{4.1}$$

$$\rho\left(u\frac{\partial u}{\partial x}+v\frac{\partial u}{\partial y}+w\frac{\partial u}{\partial z}\right)=\mu\left(\frac{\partial^2 u}{\partial x^2}+\frac{\partial^2 u}{\partial y^2}+\frac{\partial^2 u}{\partial z^2}\right)-\frac{\partial p}{\partial x} \tag{4.2}$$

$$\rho\left(u\frac{\partial v}{\partial x}+v\frac{\partial v}{\partial y}+w\frac{\partial v}{\partial z}\right)=\mu\left(\frac{\partial^2 v}{\partial x^2}+\frac{\partial^2 v}{\partial y^2}+\frac{\partial^2 v}{\partial z^2}\right)-\frac{\partial p}{\partial y} \tag{4.3}$$

$$\rho\left(u\frac{\partial w}{\partial x}+v\frac{\partial w}{\partial y}+w\frac{\partial w}{\partial z}\right)=\mu\left(\frac{\partial^2 w}{\partial x^2}+\frac{\partial^2 w}{\partial y^2}+\frac{\partial^2 w}{\partial z^2}\right)-\frac{\partial p}{\partial z} \tag{4.4}$$

u is the streamwise (x) velocity, v is the wall-normal (y) velocity, w is the lateral (z) component of velocity, P is the static pressure, ρ is the liquid density, and μ is the dynamic viscosity of the liquid. Equations 4.2-4.5 were solved numerically for the computational domain illustrated schematically in Fig. # 4.1.

Figure # 4.1 is a 3-D representation of a few square micro-posts on a substrate with appropriate dimensions labeled as defined in Fig. # 1.5. The posts are equally spaced and because of symmetry the computational domain covers half of a post and half of a neighboring cavity in the transverse direction. In the streamwise direction the computational domain has a length that extends from the trailing edge of a post to the trailing of the next post. The

computational domain height extends from the top of the posts ($y = 0$) to the channel centerline $y = H/2$. The liquid flows over the posts in the direction illustrated in the figure without penetrating into the cavities. Again, the shape of the meniscus at the liquid-vapor interface was assumed to be flat, representing the ideal non-wetting and perfectly hydrophobic surfaces. This assumption serves as a basis for comparison with other models.

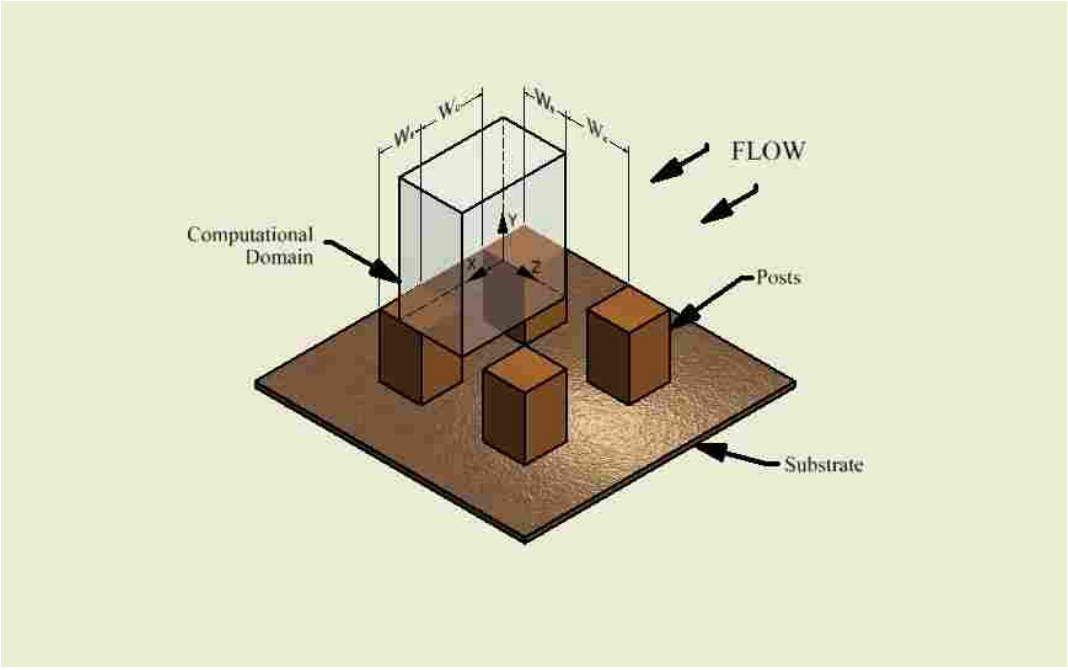

Figure 4.1 : Illustration of the 3-D computational domain employed over the micro-post patterned superhydrophobic surface with the appropriate coordinate system.

The boundary conditions employed were as follows. For pressure-driven flow the symmetry boundary condition was imposed at the channel center-line $y = H/2$ and the lateral sides of the solution domain. However, for the Couette flow situations the channel center-line boundary condition was allowed to be a moving wall in the streamwise direction. No-slip and no-penetration conditions were specified for the wall representing the post surface and zero-shear and no-penetration were specified at the liquid-cavity interfaces. The conditions at the upstream

and downstream surfaces of the computational domain were chosen to be periodic. This type of boundary condition ensures that *u*, *v*, *w*, and their derivatives are equal at corresponding locations along these two surfaces. The specific boundary conditions for the computational domain are given mathematically as follows:

1. Boundary conditions at $y = 0$
   a. $u = 0$ for $W_c \le x \le W_c + W_s$ and
   b. $v = w = 0$ for all *x* and *z*
   c. $\frac{\partial u}{\partial y} = 0$ for and $0 \le x \le W_c$
2. Boundary conditions at $y = H/2$ and all *x* and *z*
   a. For the pressure-driven flow scenarios
      i. $\frac{\partial u}{\partial y} = \frac{\partial v}{\partial y} = \frac{\partial w}{\partial y} = 0$
   b. For the Couette flow scenarios
      i. $u = U$
      ii. $v = w = 0$
3. Boundary conditions at $z = 0$ and $z = w_s$ and all *x* and *y*
   a. $\frac{\partial u}{\partial z} = \frac{\partial v}{\partial z} = \frac{\partial w}{\partial z} = 0$
4. Periodic boundary conditions at $x = 0$ and $x = w_s + w_c$
   a. $u(0, y, z) = u(w_c + w_s, y, z)$
   b. $v(0, y, z) = v(w_c + w_s, y, z)$

c. $w(0,y,z) = w(w_c + w_s, y, z)$

d. $\frac{\partial u}{\partial x}(0,y,z) = \frac{\partial u}{\partial x}(w_c + w_s, y, z)$

e. $\frac{\partial v}{\partial x}(0,y,z) = \frac{\partial v}{\partial x}(w_c + w_s, y, z)$

f. $\frac{\partial w}{\partial x}(0,y,z) = \frac{\partial w}{\partial x}(w_c + w_s, y, z)$

The periodicity condition provides that the velocity distribution within the domain defined in Fig. # 4.1 repeats from module to module, such that $u(x) = u(x+W) = u(x+2W) = ...$ and $w(z) = w(z+W) = w(z+2W) = ...$, where, *W* is the micro-post/cavity module width as illustrated in Fig. # 1.5. Although the pressure itself is not periodic, the pressure drop between modules is periodic such that the pressure drop from module to module can be expressed as $\Delta p = p(x) - p(x+W) = p(x+W) - p(x+2W) = ...$ The pressure gradient driving the flow may thus be represented as the gradient of a linearly-varying component and the gradient of a module-periodic component, $\Delta p = \alpha + \Delta\bar{p}(x)$. Thus α is the linearly-varying component of pressure, and $\Delta\bar{p}(x)$ is the periodic pressure whose distribution repeats from module to module. Computationally, either the module-to-module pressure drop α, or the total mass flow rate through the micro-channel may be imposed. In this study the mass flow rate in the micro-channel was specified for each simulation, and α was determined iteratively by updating its value through the course of the iterations. Corrections to the value of α were made during the iterations based on the difference between the actual and desired mass flow rate.

Liquid water was used as the fluid with constant thermodynamic properties density and viscosity ρ = 998.2 kg/m^3 and μ = 0.001003 kg/m-s, respectively. The research was conducted in three phases. Phase one consisted of analysis and simulations for pressure-driven flows for square micro-posts. Phase two considered shear-driven or Couette flows for square micro-posts. Phase three considered pressure-driven flows for surfaces with rectangular micro-posts of varying aspect ratios. There were a total number of 144 different scenarios considered. Since there were some modest differences in setting up the models for each of these three phases, they are explained in detail in the subsequent sections. The commercially available software, GAMBIT, was used to define the geometry and the initial mesh. For the periodic boundary conditions appropriate edges and faces needed to be linked prior to meshing. Initially, a structured coarse mesh was used for all cases. Along the edges and near the surfaces where gradients were presumed to be high a finer mesh was employed.

4.2.1 Pressure-Driven Flow for Square Micro-posts

With the boundary conditions and assumptions described in the previous section the problem was solved using the commercial solver FLUENT version 6.3. For a specified Reynolds number an average velocity was determined and mass flow rate $\dot{m}$ through the channel was specified as shown below:

$$\dot{m} = \rho A_{cr} \overline{U} = \frac{A_{cr} \mu \,\mathrm{Re}}{D_h} \tag{4.5}$$

where A_{cr} is the cross sectional area for the computational domain, $\bar{U}$ is the average streamwise velocity, and D_h is the hydraulic diameter. Using this specified mass flow rate, iterations of the solver were performed until the solution was converged and the average wall shear-stress ceased

changing for over two thousand iterations. The output value for the pressure drop $\Delta P/W$ was substituted in Eq. 3.8 to calculate the friction factor-Reynolds number product *fRe* for each scenario. The *fRe* value can then be used to calculate the slip length from Eq. 3.14 for the specific scenarios.

To benchmark the numerical approach a simulation for a classical parallel-plate channel with no-slip walls was performed. The results yielded *fRe* = 95.8, which is within 0.2% of the classical value of 96. Also, simulations on transverse and longitudinal micro-ribs were performed to be used as benchmarks for our initial results obtained for micro-posts at *Re* = 1and for comparison purposes with Davies [2] and Jeffs [27] results for transverse and longitudinal ribs. The results proved to have similar general patterns for the *fRe* and the slip length, but in the meantime noteworthy differences were observed which will be discussed in the Results section.

The parameter ranges explored for pressure-driven flow are summarized in Table 4.1. Specifically simulations were performed to quantify the influence of F_c, W_m, and *Re* on the overall flow physics and average frictional resistance.

Table 4.1 : Ranges reported for F_c, W_m, and *Re* in pressure-driven flow scenarios.

Parameter	Range
F_c	0.0-0.9998
W_m	0.01-1.5
Re	1-2500

4.2.2 Shear-Driven or Couette Flow for Square Micro-posts

Shear driven flow was investigated to document whether the apparent slip length is dependent on the imposed velocity distributions. For this situation the boundary condition at the top control surface was specified as a moving wall with constant velocity equal to the average velocity applied in the pressure-driven cases at $Re = 1$. For both the pressure-driven and Couette flow scenarios the D_h was obtained in the same manner. Also the height of the channel in the Couette flow cases was set equal to half the height used for the pressure-driven flow models. For these scenarios the imposed pressure drop did not need to be specified in the model.

For each case the average wall shear stress $\overline{\tau_w}$ was calculated by integrating over the entire plane at $y = 0$ and $\bar{U}$ was determined from the expression given in Sec.3.2.2. Similar to the pressure-driven flow cases, in order to confirm the accuracy of the model, a simulation was performed for a classical channel with no-slip surfaces. The typical fRe result obtained was equal to 31.88, which is within 0.375% of $fRe = 32$ for the classical Couette flow. Several simulations over the following ranges of cavity fraction F_c and relative module W_m width were performed:

Part A. $Re = 1$, $W_m = 0.1$ for the range $0.0 \leq F_c \leq 0.9998$

Part B. $Re = 1$, $W_m = 0.01, 0.1, 1$, and $F_c = 0.75, 0.95, 0.999$

The results from all simulations are included and discussed in chapter 5. Extreme care was required while performing all numerical simulations, to ensure convergence and grid independence while avoiding extra and unnecessary iterations which could eventually result in accumulation of round-off error or unstable results.

4.2.3 Pressure-Driven Flow for Rectangular Micro-posts

In order to investigate the effect of micro-post aspect ratio, simulations were performed for a modest number of rectangular micro-posts. The aspect ratio was defined as the ratio of the length and width of the rectangular post, $AR = L/W$. The post aspect ratios considered were 1/8, 1/4, 1/2, 2, 4, and 8. The other parameters were specified as $Re = 1$, $W_m = 0.1$ with two different values of the cavity fraction, $F_c = 0.75$ and 0.95. For $AR = 2$, 4, and 8 the flow direction was perpendicular to the shorter side of the rectangles, Fig. # 4.2(a), whereas for $AR = 1/8$, 1/4, and 1/2 it was perpendicular to the longer side of the rectangles, Fig. # 4.2(b).

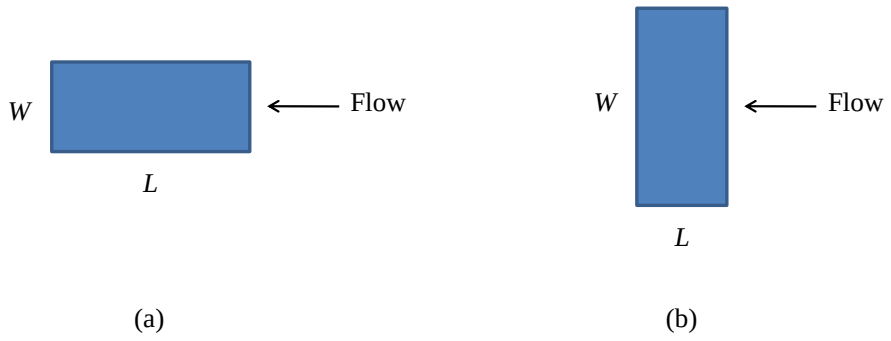

Figure 4.2: Schematic diagram illustrating the direction of flow over the rectangular micro-posts for the two cases (a) *AR* = 2, 4, and 8, (b) *AR*=1/8, 1/4, and 1/2.

The purpose was to see if there would be any noticeable difference between the two orientations and to be able to characterize their effects on frictional resistance. The results would be compared with results for longitudinal and transverse ribs and the present micro-post results. The driving force for these simulations was assigned to be pressure-driven and the assumptions and boundary conditions were similar to those employed for square micro-posts.

4.3 Grid Information and the Solver

The governing equations 4.1 through 4.4 constitute the continuity equation and three non-linear second-order partial derivative momentum equations. The three dimensional velocity and pressure fields are unknown. FLUENT was used to obtain a numerical solution for such a coupled system of equations. The finite volume approach was implemented in which the computational domain is discretized into small finite volumes and the governing equations are integrated over these volumes to a system of algebraic equations. The equations are solved through an iterative procedure. Because of the non-linearity of the governing equations an under relaxation factor is utilized to facilitate the convergence of the iterations. Appropriate criteria were used to monitor convergence of the solution. The pressure based implicit formulation available in FLUENT was chosen for both the pressure-driven and the shear driven situations. However, for the pressure-driven problems the mass flow rate was specified while for the Couette flow scenarios the top wall velocity and zero pressure gradient were provided. The pressure-velocity coupling was handled by using the SIMPLE scheme available in FLUENT for all cases.

Regarding discretization, the “Standard Option” scheme for pressure and the “First Order Upwind” scheme for momentum were employed. The under-relaxation factors that worked effectively were typically 0.3 for pressure and 0.7 for the momentum equations. Iterations were performed until a converged solution was obtained. The average shear stress on the solid surface, pressure gradient, and residuals were used to monitor convergence. Initially a coarse mesh of about 12000 to 50000 cells was deployed depending on the specific scenario. Iterations continued until changes in the average shear stress over the solid surface for the last 2000 iterations were less than 0.1%. Subsequently the mesh was refined using the adaptive grid

refinement tool available in FLUENT, which automatically refines the mesh in regions with high gradients in the *x*, *y*, and *z* velocities. During each refinement process a threshold for velocity gradients was specified. Refinement at each threshold was performed several times until the solution ceased to change with grid refinement. The threshold was reduced systematically by one order of magnitude each time the refinement was applied, and simulations were performed until changes in the converged values of average shear stress over the solid surface and the *fRe* product were less than 0.1%. In order to achieve mesh independence in some cases the threshold was reduced down to 10^{-13}. The total number of cells, depending on the case, for converged solutions ranged between 50,000 and over 1,500,000. Throughout the entire numerical simulations the minimum and maximum numbers of iterations performed varied from 5000 to $2x10^{6}$.

5 RESULTS

3-D numerical simulations of fully developed steady-state liquid laminar flow through a rectangular micro-channel with superhydrophobic walls were performed. The channel was modeled as two infinite parallel plates resembling superhydrophobic surfaces with micro-post pattern geometries. The research was performed in three phases, 1) pressure-driven flow with square micro-posts, 2) Couette flow with square micro-posts, and 3) pressure-driven flow with rectangular micro-posts at various aspect ratios. The influences of the important parameters such as F_c and W_m on frictional resistance reduction were explored and are presented here in graphical forms. Phase (1) of this study also explored the effect of varying *Re* on frictional resistance.

To ensure the models were set up correctly for all three phases of the research, simulations were first performed for entirely solid walls on the top and bottom surfaces of the computational domain. The obtained results yield *fRe* = 95.8 for the pressure-driven classical channel flow case, and *fRe* = 31.88 for the classical Couette flow situation. These results are within 0.2% of the no-slip scenario of 96 for the classical channel flow and 0.4% of the no-slip Couette flow which validate the accuracy of the modeling approach used. All of the analyses were performed for liquid water as the fluid while assuming non-wetting scenarios with a flat zero-shear model at the liquid-vapor interface over the cavities. This chapter contains results of all the simulations for the three phases of the research. Previously published results for

longitudinal and transverse micro-ribs and scaling-law results for micro-posts are used as benchmarks in some illustrations and graphs.

5.1 Pressure-driven Flow with Square Micro-posts

As explained in chapters 3 and 4, fully developed liquid laminar flow confined within two infinite parallel-plates was employed for all the scenarios. In classical cases where no-slip conditions prevail at the walls, the velocity profile is parabolic varying from zero at the walls to a maximum at the centerline of the channel. As stated before, in cases where the walls are superhydrophobic apparent slip exists at the walls. The amount of slip depends on parameters which will be discussed later in the chapter. Phase (1) of this study considered pressure-driven fully developed liquid laminar flow over the superhydrophobic surfaces. Figure 5.1 illustrates a typical streamwise velocity contour at the wall surface (y = 0 plane) of the channel for which Re = 1, F_c = 0.85, and W_m = 0.1. The velocity is higher over the cavity regions where slip flow condition exists. The regions with highest velocity are illustrated in red. As expected, the streamwise velocity is greatest in the region of the cavity mid-span. Near the surface of the post at y = 0, the velocity tends to slow down due to higher shear stress and the no-slip condition at the liquid-solid interface. In order to satisfy the conservation of mass principle and from the microscopic point of view, the liquid within the considered computational domain must speed up locally in the cavity regions between the posts, due to the deceleration over the solid post surfaces. Therefore, it is evident that the reduction in liquid-solid contact area is responsible for this increase in liquid momentum over the cavity regions. The non-zero velocity at y = 0 over the cavity regions is the slip velocity as discussed previously. The overall effect of this slip from the macroscopic viewpoint is an apparent or net slip velocity over the entire superhydrophobic

surface. The net or surface area-weighted average slip velocity for this particular scenario was about 32.8% of the average liquid velocity through the channel. A direct result of the apparent slip velocity is an overall increase in momentum flux and volume flow rate of the liquid through the micro-channel, for a specified driving force.

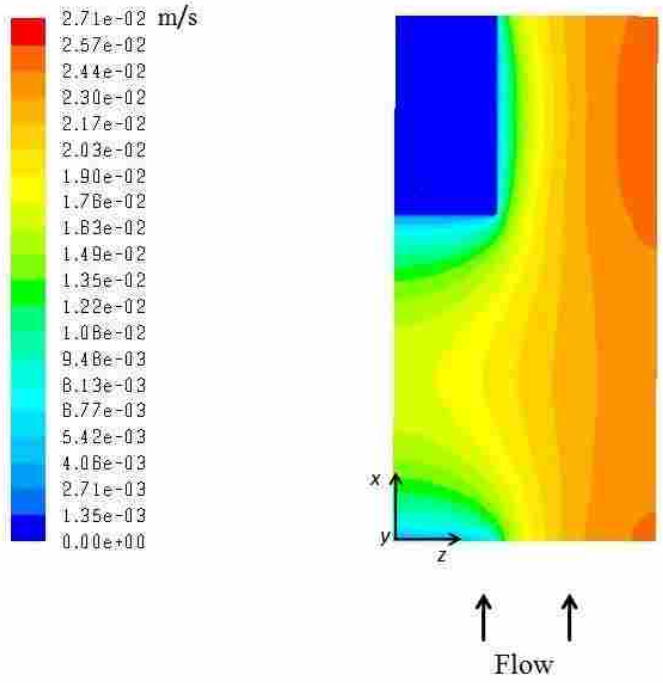

Figure 5.1: A typical streamwise velocity contour (m/s) at y = 0 plane for pressure-driven flow over a superhydrophobic surface exhibiting square micro-posts with Re = 1, W_m = 0.1, F_c = 0.85.

Considering the overall surface geometry and its effect on the liquid flow through the channel, it is useful to mention that the arrays of posts create a checkerboard type surface as illustrated in Fig. # 5.2. As a result, there tends to be a series of cavity "canals" parallel, and cavity regions transverse, to the flow. The absence of any solid surface along the cavity canals resembles the cavity regions that exist in longitudinal micro-rib patterned surfaces. Conversely, the presence of the posts create cavity regions between successive posts in the streamwise

direction that should be similar in their effect to the cavity regions that exist in transverse micro-rib patterned surfaces. It is important to redirect one's attention to Fig. # 5.1 to note that the high velocity regions occur within the longitudinal cavity canals, and lower velocities occur inside the transverse cavity regions. As the liquid flows over an array of posts, it encounters a periodic series of slip and no-slip flow conditions, however, the liquid glides over a cushion of air as it flows above the longitudinal cavity canals. Therefore, it would seem logical to conclude that superhydrophobic surfaces with micro-posts should perform somewhere between surfaces that exhibit parallel and transverse micro-ribs. Results obtained at other cavity fractions confirmed that this was indeed the case up to $F_c \approx 0.88$. However, somewhat different behavior was observed at higher cavity fractions. This phenomenon and the effect of surface geometry are discussed in detail later in the chapter. Velocity contours near the edges of the post in Fig. # 5.1 indicate large changes in the streamwise velocity as the liquid approaches the solid surface of the post.

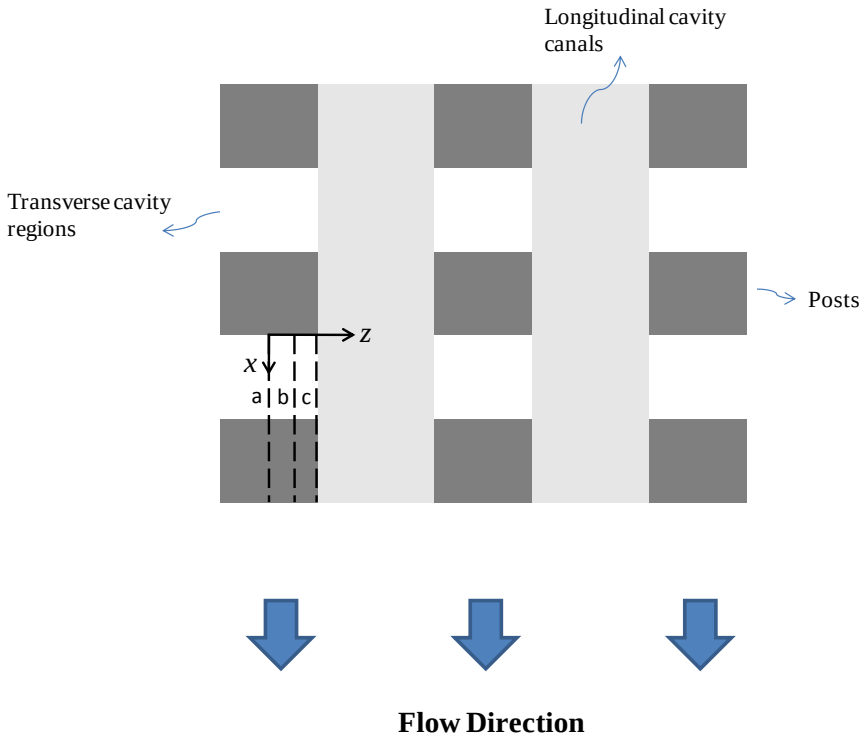

Figure 5.2: Schematic view of a superhydrophobic surface with micro-posts resembling a checkerboard arrangement. Lines a, b, and c correspond to z = 0.0, 0.19, and 0.38.

It is along the edges and at the corners that the velocity gradients are highest compared with other parts of the channel. These increased velocity gradients result from the higher shear stress that prevails along the surface of the posts.

Normalized streamwise velocity variations u/U_{ave} at the plane of the wall (y = 0) at three different lateral locations z = 0, 0.19, and 0.38 are shown in Fig. # 5.3 for the Re = 1, W_m = 0.1, and F_c = 0.85 scenario. u/U_{ave} is shown as a function of x/W, where x is in the flow direction and W is the total post/cavity width. x/W = 0 corresponds to the trailing edge of a post and x/W = 1 is at the leading edge of the next consecutive post. The first curve represents streamwise velocity variation along the mid-section (z = 0 line a in Fig. # 5.2) of a typical cavity/post region, the top curve is the streamwise velocity variation along the edge (z = 0.38 line c in Fig. # 5.2) of

the cavity/post, and the third curve illustrates the streamwise velocity variation along the section (z = 0.19 line b in Fig. # 5.2) halfway between the edge and the mid-section of a cavity/post region at y = 0 within the computational domain. It can be seen that generally all three curves have similar shapes. They appear to vary parabolically, with u/U_{ave} increasing from zero at the trailing edge of a post, until it reaches a maximum at the center of the cavity between two consecutive posts. It then deceases to zero velocity at the leading edge of the next post, and is zero over the entire post surface.

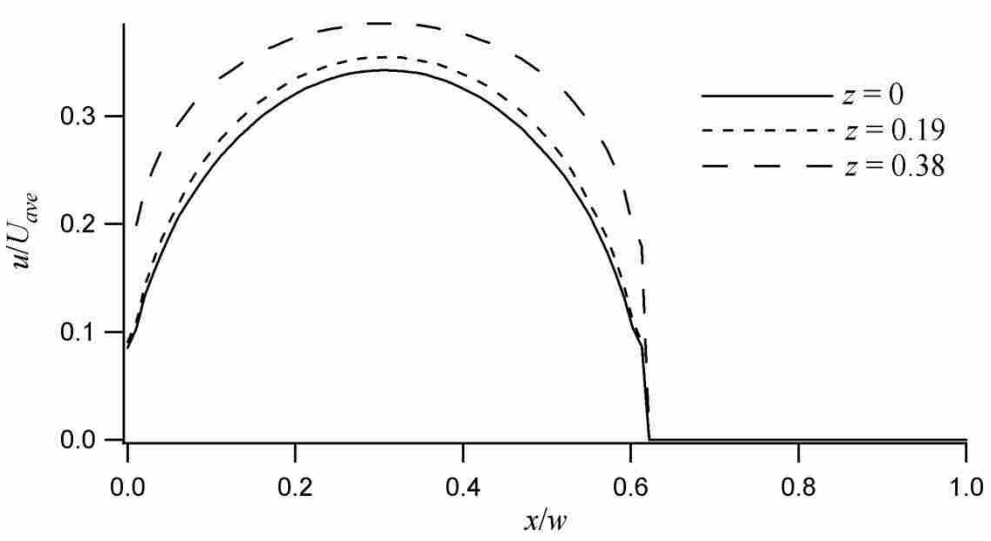

Figure 5.3: Typical normalized streamwise velocity variations at y = 0 and at three different locations on a post for a pressure-driven flow over a superhydrophobic surface exhibiting square micro-posts with Re = 1, W_m = 0.1, F_c = 0.85.

It can be seen in the figure that there is only a small difference (about 5%) between the velocities at z = 0 and z = 0.19. However, there is a more substantial increase (about 15%) in the streamwise velocity along the z = 0.38 or line (c) compared with the velocity along the (z = 0 or line a) post mid-section line.

Average shear stress contours over a typical post at $y = 0$ for the $Re = 1$, $F_c = 0.85$, and $W_m = 0.1$ scenario are illustrated in Fig. # 5.4. Note that only the stress contour on the post surface is shown in this figure, since the shear stress over the entire cavity region is zero. Near the edges, and especially near the corners, much higher shear stress than at other regions of the post exists due to the elevated velocity gradients in these regions.

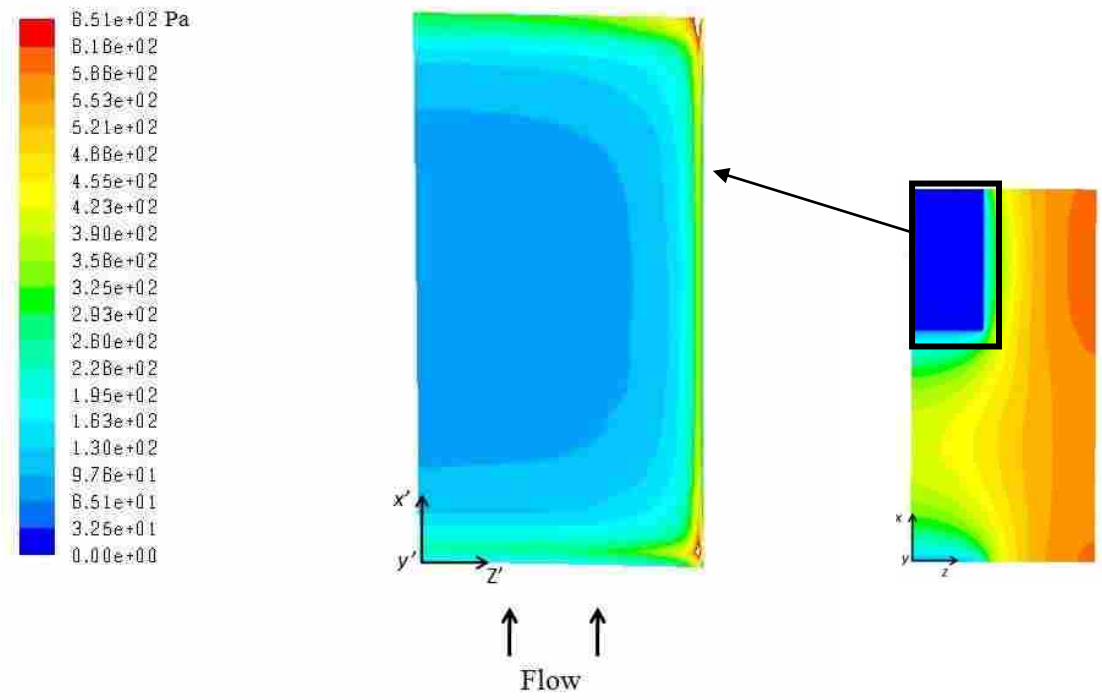

Figure 5.4: Shear stress (Pa) contours at the $y = 0$ plane for a typical square micro-post at $Re = 1$, $F_c = 0.85$, and $W_m = 0.1$.

Altering the shape of the posts by eliminating or reducing sharp edges and corners could potentially reduce the surface shear stress and overall surface friction even further. For example, rounding the sharp corners or even considering cylindrical posts with the same surface area as the square posts would be an interesting exploratory topic for further studies.

Figure # 5.5 is a graphical representation of the variation of shear stress at three different locations on the surface of a typical post. In this figure the wall shear stress, which is normalized by the shear stress for the classical no-slip scenario, is plotted with respect to the streamwise position x, normalized by W, at the same three lateral locations of Fig. # 5.3 (z = 0, 0.19, and 0.38). The z = 0 profile corresponds to the mid-post region, z = 0.38 is along the edge of the post in the streamwise direction, and 0.19 is halfway between the z = 0 and 0.38 locations. It can be seen in Fig. # 5.5 that the three shear stress curves peak at the leading and the trailing edges of the post due to high velocity gradients du/dy at these locations. This increase in velocity gradient is caused by a sudden change in the boundary condition at the surface, which changes from slip flow over the cavity to no-slip flow over the post. The data also show that there is approximately four times as much shear stress along the edge of the post at z = 0.38, as there exists along the mid-post line. Only a slight difference exists between shear stresses at the mid-post (z = 0 line) and the z = 0.19 position. According to Eq. 1.2 this increase in velocity gradient has a direct impact on surface drag or frictional resistance. As it was mentioned in Ch. 1, frictional resistance could be reduced by decreasing the velocity gradient at the wall. Modification of post geometry as discussed above could help in reducing velocity gradients; however, there are other issues and factors that need to be considered.

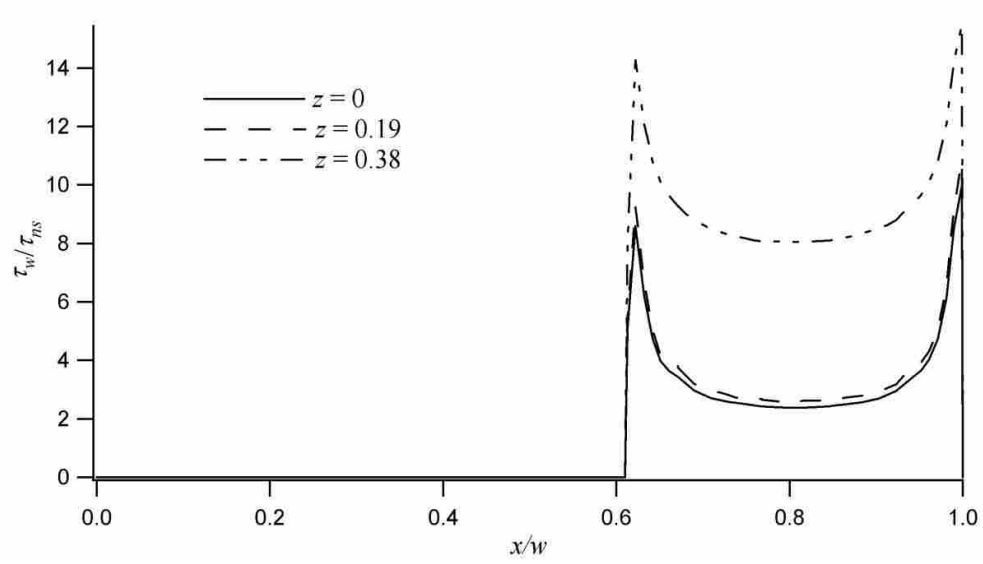

Figure 5.5: Typical normalized streamwise shear stress variations at $y = 0$ and at three different locations on a cavity/post region for a pressure-driven flow over a superhydrophobic surface exhibiting square micro-posts with $Re = 1$, $W_m = 0.1$, $F_c = 0.85$.

Micro-posts can be constructed in various shapes, rectangular, square, cylindrical, and conical to name a few, but it is the overall performance and overall frictional resistance reduction that is important. Practically speaking, issues such as susceptibility to wetting and fabrication should also be considered. In order to examine the influence of geometry on frictional resistance, numerical analysis was performed for a few cases on rectangular micro-posts. Their results will be discussed later in this chapter.

Streamwise velocity profiles were extracted from the numerical results at four locations within the computational domain and are shown in Fig. # 5.6 with black, green, blue, and red arrows. Figure 5.6 provides the normalized streamwise velocity profiles u/U_{ave} above the surface at these four locations for the case discussed above, $Re = 1$, $F_c = 0.85$, and $W_m = 0.1$. The color of the lines in the figure corresponds to the locations indicated by the matching colored arrows. The mean velocity profile U_m, which was obtained by integrating the streamwise velocity over

the entire cross sectional area of the computational domain, is also included in the figure and is shown as the black dashed line.

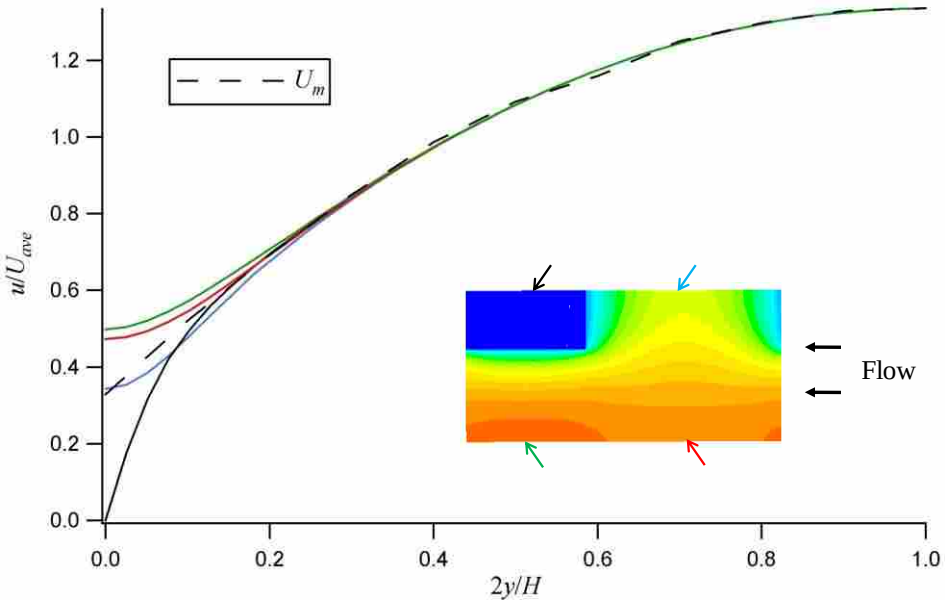

Figure 5.6: Normalized streamwise velocity profiles at four locations within the computational domain over a superhydrophobic surface with square micro-post geometry for the scenario *Re* = 1, F_c = 0.85, and W_m = 0.1.

Figure # 5.6 shows the streamwise velocity u normalized by the area-weighted average liquid velocity through the channel U_{ave} versus the wall normal distance, normalized by half of the channel height $H/2$. The profile above the solid surface of the post (solid black curve) satisfies the no-slip condition at the wall and resembles the usual fully developed laminar flow parabolic profile. For $\frac{2y}{H} \geq 0.3$ the profiles at all four positions merge and are exactly the same in magnitude and shape. However, near the wall ($\frac{2y}{H} \leq 0.3$) the profiles begin to deviate from one another and from the mean velocity behavior. It is important to note that at $y = 0$, the liquid velocity over the cavity regions is non-zero which is an indication of slip at the surface. The maximum slip velocity occurs in a region, shown with a green arrow, between the posts. In this

region, and at $y = 0$, the normalized velocity has the value of 0.5 which is 50% of the average velocity U_{ave}. This implies greater liquid flow through this region of the channel. The red color profile corresponding to the region marked with the red arrow in the inset of the figure is modestly lower near the wall ($\frac{2y}{H} \leq 0.3$) and the green color profile for the region marked with the blue arrow in the inset of the figure has significantly lower value than the profile for the region marked with the green arrow. It is also important to point out that the y-intercept for the mean velocity profile U_m is about 0.33, which is the normalized apparent slip velocity for this scenario.

5.1.1 Influence of Cavity Fraction F_c at $W_m = 0.1$ and $Re = 1$

The main purpose of using superhydrophobic surfaces in micro-channels is to reduce liquid-solid contact area, thereby reducing the frictional resistance between the liquid and the channel wall surface. As some of the solid surface on the channel walls is removed and replaced with pockets (or arrays) of air, the frictional resistance at the channel surface can significantly decrease due to reduced friction between the liquid and the air. In order to examine and quantify (characterize) the relationship between the cavity fraction and the frictional resistance reduction, it is helpful to first observe, discuss, and compare the streamwise velocity contours at the surface of the channel ($y = 0$) at two different cavity fractions, where all other parameters and flow conditions are exactly similar. Fig. # 5.7 is an illustration of such a contour for $F_c = 0.95$, $Re = 1$, and $W_m = 0.1$.

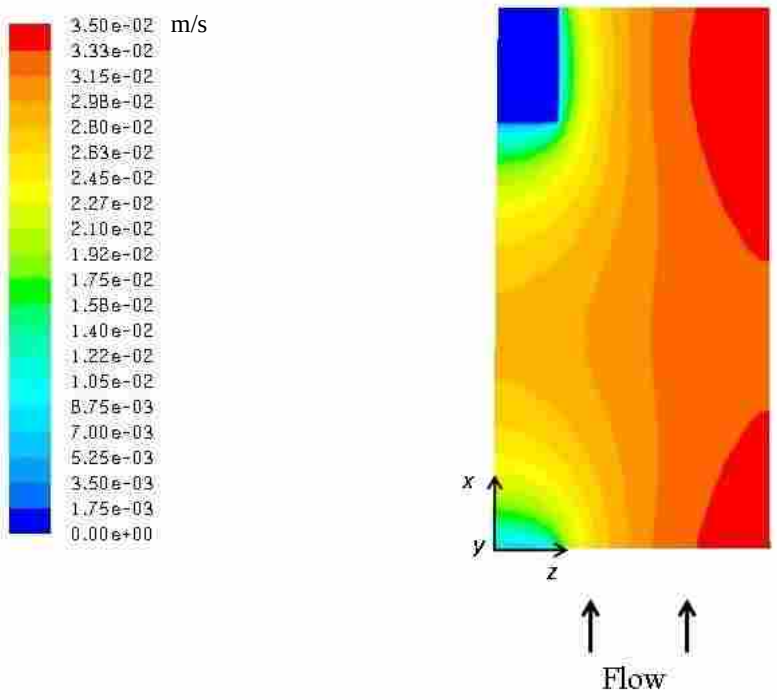

Figure 5.7: Streamwise velocity contours (m/s) at y = 0 for a pressure-driven flow over a superhydrophobic surface exhibiting square micro-posts with F_c = 0.95, Re = 1, and W_m = 0.1.

As expected, this velocity contour is quite similar to the streamwise velocity contour plot obtained for the F_c = 0.85 case and shown in Fig. # 5.1. Although the regions of high and low streamwise velocity for both contours presented in Figs.5.1 and 5.7 are similar, the surface with F_c = 0.95 has larger regions of high streamwise velocity. This phenomenon is logical since at F_c = 0.95 the liquid solid contact area is smaller than in the F_c = 0.85 scenario. As a result, the apparent or overall slip velocity at the surface for F_c = 0.95 should be greater than for the F_c = 0.85 case. Later discussions of apparent slip velocity will also confirm this observation. The magnitudes of the streamwise velocities at y = 0 are included on the left of each contour. It is important to notice that greater streamwise velocity magnitudes were obtained over the entire cavity region for the higher cavity fraction scenario. For instance, the maximum streamwise velocity at y = 0 for the F_c = 0.95 is 0.035 m/s, compared with 0.027 m/s for the surface with F_c

= 0.85. This is an increase of nominally 29.6% compared with the 11.8% increase in cavity fraction. One can conclude that there is a direct relationship between the cavity fraction and the slip velocity, *i.e.*, as cavity fraction is increased the apparent slip velocity is also increased.

Figure # 5.8 provides shear stress contours at the liquid solid interface ($y = 0$) of a micro-post on a superhydrophobic surface with $F_c = 0.95$. Even though the patterns on this shear stress contour are similar to the ones presented in Fig. # 4 for which $F_c = 0.85$, there are some significant differences that are useful to mention. In both figures the magnitudes of the average solid surface shear stress are presented. The maximum shear stress region in Fig. # 5.4 has an average value of 651 Pa, whereas the maximum in Fig. # 5.8 has a magnitude of 1200 Pa. The 11.8 % increase in cavity fraction amounts to a substantial increase of 84% in maximum shear stress over the solid micro-post surface.

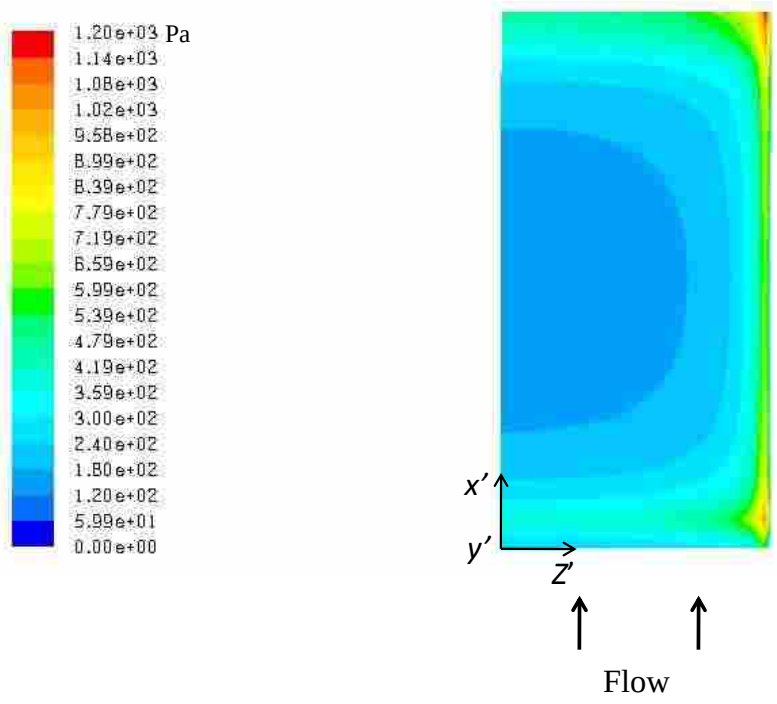

Figure 5.8: Shear stress (Pa) contours at $y = 0$ for a square micro-post at $Re = 1$, $F_c = 0.95$, and $W_m = 0.1$.

This result is also expected, since by decreasing the liquid-solid contact area while keeping all other parameters such as *Re* constant, smaller solid surface will be subjected to the same shear fluid inertia due to the flowing liquid. The natural result is a rise in the micro-post surface shear stress. Because of the tremendous rise in shear stress on the post surface as the cavity fraction is increased, real-life application of such superhydrophobic surfaces could be challenging. In the ideal situation, the durability of the micro-posts is important since any fracture or damage of the posts could make the surface more susceptible to wetting.

In order to verify the consistency of the results, streamwise velocity profiles for the F_c = 0.95 scenario were also obtained and graphed as shown in Fig. # 5.9. Profiles are shown and are color coded to the locations where the profiles correspond. An area weighted mean profile is also shown. The general behavior of the profiles is similar to the F_c = 0.85 case presented in Fig. # 5.6. As discussed before, the liquid-solid interface reduction should result in an increase in apparent slip velocity. From Fig. # 5.9, the y-intercept of the mean profile U_m is 0.56 and is the value obtained by calculating the area-averaged velocity at the y = 0 plane from Fig. # 5.7. Compared with the F_c = 0.85 case, this is a 69.7% increase in normalized apparent slip velocity. The influence of certain important parameters such as cavity fraction on the apparent slip velocity will be discussed later in much more detail in this chapter.

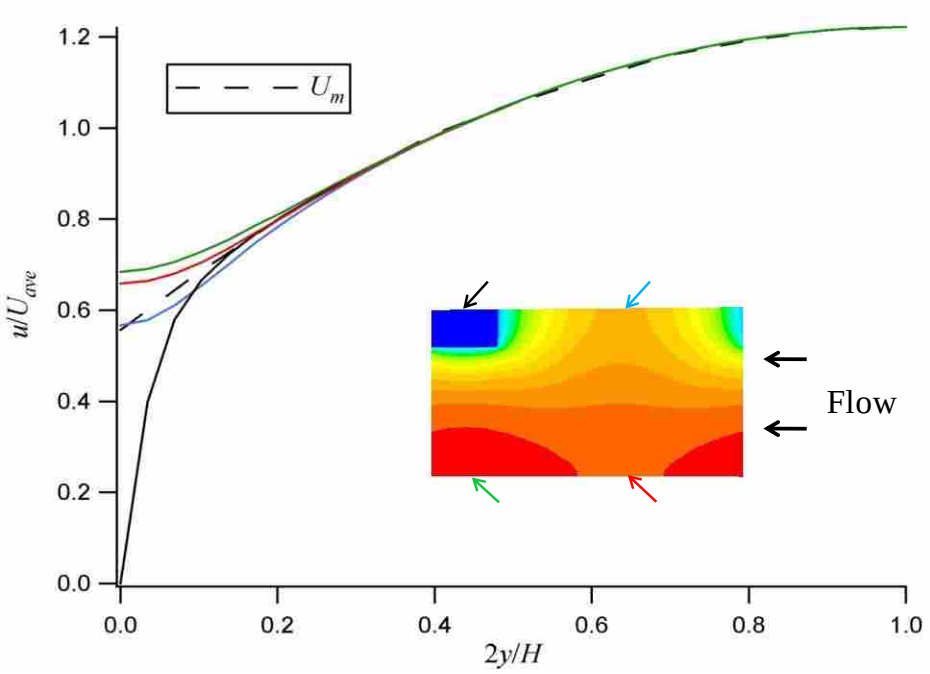

Figure 5.9: Normalized streamwise velocity profiles at four locations within the computational domain over a superhydrophobic surface with square micro-post geometry for the scenario *Re* = 1, F_c = 0.95, and W_m = 0.1. Also shown is the area weighted average or mean

At this point it is appropriate to examine streamwise velocity contours of a very high cavity fraction scenario, and make comparisons with the two previous cases discussed and presented in Figs.5.1and 5.7. Streamwise velocity contours of the F_c = 0.996 scenario at y = 0 are considered and illustrated in Fig. # 5.10. At this high cavity fraction, which is near the limiting case of F_c = 1, similar generalized behavior and patterns to the two cases previously discussed are observed. Again, for these three particular cases all other parameters such as *Re* and W_m were held constant and equal to 1 and 0.1, respectively.

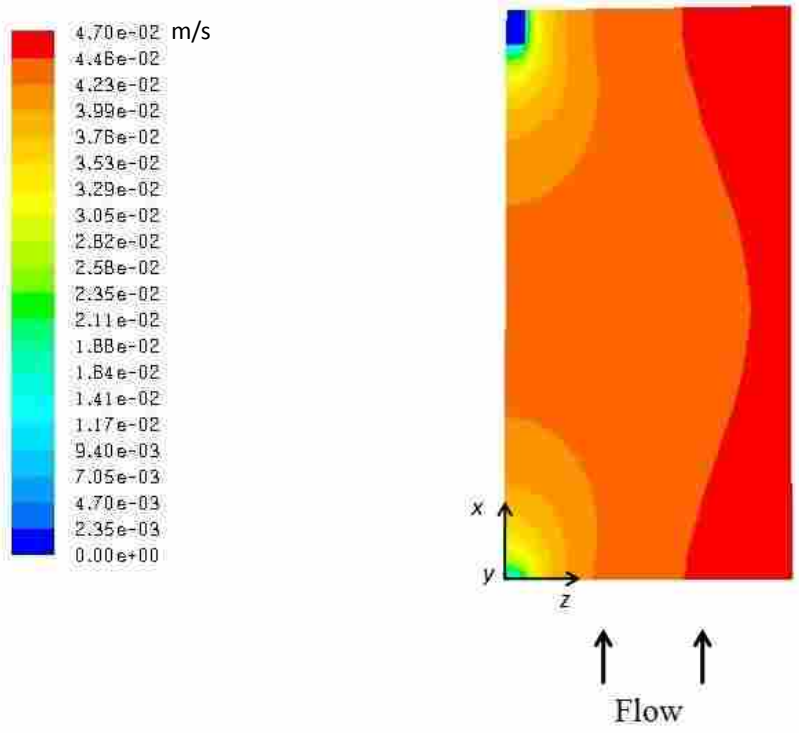

Figure 5.10: A typical streamwise velocity contour (m/s) at $y = 0$ for a pressure-driven flow over a superhydrophobic surface exhibiting square micro-posts with $F_c = 0.996$.

The general pattern and flow characteristics for this scenario are similar to the lower cavity fraction situations $F_c = 0.85$ and 0.95 presented in Figs.5.1 and 5.7. On the surface of the post the no-slip velocity exists, whereas near the edges of the post regions of high velocity gradient prevail. Toward the mid-points of the cavity regions more gradual velocity gradients are observed. Similarly, the liquid velocity tends to be higher over the cavity regions. However, the streamwise velocity magnitudes appear to be considerably higher throughout the cavity region, for this scenario, since the cavity area is so much larger compared to the scenarios presented in Figs. 5.1 and 5.4. This is a direct result of reduced shear stress over a larger region. The average (or apparent) normalized slip velocity at the $y = 0$ plane for this case was 0.043 m/s which is about 2.6 times greater than the slip velocity for the $F_c = 0.85$ and about 1.5 times greater than the $F_c = 0.95$ scenario.

The overall influence of cavity fraction on the local slip velocity was also investigated by considering the line plots of streamwise velocity at $y = 0$ along the post/cavity centerline ($z = 0$ line). These results are illustrated in Fig. # 5.11 for cavity fractions of $F_c = 0.5$, 0.85, 0.95, and 0.9998. Here the velocity at $y = 0$ is plotted versus x/w, where $x/w = 0$ is the start and $x/w = 1$ is the end of a cavity region between two successive posts. For each case, the liquid streamwise velocity increases from zero at the solid surface ($x/w = 0$) to a maximum at the center of the cavity, then it symmetrically returns to zero as the liquid approaches the next solid post surface downstream. It can be seen that the higher cavity fraction scenarios result in much greater velocities at the $y = 0$ plane. These velocities represent streamwise slip velocities and they signify reduction of frictional resistance in the channel. At high cavity fractions the slip velocity reaches its maximum at much smaller x/w than in the low cavity fraction scenarios. Further, at high F_c the slip velocity plateaus at a high value over a significant portion of the cavity region. This is in contrast to the $F_c = 0.5$ case where u/U_{ave} increases until the mid-cavity point.

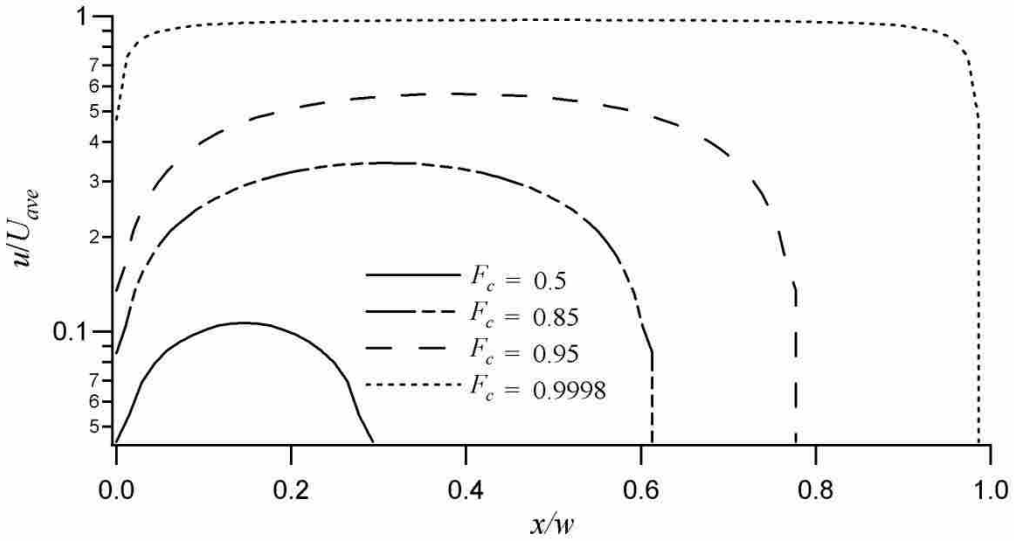

Figure 5.11: Normalized streamwise velocity variation along the cavity/post centerline at $y = 0$ for a pressure-driven flow over a superhydrophobic surface exhibiting square micro-posts at various F_c.

Since the flowing liquid exerts a drag or a shear force on the surface of the channel, the reduction of liquid-solid contact area also affects the amount of shear stress that is applied to the solid surface by the liquid. Figures 5.4 and 5.8 clearly illustrated the variation of shear stress on a micro-post solid surface, and Fig. # 5.5 demonstrated how the shear stress varied along the micro-post at three different locations in the streamwise direction. It was shown that the shear stress was highest along the edges and on the corners, since the velocity gradients were highest at those locations. In light of the above discussion and the observations made in Figs 5.4 and 5.8 it can be concluded that the wall shear stress on micro-posts is higher for surfaces with high cavity fractions. To confirm this, the wall shear stress τ_w normalized by the classical no-slip value τ_{ns} along the cavity/post centerline is plotted in Fig. # 5.12 as a function of x/w at four different cavity fractions. The shear stress variation of each of the four scenarios resembles the profiles presented in Fig. # 5.5. However, Fig. # 5.12 clearly demonstrates the influence the cavity fraction F_c exerts on the post wall shear stress τ_w. It is evident that as F_c increases, the wall shear stress over the post also increases and at high cavity fractions, the increase in the wall shear stress is very significant. As explained previously, this occurs because the surface area of the post is decreased while the fluid inertia moving past the surface remains unchanged. As the flow approaches the post, for each cavity fraction the shear stress increases sharply along the edge of the post and then it decreases almost parabolically to a minimum at the middle of the post and rises again to a peak value at the trailing edge of the post after which it drops sharply again back to a zero value as the flow reaches the cavity region. The rapid jump in each graph is due to high velocity gradients present along the edges. For each scenario the sharp increase in the wall shear stress appears to be higher along the trailing edge than the leading edge of the post. That could be because the flow slows down over the post surface due to friction and loses some of its

momentum as it approaches the trailing edge of the post. The percent increase of τ_w above the no-slip value τ_{ns} at the middle of the post for the cavity fractions shown on the graph were 200, 300, 500, and 5000 for cavity fractions F_c = 0.5, 0.85, 0.95, and 0.9998, respectively.

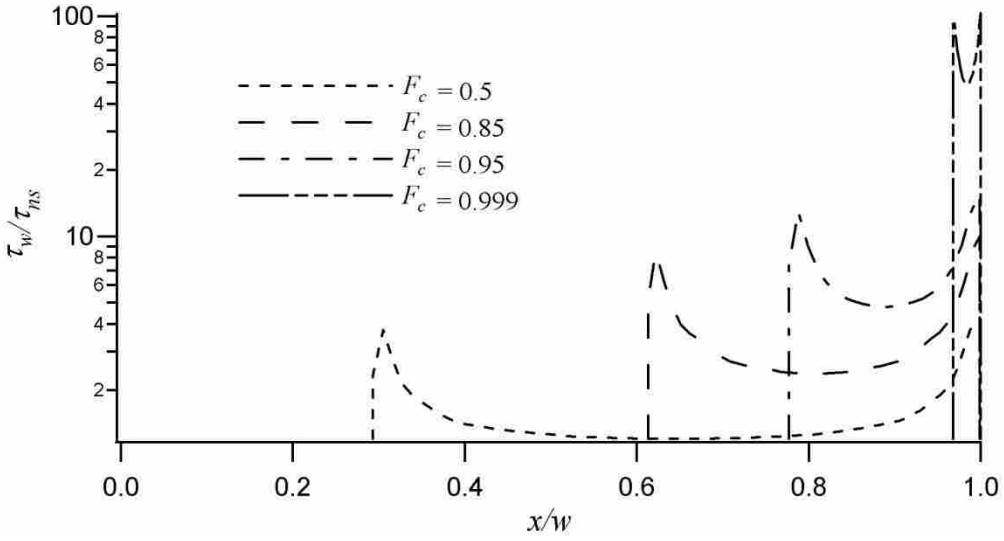

Figure 5.12: Normalized shear stress variation along the cavity/post centerline at y = 0 for a pressure-driven flow over a superhydrophobic surface exhibiting square micro-posts at various F_c , Re = 1, and W_m = 0.1.

Hence, it is clear that the increase in the wall shear stress is non-linear with respect to the cavity fraction and it becomes extremely significant at high values of F_c.

Recall that the friction factor Reynolds number product *fRe* represents the aggregate frictional resistance of a surface, averaging the high shear regions above a post with the zero shear above the cavities. In this regard it is a very useful parameter to use in overall characterization of any superhydrophobic surface. Figure 5.13 presents *fRe* as a function of cavity fraction F_c for square posts, parallel ribs, and transverse rib configurations. All of the data in this figure correspond to Re = 1 and W_m = 0.1. The present post results are plotted along with data from Davies *et al*. [14] for the transverse rib case, and data from Jeffs [27] for the parallel

rib scenario. Both Davies and Jeffs obtained their data numerically using FLUENT. As noted in Ch. 3, Woolford *et al*. [17] later developed correlations (Eqs. 3.16 and 3.17) for both of the scenarios. Perhaps, for future studies, the same process could be followed to develop correlations for post-type surfaces by using the data obtained from the present simulations. In Fig. # 5.13, the data shows that as cavity fraction increases, the *fRe* product for all three surface patterns decreases. Although a direct comparison between posts and ribs cannot be made due to the three dimensionality of the flow for the post case, the general trend (provided all other conditions are the same) can be compared. In general, as F_c decreases, the difference between the three different patterns also diminishes. For instance, at $F_c = 0.5$ there is not a significant difference in *fRe* between the three geometries.

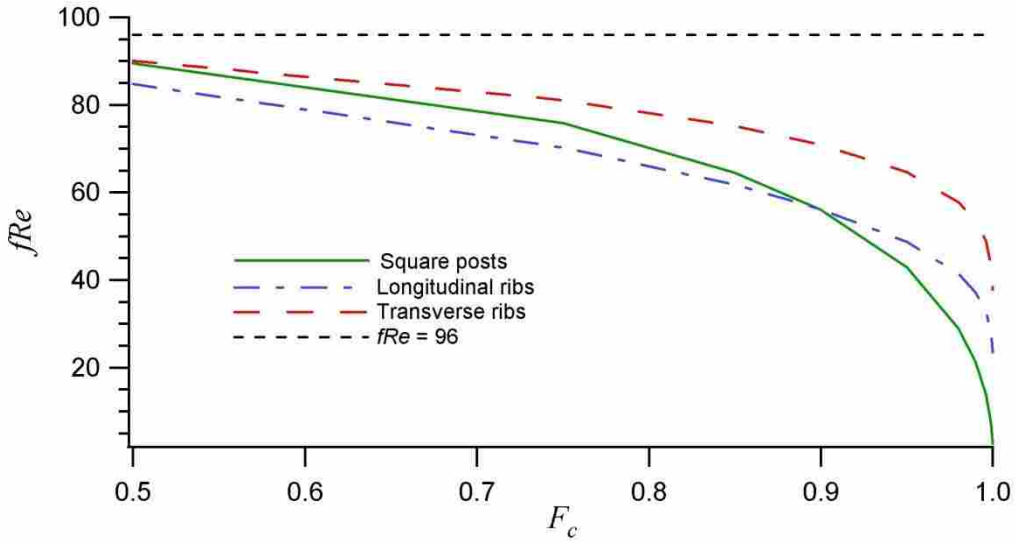

Figure 5.13 *fRe* as a function of F_c for micro-channels with square posts and ribs oriented longitudinal and transverse to the flow direction at *Re* = 1 and W_m = 0.1.

In fact, there is less than 1% difference between the post and the transverse results at this cavity faction value. For small values of F_c all three cases approach the classical channel flow value of 96. In the range of $0.5 \leq F_c \leq 0.88$ the post-type surfaces yield *fRe* values somewhere

between the parallel rib and the transverse rib scenarios. This phenomenon was somewhat discussed earlier in the chapter with Figs. 5.1 and 5.2. Intuitively, it makes sense that geometries with transverse edges and surfaces produce greater velocity gradients and a more significant amount of resistance to flow. As F_c approaches 0.88 the post geometry yields results similar to the parallel rib cases and the gap in *fRe* values widens from the values of Davies *et al*. [14] obtained for transverse ribs. The most interesting phenomenon illustrated in this figure occurs for $F_c \geq 0.88$. Here, it is clear that at high cavity fractions micro-posts far surpass the rib geometries in terms of yielding reductions in *fRe*. As $F_c \rightarrow 1$the data shows that *fRe* drops rapidly for all three configurations, however, the decrease is most pronounced for the post patterned surfaces. At the highest value of F_c explored, F_c = 0.9998, the obtained *fRe* result for square posts was 2.7. In contrast the values for longitudinal and transverse ribs were 23.5 and 37.3, respectively. While the reduction from 96 for the longitudinal and transverse scenario is 76% and 61%, respectively, the reduction for the post geometry is 97.2%. The reason for such reductions in frictional resistance is the decrease in the average wall shear stress $\overline{\tau_w}$. Ybert *et al*. [23] developed scaling laws to predict *fRe* for posts and ribs in limiting case scenarios and their results showed the same patterns.

It is also helpful to look at this effect from a different perspective. The ratio of W_c and W can be classified as cavity width ratio R_c which is different from cavity fraction F_c defined earlier. Then the solid width ratio R_s would be equal to 1-R_c. The reason this is useful is that R_s represents the ratio of post size to total post/cavity width and it is the actual dimensional feature that governs the size posts or ribs that can be fabricated on a surface. Also, since ribs are two-dimensional features and posts represent three-dimensional geometries, the ratio R_c applies to

both posts and ribs for a given size of each. This way, R_c may be a better variable to use for comparison purposes. It is also important to emphasize and to distinguish between the solid width ratio R_s and the solid fraction F_s which was described in Ch. 1. Fig. # 5.14 shows *fRe* as a function of R_s on a logarithmic scale for $Re = 1$ and $W_m = 0.1$.

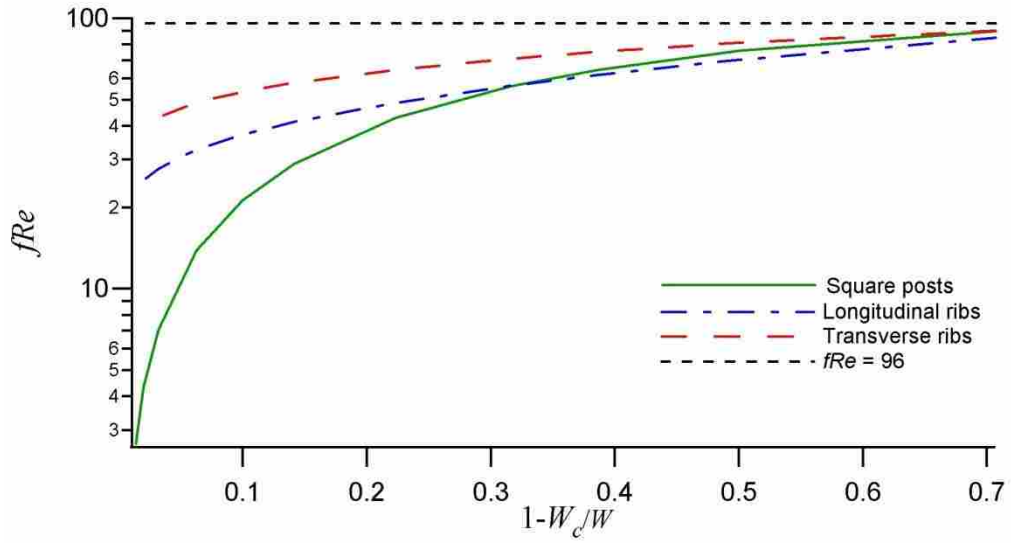

Figure 5.14: *fRe* as a function of solid fraction at $Re = 1$ and $W_m = 0.1$ for superhydrophobic surfaces with; square micro-posts, longitudinal ribs [27] and transverse ribs [14].

For all three surface geometries, as the solid ratio increases *fRe* clearly approaches the classical channel flow value of 96. As the solid ratio decreases ($R_s \rightarrow 0$), the difference between the *fRe* values for the posts and rib configuration is illustrated in a more pronounced manner.

The apparent slip length is another important parameter related to micro-channel liquid flow with superhydrophobic walls. Since *fRe* is related to both the apparent slip length and relative module width, it is useful to observe the effect of cavity fraction on these parameters graphically. Using the acquired numerical results the apparent slip length λ/W was calculated (Eq. 3.15) and plotted as a function cavity fraction as shown in Fig. # 5.15.

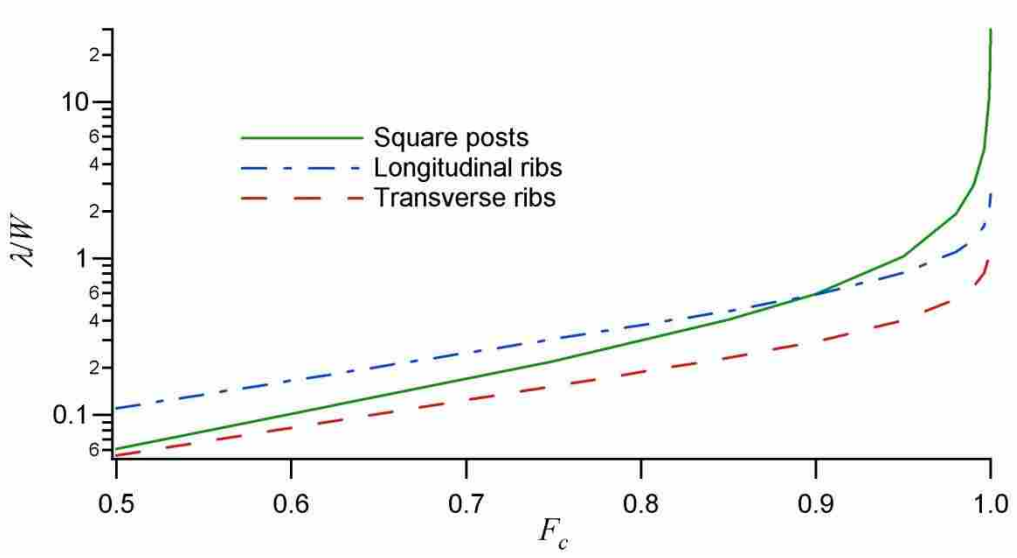

Figure 5.15: Apparent slip length λ/W as a function of F_c for a pressure-driven liquid laminar flow at Re = 1 and W_m = 0.1 over a superhydrophobic surface exhibiting micro-posts.

The data of Fig. # 5.15 shows that as F_c increases, the apparent slip length also increases, and the increase tends to be very significant as $F_c \rightarrow 1$, which is the ideal case. This is due to the decreased amount of liquid-solid contact area. In the ideal situation where there would be no solid surface and the liquid would flow over a layer of vapor. Similar behavior has been documented in the literature by Ybert *et al*. [23], Woolford *et al*. [17], Maynes *et al*. [15], and Davies *et al*. [14]. Ybert *et al*. obtained a scaling law with which they arrived at the same conclusion. Although the correlations given in Eq. 3.16 and 3.17 were developed by Woolford *et al*. [17] for micro-ribs, they verify that $\lambda/W \rightarrow \infty$ as $F_c \rightarrow 1$ which is similar to the results shown in Fig. # 5.16 for micro-posts. However, the magnitude of λ/W is much greater for the post scenario, being 2.2 times greater than the longitudinal rib case at F_c = 0.99.

In Chapter 3 it was shown that there exists a direct relationship between the apparent slip velocity and apparent slip length (Eq. 3.6). The results obtained numerically for the pressure-driven flow scenarios with micro-post patterned walls, presented in Fig. # 5.16, confirm this

relationship. This figure presents the normalized apparent slip velocity variation as a function of F_c in the creeping flow regime, Re = 1 for W_m = 0.1. In both Figs. 5.15 and 5.16 the slip length and slip velocity increase with F_c and the change for both is very significant at large values of cavity fraction.

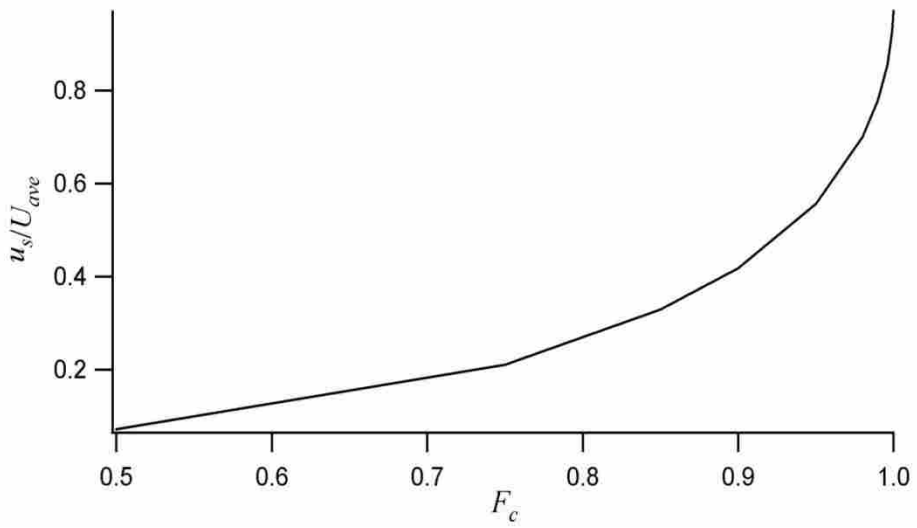

Figure 5.16: Normalized apparent slip velocity at y = 0 for a pressure-driven liquid laminar flow at Re = 1 and W_m = 0.1 over a superhydrophobic surface exhibiting square micro-posts.

Similar to the apparent slip length variation with increasing F_c, as illustrated in Fig. # 5.15, the apparent slip velocity also increases as F_c increases. The increase appears to be more significant at high values of cavity fractions. The overall apparent slip velocity, which is an area-weighted average quantity at y = 0, represents an effective increase in the mass flow rate of liquid through the channel. This phenomenon is extremely desirable in situations such as liquid flow through micro- or nano-channels.

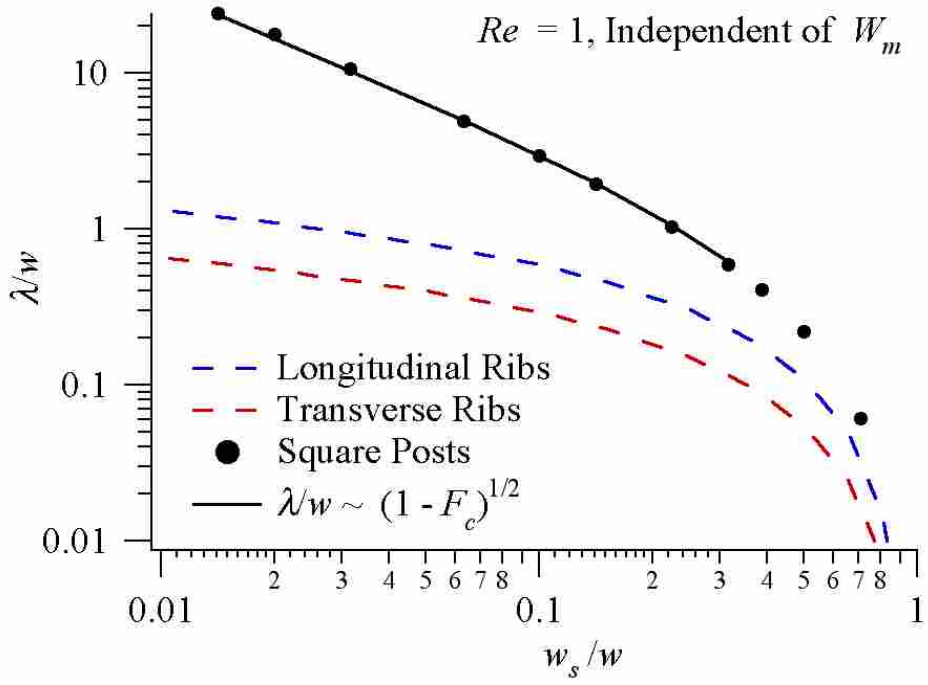

Figure 5.17: Apparent slip length λ/W as a function of W_s/W for a pressure-driven liquid laminar flow at Re = 1 and W_m = 0.1 over a superhydrophobic surface exhibiting micro-posts compared with longitudinal [15] and transverse [14] ribs and the results obtained by Ybert *et al.* [23].

Variation of the slip length with respect to the solid width ratio for posts, longitudinal ribs [27], transverse ribs [14], and scaling laws for posts [23] are shown in Fig. # 5.17. All results indicate that slip length reduces significantly with increasing solid width ratio. Our numerical simulation results are in close agreement with Ybert's scaling law results.

5.1.2 Influence of Relative Module Width W_m at Re = 1

The relative module width, W_m is defined as the ratio of the total module width to the hydraulic diameter (Eq. 1.7). For the same module width and cavity fraction, higher value of W_m implies a shorter channel, and conversely a low value of W_m indicates a taller channel height. As a result, by keeping the width constant and varying W_m one can examine the effect of channel height on the overall frictional resistance. At Re = 1 and the range of $0.01 \leq W_m \leq 1.5$ three

different cavity fractions were considered 0.75, 0.95, and 0.999. The *fRe* results from this study are illustrated in Fig. # 5.18.

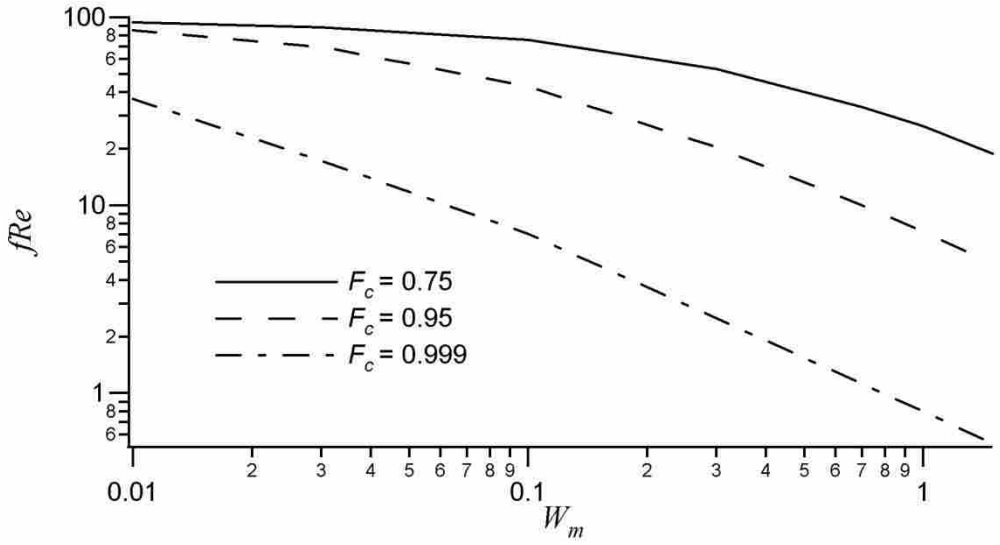

Figure 5.18: Dependence of *fRe* on W_m for a superhydrophobic surface exhibiting square micro-posts in a pressure-driven flow situation at *Re* = 1 for F_c = 0.75, 0.95, and 0.999.

The general trend in the data of Fig. # 5.17 is similar to results published in the literature for micro-ribs and those obtained by scaling laws for micro-posts [14, 15, 16, 23]. As W_m increases, the *fRe* product decreases, with the most significant variation occurring for $W_m \leq 0.3$. Figure 5.13 showed that *fRe* decreased as cavity fraction increased for $W_m = 0.1$. In Fig. # 5.18 similar behavior is observed for other values of W_m. In all scenarios, as $W_m \rightarrow 0$ the *fRe* product approaches the classical value of 96. At a specific value of W_m, the gap between *fRe* results for the different scenarios explored, tends to decrease as F_c increases. For instance, at $W_m = 1$ the difference in *fRe* results for F_c = 0.95 and 0.999 is about 8%, whereas the difference in *fRe* for the F_c = 0.75 and 0.999 is more significant and approximately equal to 20%. This observation underlines the fact that the reduction in liquid-solid contact area does indeed reduce frictional resistance. An interesting observation from the figure is that as $W_m \rightarrow 0$, the reduction in

frictional resistance diminishes. The implication is that for very tall channels, even with the large $F_{c,}$ the top and bottom surfaces of the channel may be too far apart to have a significant effect on the overall frictional resistance.

The influence of W_m near the surface was also determined for the post patterned superhydrophobic surface and the results are illustrated in Fig. # 5.19. It can be seen that when *Re* is held constant, the apparent slip length λ/W also remains constant with respect to relative module width W_m for all three cavity fractions F_c = 0.75, 0.95, and 0.999.

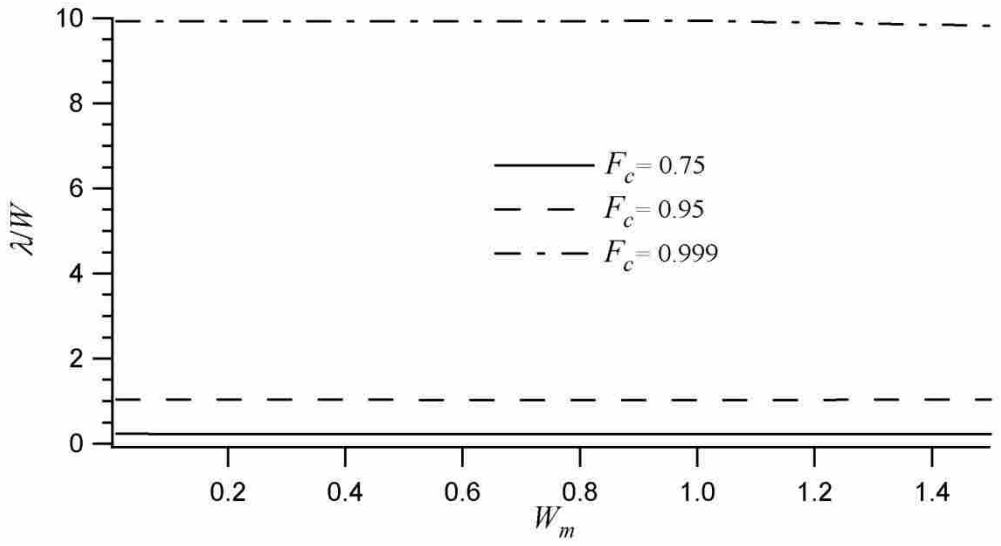

Figure 5.19: Dependence of λ/W on W_m for a superhydrophobic surface exhibiting square micro-posts in a pressure-driven flow situation at *Re* = 1 for F_c = 0.75, 0.95, and 0.999.

Previously published results for ribs [1, 10, 14, 15] have also shown that regardless of W_m the apparent slip length λ/W is mainly dependent on the cavity fraction F_c. According to Fig. # 5.19, the results from this study which had never been proved prior to this study, show similar relationship for post-patterned superhydrophobic surfaces. Such an important contribution has been verified by the following relationship for longitudinal ribs [10]

$$\frac{\lambda}{W} = \frac{1}{\pi}\ln\left(\sec\left(\frac{\pi}{2}F_c\right)\right) \tag{5.1}$$

Although Lauga and Stone [10] developed an analytical expression for transverse ribs that varied from Eq. 5.1 by a factor of 0.5, more recent results obtained from literature [1, 14, 15] have been somewhat different for transverse ribs. One can conclude that the apparent slip length is independent of the channel size and is only a function of the cavity fraction for longitudinal ribs, but is dependent on the cavity fraction and the Reynolds number (within a limited range) for transverse ribs [1, 2] and similarly for posts, as will be discussed in the next section.

5.1.3 Influence of Reynolds Number *Re* on *fRe*

In order to analyze the effect of the Reynolds number on the overall frictional resistance reduction, simulations were performed over the flow regimes $1 \leq Re \leq 2500$. Figure 5.20 shows a streamwise velocity contour at $y = 0$ and Re =1000 for the same F_c and $\boldsymbol{W}_m$ as shown in Fig. # 5.7. At this Reynolds number, Fig. # 5.20 illustrates similar overall pattern in the streamwise velocity contour to the one presented in Fig. # 5.7, but with a few important differences. The most important difference relates to the velocity contour between two consecutive posts. In Fig. # 5.7 the velocity behavior is symmetric about the two consecutive posts regardless of the flow direction. However, for the high *Re* case this symmetry no longer exists. This is illustrated in Fig. # 5.20 by the relative size of the low-velocity region at the front and behind the post. At high *Re*, the low-velocity region persists further into the cavity region than for the low *Re*, symmetric, case. As before, the maximum velocity occurs in the longitudinal spacing between the posts.

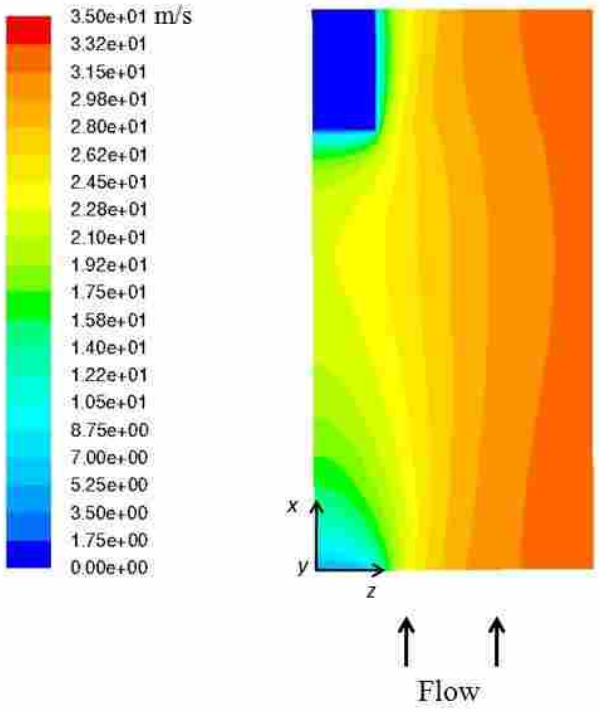

Figure 5.20: A typical streamwise velocity contour (m/s) for a pressure-driven flow over a superhydrophobic surface, $y = 0$, exhibiting square micro-posts with $Re = 1000$, $W_m = 0.1$, $F_c = 0.95$.

Figure 5.21 provides a graph of *fRe* as a function of *Re* and the data confirms the existence of a *Re* dependency for $Re \geq 40$.

According to Jeffs [27] frictional resistance *fRe* for micro-ribs oriented longitudinal to the flow direction is independent of *Re*. However, Davies *et al*. [14] showed in their numerical analysis for transverse ribs that a significant dependence on Reynolds number exists in the $Re \geq 40$ range.

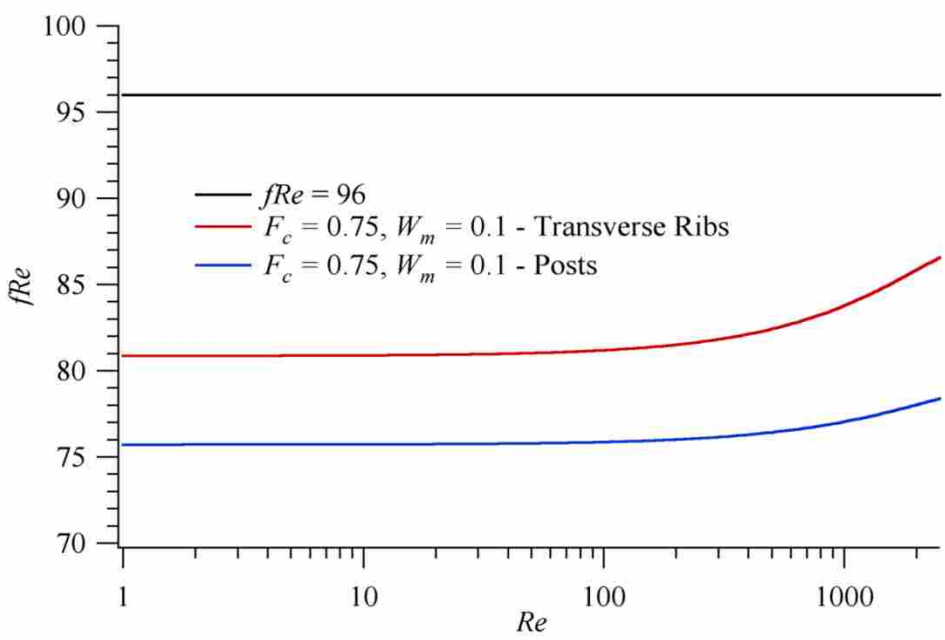

Figure 5.21: Dependence of *fRe* on Reynolds number in non-creeping flow regime, *Re* ≥ 1, for liquid flow over superhydrophobic surfaces with micro-post and micro-rib patterning [14].

The data of Fig. # 5.21 corresponds to $F_c = 0.75$ and $W_m = 0.1$, and the present post results are compared to data obtained by Davies *et al*. [14] for transverse ribs. For all values of *Re*, post features yield smaller values for *fRe* than transverse ribs at this F_c. This is consistent with the previous discussion of the creeping flow regime. Up to $Re \approx 40$ the frictional resistance for both surface geometries is independent of the Reynolds number. Throughout this region the post scenario yields about 6.2% more reduction in *fRe* compared to transverse ribs. However, at $Re \geq 40$ both posts and transverse ribs show increased dependence on *Re*. As *Re* increases further, the *fRe* values for both surface geometries increase toward the classical laminar flow value of 96 for parallel plates. It should be noted that the dependence of *fRe* is less symmetric for the post features than for the transverse rib scenarios, as observed in Fig. # 5.20. For the transverse rib *fRe* increases by 5 between $Re = 40$ and $Re = 2000$. Conversely, the increase in *fRe* for the post scenario is 2 over this same *Re* range.

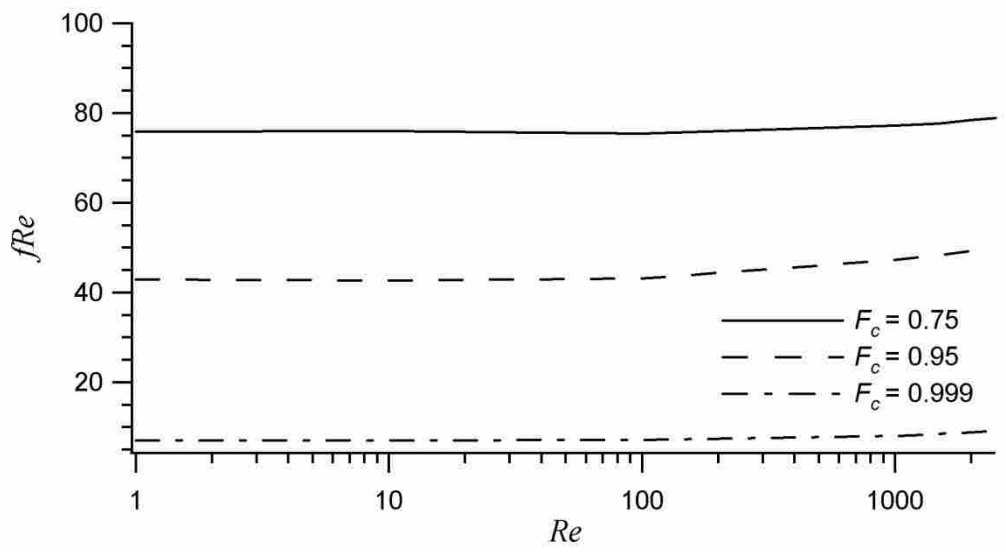

Figure 5.22: Dependence of *fRe* on Reynolds number in non-creeping flow regime, *Re* ≥ 1, for liquid flow over superhydrophobic surfaces with micro-post patterning at various *Fc*.

Dependence on *Re* by *fRe* was examined at various cavity fractions, and at all cavity fractions explored, the relationship between *fRe* and *Re* was observed. Fig. # 5.22 shows *fRe* as a function of *Re* for post patterned superhydrophobic surfaces at F_c = 0.75, 0.95 and 0.999. It can be seen that the *fRe* behavior is similar for all three F_c. Similar to transverse ribs, *fRe* is independent of the Reynolds number at $Re \leq 40$ and gradually increase non-linearly with increasing *Re*. This increase appears to be modestly more pronounced at low cavity fractions, although the difference between the various F_c values is small. Such results are significant, because they suggest that for $Re \geq 40$ the frictional resistance actually begins to increase. In other words, as *Re* reaches the upper limit for laminar channel flow and in the transitional flow regime the frictional resistance increases with increasing *Re*.

The influence of *Re* on *fRe* at various relative module widths W_m was also investigated. Fig. # 5.23 shows how *fRe* varies with respect to *Re* for liquid flow over superhydrophobic surfaces with a post configuration when F_c = 0.75, and at W_m = 0.1 and 1. While both the W_m =

0.1 and $W_m = 1$ data portray a similar overall behavior, a significant difference can be noticed. At $W_m = 1$ the *fRe* is independent of *Re* only for $Re \leq 4$, whereas, at $W_m = 0.1$ this independence is observed for $Re \leq 40$. The comparison of the two scenarios indicates an order-of-magnitude difference between the two Reynolds numbers and the two relative module widths. As W_m was increased by a factor of ten, the influence of the *Re* began to occur of whose Reynolds number influence, and thus fluid inertia exercises influence. This is unexpected since relative module widths of 0.1 and 1 are different by a factor of ten. This behavior is also consistent with that observed by Davies *et al*. [14] for transverse ribs. One implication of this is that a better Reynolds number to evaluate is the Reynolds number based on the width of a cavity and rib module $Re_w = \bar{U}W/\nu = (Re)W_m$. Using this definition, the departure from a constant *fRe* value occurs at $Re_w \approx 10$ for both the $W_m = 1$ and 0.1 cases. This makes excellent physical sense, since it is the local size of the rib features that give rise to the non-symmetric behavior illustrated in Fig. # 5.20.

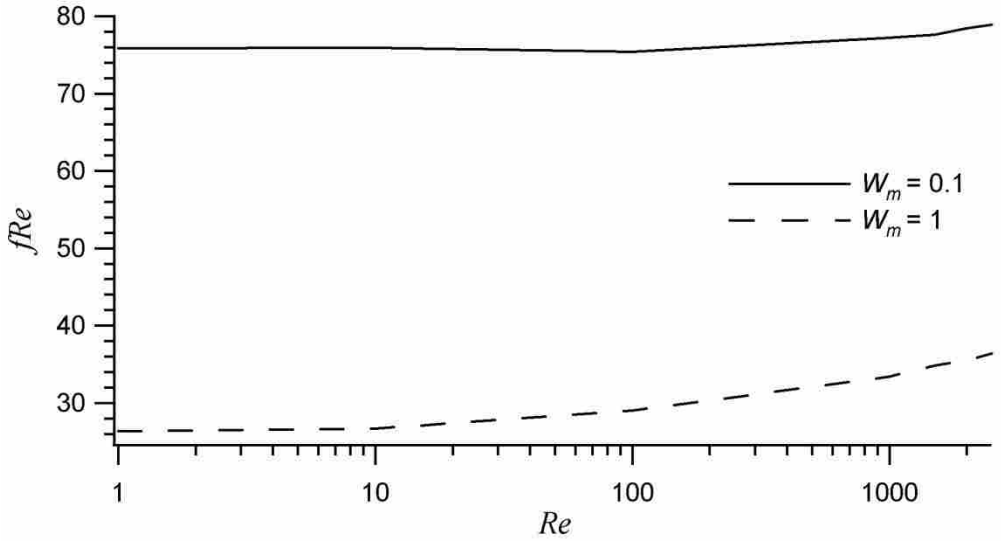

Figure 5.23: Dependence of *fRe* on Reynolds number in non-creeping flow regime, $Re \geq 1$, for liquid flow over superhydrophobic surfaces with micro-post patterning for $F_c = 0.75$ and $W_m = 0.1$ and 1.

The results of phase (1) indicate that for superhydrophobic surfaces the frictional resistance reduction is strongly dependent on F_c and W_m in the creeping flow regime. This reduction becomes increasingly more significant at large cavity fractions and also at large relative module widths. The effect of superhydrophobicity is more pronounced as the channel hydraulic diameter decreases. Surfaces exhibiting square micro-posts reduce frictional resistance more than transvers ribs, but less than longitudinal ribs at $0.0 \leq F_c \leq 0.88$. However, over the range of $0.88 \leq F_c \leq 0.9998$ surfaces with micro-posts were significantly more effective in reducing frictional rasistance than those with transverse and longitudinal ribs. While frictinal risistance is independent of the Reynolds number for longitudinal ribs, it becomes increasingly dependent on the Reynolds number at $Re \geq 40$ for surfaces with posts and transverse ribs. For such surfaces, further increase in Re has an adverse effect on the frictional resistance reduction.

5.2 Couette Flow with Square Micro-Posts

Attention will now be given to the scenario of a wall driven, or Couette, flow on the dynamics. A thorough review of the literature revealed no previous studies explaining the effects of other driving forces on frictional resistance reduction in micro-channels with superhydrophobic walls having square post configurations. This issue has not been addressed previously in a complete and comprehensive manner. A wide variety of questions relevant to this as mentioned in the Objective section remain unanswered. In order to provide insight and useful answers to those previously discussed questions, similar simulations were performed for shear-driven (Couette) flow. Analyzing the influence of F_c and W_m in the creeping flow regime where the Couette flow Reynolds number $Re_c = 1$ was the main objective in the Couette flow scenarios. Because in Couette flow, the velocity profile within the channel is linear as opposed

to pressure-driven cases where the velocity profile is parabolic, it is logical that some noticeable differences should be observed, even if all other conditions are maintained the same. For the Couette flow scenarios, the average velocity used for pressure-driven cases was employed as the velocity of the moving top wall and the Reynolds number was based on the plate velocity $Re_c = (U_p D_h)/v$. The bottom wall was considered to be superhydrophobic. The influences of important parameters such as the cavity fraction, in the range of 0.0-0.9998, and the relative module width, from 0.01 to 1.5, on frictional resistance reduction in the creeping flow regime were explored. Certain formulas for Couette flow scenarios were included in Ch. 3 to show the relationship between various parameters as they appear in the following discussions. The following sections address the influence of cavity fraction and relative module width on fRe, u_s, and λ/W.

A typical streamwise velocity contour at the superhydrophobic wall surface ($y = 0$) of the channel for a Couette flow case at $Re_c = 1$, $W_m = 0.1$, and $F_c = 0.85$ is presented in Fig. # 5.23. The general pattern appears to be similar to the pressure-driven situation shown in Fig. # 5.1. However, one important difference that can be observed is that the velocity magnitudes are smaller than in the pressure-driven case. The normalized area-weighted average velocity at $y = 0$ (apparent slip velocity) for this case was about $u_s/U_p = 0.141$. This is approximately 13.9% less than the pressure-driven flow case at the same F_c and W_m, because the streamwise velocity gradients in the direction normal to the wall are different for these two cases.

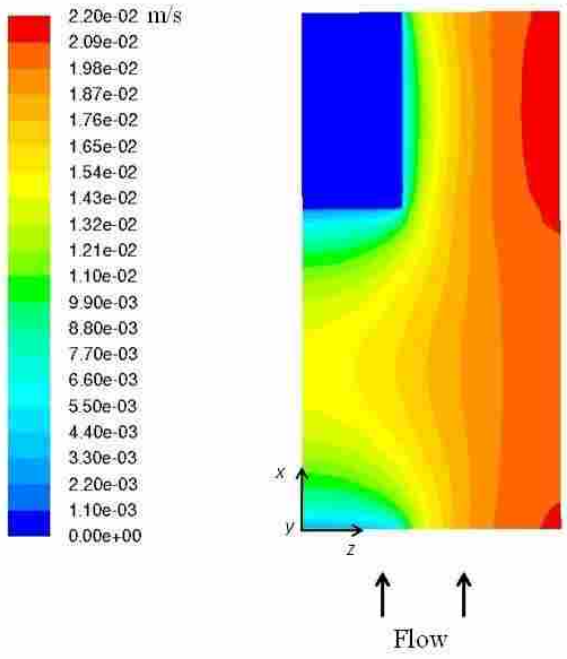

Figure 5.24: A typical streamwise velocity contour for a Couette flow over a superhydrophobic surface, $y = 0$, exhibiting square micro-posts at $Re_c = 1$, $F_c = 0.85$, and $W_m = 0.1$.

Figure 5.25 provides shear stress contours at a typical post surface for the $Re_c = 1$, $W_m = 0.1$, and $F_c = 0.85$ scenario. The overall pattern is also similar to what was observed in Fig. # 5.4 for the pressure-driven flow situation. The high shear stress regions again occur along the edges and especially in the corners. The wall shear stress values also tend to be smaller in this case than in the pressure-driven scenario. Again, this is due to the fact that the driving plate velocity for the Couette flow scenario is equal to the average (not maximum) velocity for the pressure-driven flow scenarios.

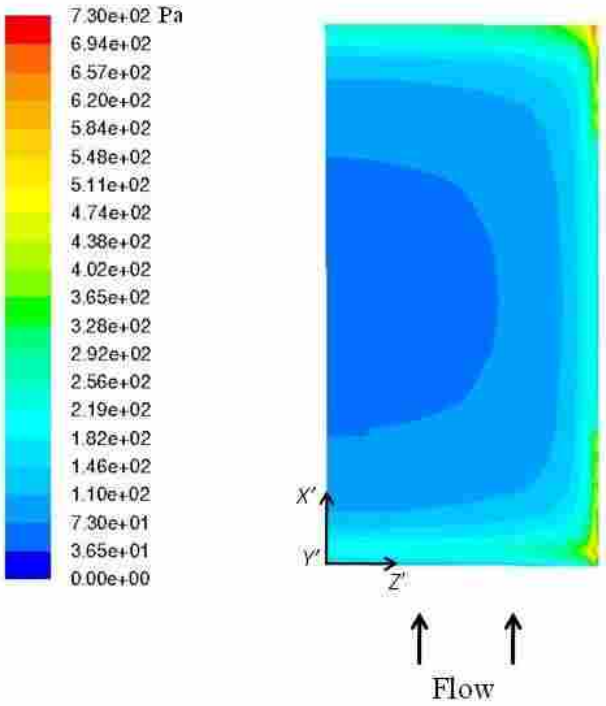

Figure 5.25: Area weighted average shear stress contour for a Couette flow over a typical micro-post surface at y = 0 and Re_c = 1, F_c = 0.85, and W_m = 0.1.

In future work, simulations at other Reynolds numbers could be performed with Couette flow to investigate influence of Re_c over the laminar flow range. Because the effect of the driving force on the overall surface friction was one of the primary objectives, the shear stress at the surface is an important parameter to examine. Similar to the pressure-driven case, variation of the wall shear stress at the surface is related to the amount of slip at the surface. Figure 5.26 presents, for the F_c = 0.95, W_m = 0.1 and Re_c = 1 case, the normalized shear stress on the surface of a post in the streamwise direction at three different lateral locations. The three positions correspond to those shown in Fig. # 5.2, and the result is similar to the results of Fig. # 5.5. The

shear stress for all scenarios peaks at the leading and trailing edges of the post. At each lateral location (z = 0.0, 0.19, and 0.38), the wall shear stress decreases from a high value at the leading edge to a minimum at the center of the post and increases back to a maximum at the trailing edge of the post. The normalized wall shear stress at z = 0.38 is much greater than τ_w/τ_{ns} at z = 0.0 and 0.19, because the wall-normal velocity gradients are greater along the post edge at z = 0.38 than at the other two locations. At z = 0.38 the graph of τ_w/τ_{ns} demonstrates a shallower dip than at z = 0.0 and 0.19, since the wall-normal velocity gradients do not decrease as much along the post edge as the liquid approaches post midpoint. The dip or the lowest point on the graph of τ_w/τ_{ns} at z = 0.38 is approximately three times greater than the dips at the other two locations.

These observations are consistent with the shear stress contour of Fig. # 5.25. Comparing wall shear stress results of the pressure-driven flow and the Couette flow scenarios shows that for both, the streamwise wall shear stress is greater in magnitude along the edge than along the midpoint of the post. Another observation from comparing these results is that the overall normalized wall shear stress magnitudes are higher in the pressure-driven cases than in the similar Couette flow scenarios. Care should be taken to not compare Fig. # 5.26 directly with Fig. # 5.5, since they belong to surfaces with two different F_c values. However, direct comparison of the numerical results of the wall-shear stress for both scenarios at F_c = 0.85 indicates that there is not a discernable difference in the normalized wall-shear stress near the midsection of the post. This quantity was $\tau_w/\tau_{ns} \approx 2.4$ at the minimum points of the graphs along the z = 0 and 0.19 lines for both scenarios. But, near the edge of the post along the z = 0.38 line the quantity $\tau_w/\tau_{ns} \approx 7.44$ for the Couette flow and about 8 for the pressure-driven flow scenarios, respectively. This difference of approximately 7% in the wall-shear stress implies greater

velocity gradients along the edge of the post for the pressure-driven flow case than the Couette flow case.

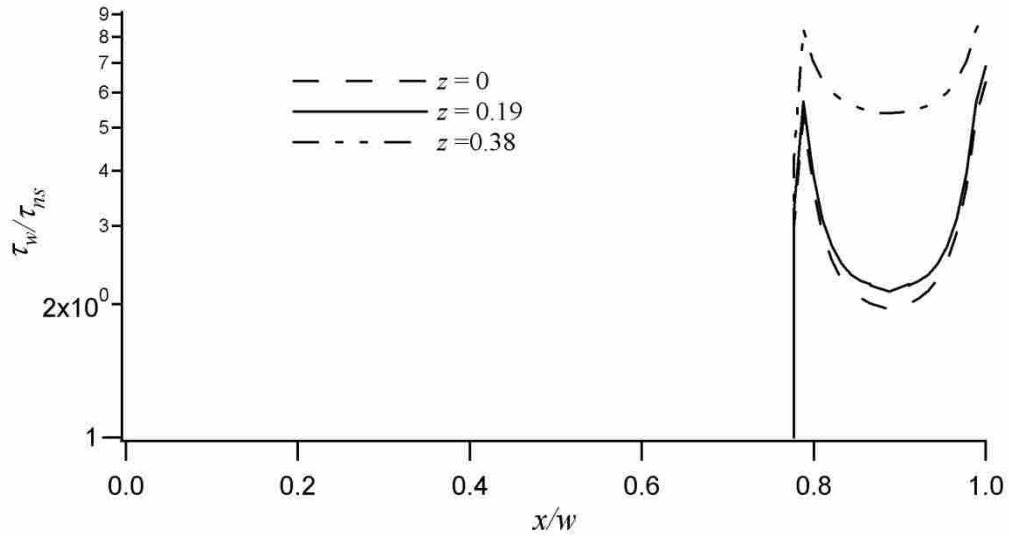

Figure 5.26: Typical normalized streamwise shear stress variations at $y = 0$ and at three different locations on a post for a Couette flow over a superhydrophobic surface exhibiting square micro-posts with $Re_c = 1$, $W_m = 0.1$, $F_c = 0.95$.

As mentioned in the pressure-driven flow section, modification of the shape and geometry of the edges and/or corners of the posts could cause a reduction in the wall shear stress. In future studies different post geometries, such as cylindrical shapes could also be considered and investigated for Couette liquid flows over superhydrophobic surfaces exhibiting post geometry.

At this point, it is appropriate to consider velocity profiles for the Couette flow situation at specific locations shown in Fig. # 5.27 which are normalized velocity profiles at the same four locations as the profiles of Fig. # 5.9. Here the velocity is normalized by the plate velocity and y is normalized by the spacing between plates H. Also shown is the mean profile demonstrated as U_m. As it was mentioned in section 3.2.1, the velocity profile for Couette flow is linear. For a

classical Couette flow where no-slip boundary condition prevails at both surfaces, the average velocity is one half of the plate velocity. However, in section 3.2.2 it was mentioned that for a Couette flow over a superhydrophobic surface, the average flow velocity is greater than half the plate velocity due to apparent slip on the bottom surface.

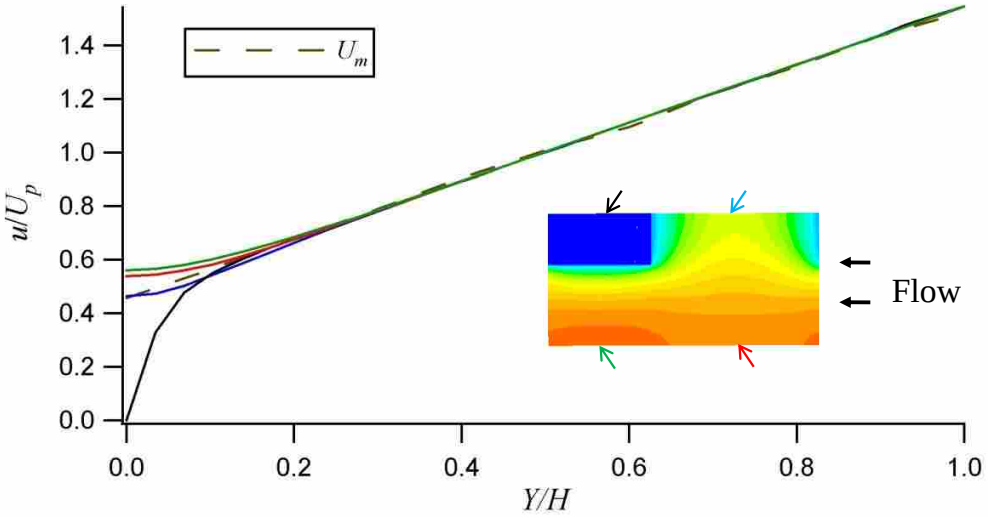

Figure 5.27: Normalized streamwise velocity profiles at four locations within the computational domain for a Couette flow over a superhydrophobic surface with square micro-post geometry for the scenario Re_c = 1, F_c = 0.95, and W_m = 0.1.

As far as the bulk liquid flow is concerned, there are obvious differences between the pressure-driven and the Couette flow, even when all other parameters are the same. The question is whether there are any differences in overall slip at the superhydrophobic surface between the two driving forces. The following few sections are devoted to answering this question which is also one of the objectives of this study. Careful comparison of Figs.5.9 and 5.27 illustrates very similar shape and behavior in the velocity profiles at all four locations, but with different magnitudes. Similar to the pressure-driven flow result, above a certain wall normal position the profiles over all surfaces are essentially the same in magnitude and shape.

For the Couette-flow scenario, profiles begin to deviate from one another at $\frac{2y}{H} \leq 0.3$. This is approximately the same wall-normal location for the pressure-driven case. The fact that the deviation of the velocity profiles for both driving forces occurs at approximately the same vertical distance from the channel surface is indeed an important discovery. Again, the non-zero velocity at $y = 0$ for the mean profile, U_m, is an indication of apparent slip at the surface. The maximum slip velocity again occurs in the cavity region, shown with a green arrow, between the posts. The normalized mean velocity at $y = 0$ (or apparent slip velocity) shown with a dashed line has the value of 0.45. This is 18% less than the apparent slip velocity of 0.55 in the pressure-driven flow scenario at $F_c = 0.95$.

5.2.1 Influence of Cavity Fraction F_c at $W_m = 0.1$ and $Re_c = 1$

In order to determine the effect of cavity fraction on the overall friction reduction for the Couette-flow scenario, the streamwise velocity along the post/cavity centerline at $y = 0$ was obtained and graphed. These results are illustrated in Fig. # 5.28 for cavity fractions of $F_c = 0.5$, 0.85, 0.95, and 0.999. Generally, the results are very similar to the pressure-driven cases discussed in Sec.5.1.1 and presented in Fig. # 5.11. Since the non-zero velocities at the channel wall represent streamwise slip, it can be concluded that similar to the pressure-driven flow results, as the cavity fraction increases the slip velocity tends to increase significantly. The variation in the streamwise slip velocity at each cavity fraction is similar in shape to the corresponding cases in the pressure-driven flow study, although the magnitudes are different due to the average velocity used in normalization.

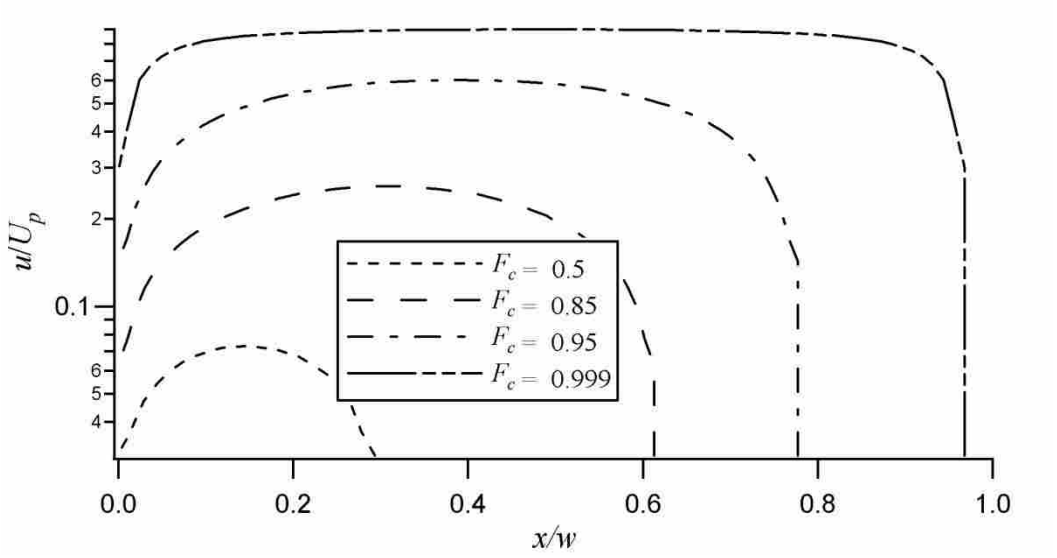

Figure 5.28: Normalized streamwise velocity variation along the cavity/post centerline at y = 0 for a Couette flow over a superhydrophobic surface exhibiting square micro-posts at various F_c , Re_c = 1, and W_m = 0.1.

The consistency of the results was also evaluated by examining the variation in the normalized wall shear stress τ_w/τ_{ns} along the cavity/post centerline at the same cavity fractions. This is shown in Fig. # 5.29. The profiles of Fig. # 5.29 are similar in shape to those presented in Fig. # 5.12 for pressure-driven flow. In Fig. # 5.29, as F_c increases the wall shear stress τ_w over the post also shows a significant increase especially at high values of the cavity fraction near the limiting case $F_c \rightarrow 1$. Comparisons related to the magnitudes of the wall shear stress for the two cases of pressure-driven and Couette flow reveal that in general τ_w/τ_{ns} is lower for the Couette flow scenario, as compared to the pressure-driven flow case. The following figures and related discussions will address this variation.

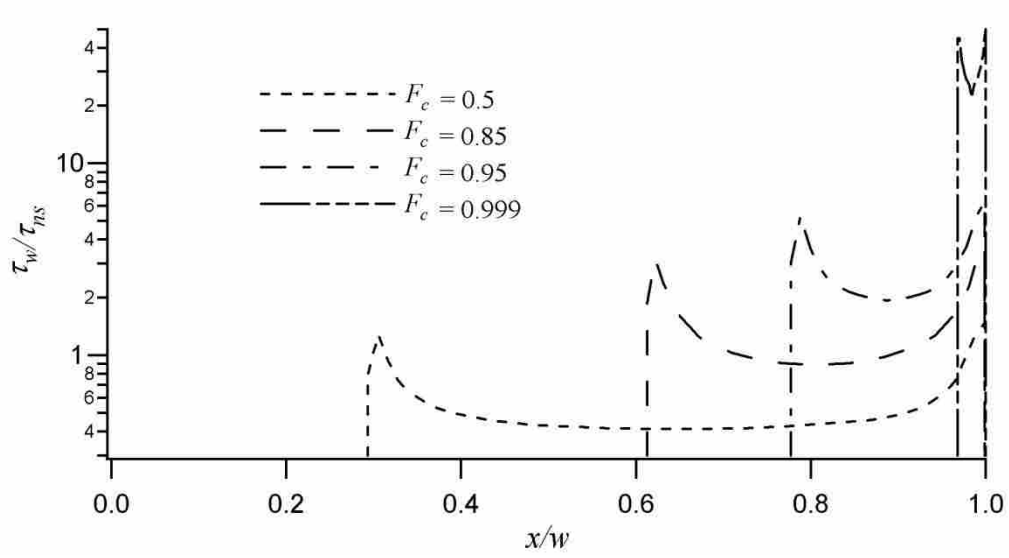

Figure 5.29: Normalized shear stress variation along the cavity/post centerline at $y = 0$ for a Couette flow over a superhydrophobic surface exhibiting square micro-posts at various F_c , $Re_c = 1$, and $W_m = 0.1$.

As was discussed in chapter 3 for classical laminar Couette flow, the *fRe* value is equal to 32. Again, the velocity distribution in the wall-normal direction is linear, varying from zero at the wall to a maximum at the moving wall boundary. In this case, the average streamwise velocity is $\bar{U} = 0.5U_p$, where U_p is the velocity of the moving wall (or plate). However, in calculating *fRe* it is important to remember that for flow over a superhydrophobic surface, there is an apparent slip flow at the stationary wall surface of the channel. Therefore, the mean or average velocity is no longer equal to $0.5U_p$, but it should be calculated by taking into account the slip velocity u_s at the surface, *i.e.* $\bar{U} = 0.5(U_p + u_s)$. Since often an objective in fluid flow over superhydrophobic surfaces is the reduction of frictional resistance, Fig. # 5.30 shows how *fRe* varies with respect to F_c.

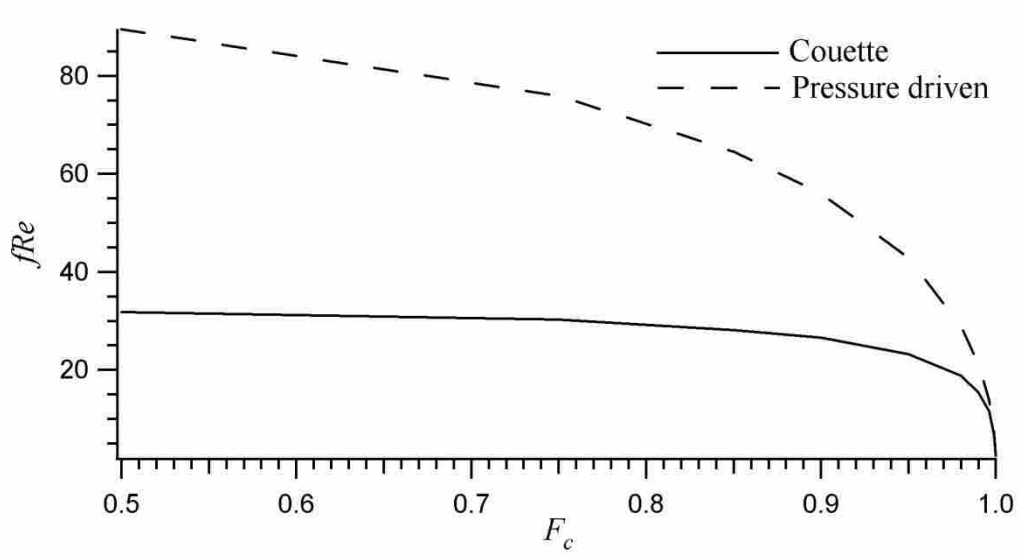

Figure 5.30: *fRe* as a function of F_c for fully developed Couette flow and pressure-driven flow at Re_c = 1 and W_m = 0.1 over a superhydrophobic surface exhibiting square posts.

In this figure, the data for the Couette flow scenario is shown along with data for the similar scenario in the pressure-driven flow case. For both scenarios, Re_c = 1 and W_m = 0.1, Couette flow follows a similar trend as the pressure-driven scenario. At small values of F_c they both approach their corresponding values for the classical no-slip channel flow, (96 and 32) emphasizing that at low cavity fractions the effect of superhydrophobic surfaces vanishes. For both flow mechanisms, at high values of F_c, the *fRe* product decreases markedly as the frictional resistance decreases. In the F_c range from 0.5 – 0.9 the variation in *fRe* is much greater for the pressure-driven flow scenario. At F_c = 0.9, *fRe* has dropped by 36% for the pressure-driven case, while dropping 12.5% for the Couette flow case. As $F_c \rightarrow 1$ for both scenarios there is a substantial decrease in *fRe*. One implication of these results is that the influence of superhydrophobicity at lower cavity fractions will be only minimal. Conversely, at large F_c the impact for both flow scenarios is significant. That is because at low F_c (approximately less than

0.75) the reduction of liquid/solid contact area does not reduce the wall shear stress significantly to have a substantial effect on frictional resistance reduction.

In Ch. 3 it was shown that mathematical expressions for determining the apparent slip length and slip velocity for the pressure-driven flow and the Couette flow are different. Once the *fRe* product is determined numerically, Eqs.3.14 and 3.25 can be used to calculate the apparent slip length for the two flow conditions, respectively. The difference between these two equations is largely due to the different velocity profiles involved in the two cases. Figure 5.31 provides the normalized apparent slip length λ/W with respect to solid fraction F_s for both the pressure-driven and the Couette flow scenarios at $Re = 1$ and $W_m = 0.1$.

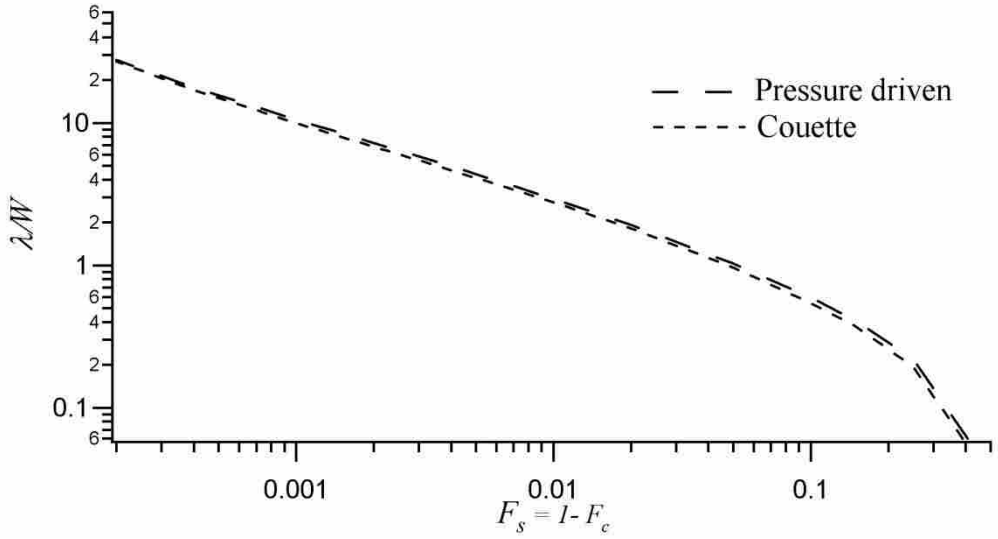

Figure 5.31: Normalized apparent slip length λ/W as a function of solid fraction F_s for both Couette flow and pressure-driven flow over a superhydrophobic surface with micro-posts at Re_c = 1and W_m = 0.1.

For both flow types there is an inverse relationship between the apparent slip length and the solid fraction. When the solid fraction approaches its hypothetical lower limit $F_s \rightarrow 0$, the apparent slip lengths for both types of flow increase dramatically as expected. In the absence of

any solid material on the channel surface, the slip length should approach infinity. Conversely, as the solid fraction increases the apparent slip length decreases. This result is also logical and it confirms the accuracy of the obtained results since as the solid fraction approaches its upper limit $F_s \rightarrow 1$ the apparent slip length for both cases should vanish to satisfy the no-slip boundary condition on the surface. It is important to notice that there is not a discernable difference in the apparent slip length between the Couette flow and the pressure-driven flow cases in the creeping-flow regime. This is an important finding because it had not been documented prior to this study and it implies that the slip length is totally independent of the driving force and it is only related to the surface geometry and the cavity fraction of the surface.

To further compare the differences between the flow types, apparent slip velocities were obtained. These are normalized in both cases by using the area-weighted average streamwise velocity and shown with respect to solid fraction F_s for both flow scenarios in Fig. # 5.32 for Re = 1and W_m = 0.1. Since there is a direct relationship between the apparent slip length and the slip velocity through Eq. 3.3, the slip velocity should vary with respect to F_s in a manner similar to the slip length. Figure 5.32 shows that the general trend is indeed similar. The data show that as $F_s \rightarrow 0$ the apparent slip velocity approaches the average velocity, and as $F_s \rightarrow 1$, u_s/U_{ave} reduces to zero for both cases. Over the entire range of F_s, the apparent slip velocity in the pressure-driven flow case is greater than for the Couette-flow scenarios.

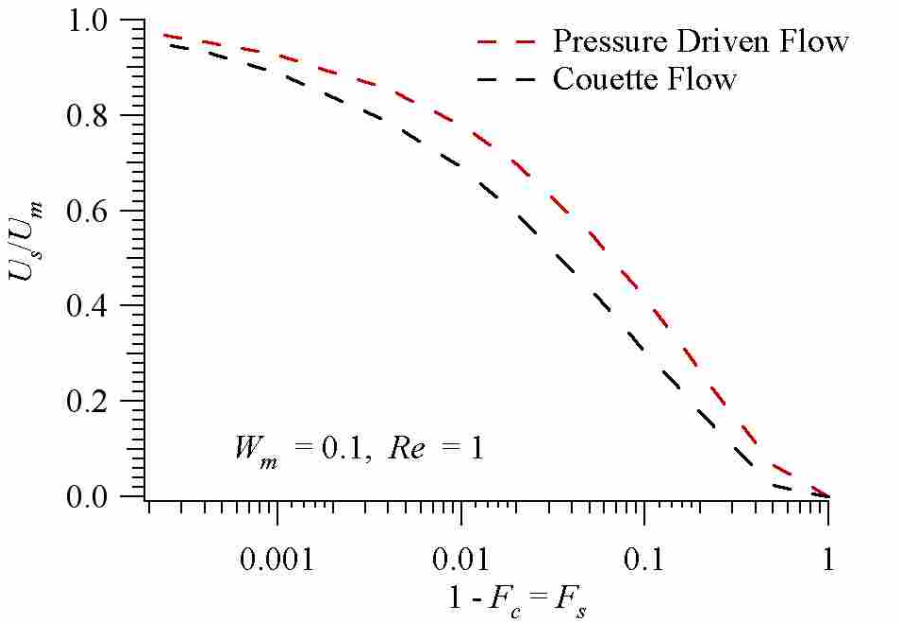

Figure 5.32: Normalized apparent streamwise slip velocity as a function of solid fraction F_s for Couette flow and the pressure-driven flow over a superhydrophobic surface with micro-posts at $Re_c = 1$ and $W_m = 0.1$.

5.2.2 Influence of Relative Module Width W_m at $Re_c = 1$

For pressure-driven flow it was shown how the relative module width affects the overall frictional resistance reduction in liquid flow over superhydrophobic surfaces. Since the relative module width W_m depends on the post/cavity total width W and the hydraulic diameter D_h, variations in W_m reflects either changes in the post spacing on the surface or the channel wall spacing. According to its definition (Eq. 1.7), an increased value of W_m implies a large value for W and/or a small value for D_h. The effect of these quantities on fRe is shown in Fig. # 5.33 for the Couette-flow scenario at $Re = 1$ and $F_c = 0.15$, 0.95, and 0.999. For the Couette-flow scenario, similar behavior to the one presented in Fig. # 5.18 is observed and is evident in the figure below. For all three $\boldsymbol{F_c}$ values, fRe tends to decrease as W_m is increased. Large W_m implies either very short channels or large post/cavity widths W. For small values of W_m, the frictional resistance fRe increases for each $\boldsymbol{F_c}$. Although fRe must approach the value of 32 for

the classical channel flow as $W_m \rightarrow 0$, the data reveal that at $F_c = 0.999$, *fRe* is nominally 28% of 32 at $W_m = 0.1$. Conversely, for the $F_c = 0.75$ case, the *fRe* value at $W_m = 0.1$ is nearly 32.

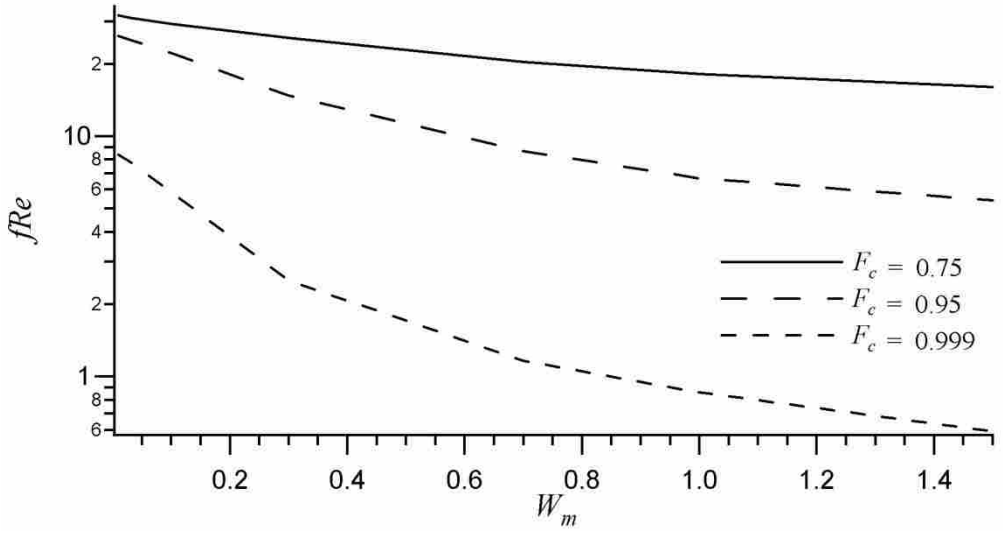

Figure 5.33: Dependence of *fRe* as a fraction of W_m for a superhydrophobic surface exhibiting square micro-posts in Couette flow at *Re* = 1 for three different F_c.

On the other hand, at higher values of W_m ($W_m > 0.6$) the *fRe* is asymptotically leveling off. At $F_c = 0.75$ the *fRe* graph levels off at higher values of W_m than the graphs of higher F_c. These observations can be expressed in a more practical manner, for instance, as $W_m \rightarrow 0$ there is vanishingly small frictional resistance reduction, and the superhydrophobicity of the surface has minimal influence specifically at lower cavity fractions. From the definition of W_m very tall channels exhibit that characteristic. In such a scenario, most of the liquid is very far from the surface and the cavity region on the surface cannot impose a strong effect on the liquid flow. From another perspective, W_m will also approach zero when *W* decreases significantly. From Fig. # 1.5, that occurs when both the combined solid and the cavity width decreases, which is the case for a superhydrophobic surface with a very high density structure. Such a phenomenon is expected, because as the surface structure density increases, the influence of cavity regions

diminish, resulting in a surface without any structure. According to Fig. # 5.33, reducing the channel height results in a more substantial decrease in *fRe*. It should be noted that at large values of *W* the channel pressure could easily exceed the Laplace pressure, making the surface susceptible to wetting. It is also important to point out that over the range of $0.01 \leq W_m \leq 1.5$ the reduction in *fRe* was about 16 (50%) at $F_c = 0.75$, 20 (77%) at $F_c = 0.95$, and 7.5 (93%) at $F_c = 0.999$, indicating a more pronounced influence of W_m on *fRe* at high cavity fractions.

Figure 5.34 illustrates how streamwise slip velocity varies along the post/cavity centerline at $W_m = 0$. In each case the slip velocity over a cavity increases from zero at the edge of a post to a maximum at the mid section of the channel and back to zero near the edge of another post. Also, as W_m is increased the slip velocity increases. That could occur when D_h is decreased. At lower values of W_m the increase in slip velocity is higher relative to scenarios with greater values of W_m. For instance, at streamwise point 0.4 there is about 400% increase in the apparent slip velocity as W_m is increased from 0.01 to 0.1. Whereas, when W_m is increased from 0.3 to 1.0, the increase in slip velocity is approximately 15%.

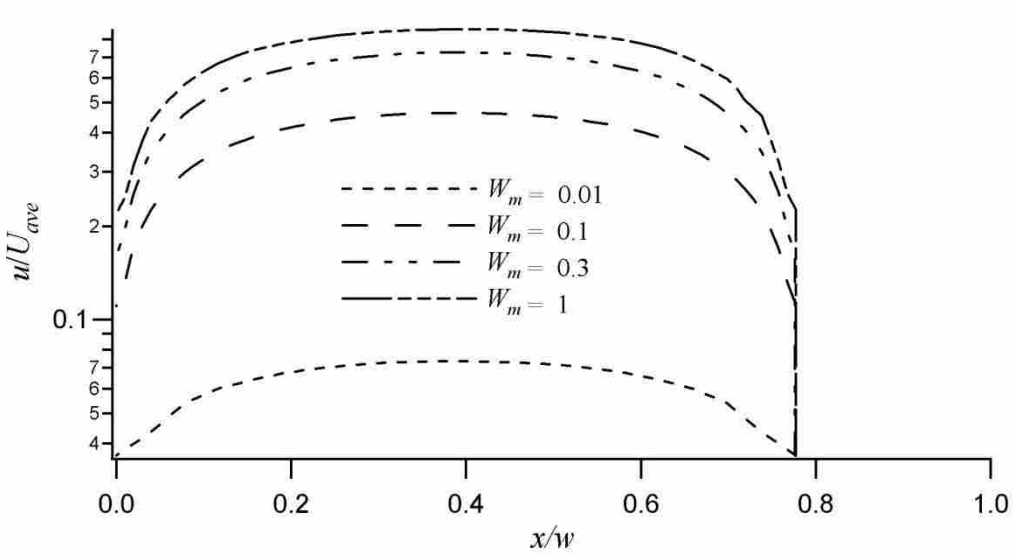

Figure 5.34: Normalized streamwise velocity variation along the cavity/post centerline at y = 0 for a Couette flow over a superhydrophobic surface exhibiting square micro-posts at

It was discovered that the slip length in liquid flow on superhydrophobic surfaces is independent of the driving force, even though, the slip velocity in pressure-driven flow is greater than the Couette flow. This difference in the slip velocities was directly related to the average wall shear stress being greater in the pressure-driven flow than in the Couette-flow scenario. The reason for such a difference in average wall shear stresses between the two flow scenarios is that the wall-normal velocity gradients are quite different. However, the slip length is strongly dependent on the surface geometry of the superhydrophobic surfaces. The *fRe* in both types of flow has similar dependence, but different in magnitude, on F_c and W_m. The influence of F_c was much greater for the pressure-driven flow than it was for the Couette flow. Only at extremely high values of cavity fraction, as $F_c \rightarrow 1$, there is not a significant difference in the two flow types of flow as far as the cavity fraction dependence is concerned.

Phase (2) of the current study suggests that influences of F_c and W_m on *fRe* observed in Couette flow cases are similar to the pressure-driven flow scenarios. The important result was

that the apparent slip lengths were exactly the same for both driving forces. However, the pressure-driven flow cases had greater slip velocities than the Couette flow scenarios throughout the entire F_s range. At very high cavity fractions as $F_c \rightarrow 1$, the effect of the driving force vanishes.

5.3 Pressure-Driven Flow with Rectangular Micro-Posts

In sections 5.1 and 5.2 the effects of two different driving forces on liquid laminar flow through micro-channels with square post patterned superhydrophobic surfaces were presented. The obtained 3-D numerical results indicated a strong relationship between the amount of liquid-solid interface and the frictional resistance reduction. The solid surface geometry is also an important parameter to consider. Even though various types and shapes of micro-posts have been studied by other scholars, rectangular posts and their effects on frictional resistance reduction have not been considered. This section includes the 3-D numerical results of a study conducted on a fully developed pressure-driven liquid laminar flow through a micro-channel consisting of rectangular micro-post patterned surfaces. Scenarios at $Re = 1$ and $W_m = 0.1$ with two F_c values of 0.75 and 0.95, were explored. As explained in Sec.4.2.3, the aspect ratio AR for the rectangular posts was defined as the ratio of the length (post dimension parallel to the flow) to the width (post dimension transverse to the flow) as shown in Fig. # 4.2. For the numerical models, aspect ratios AR of 1/8, 1/4, 1/2, 2, 4, and 8 were used at each F_c to examine the effects of post geometry on the overall flow and friction reduction. The numerical analysis was conducted in two phases: phase (1) corresponded to AR = 2, 4, and 8 and phase (2) corresponded to AR = 1/8, 1/4, and 1/2. Each phase consisted of two scenarios, $F_c = 0.75$ and 0.95.

5.3.1 Rectangular Posts Oriented Parallel to the Flow

The first phase of this part of the study consisted of rectangular micro-posts with *AR* = 2, 4, and 8 as shown in Fig. # 4.2a. In order to distinguish between the two phases, these cases are referred to as parallel orientation to the flow. It is also important to point out that the relative module width for this phase was defined as $W_m = W/D_h$, where *W* was equal to the total post/cavity width perpendicular to the direction of flow. The results for two scenarios F_c = 0.75 and 0.95 are presented in Figs.5.35 and 5.36, respectively. The variation in *fRe* with respect to *AR* for F_c = 0.75 is shown in Fig 6.35. Also included in the figure are longitudinal rib results at F_c = 0.75 (dashed line) and the classical no-slip channel flow. It can be seen that as the *AR* increases the *fRe* value approaches the results (solid line). The behavior is completely expected, with increasing *AR* leading to an increase in *fRe*, since the upper limit as $AR \rightarrow \infty$ is longitudinal ribs. However, with regard to frictional resistance reduction, the rectangular posts yield significantly smaller values of *fRe* than the longitudinal ribs at low aspect ratios. For instance, the longitudinal rib results show a 27% reduction in *fRe* compared with the no-slip channel flow, whereas the rectangular post with *AR* = 2 results in a nominal 38% decrease in *fRe*. Care must be taken, however, about making the general conclusion that at low *AR* all rectangular micro-posts result in greater reduction in frictional resistance. This result can be misleading unless spacing and arrangement of the posts and the ribs is also considered before making such a general conclusion. Of course, if reduction in overall frictional resistance were the primary concern, one could infer that the rectangular posts, as presented in Fig. # 5.35, outperform the longitudinal ribs. It is important to note that the results in Fig. # 5.13 showed at this cavity fraction (F_c = 0.75) the square micro-posts actually had a larger value for *fRe* than the longitudinal rib scenario. The logical explanation for such results is that different spacing between square posts (See Fig. #

4.1) was implemented in the numerical models than in the rectangular-post scenarios. In order to accommodate high aspect ratios, the rectangular posts had to be arranged farther apart than the square posts. This was necessary to maintain the same cavity fraction F_c and relative module width W_m values. The amount of liquid/vapor contact surface has an extremely important impact on the frictional resistance reduction. Thus the mentioned scenarios cannot be directly compared.

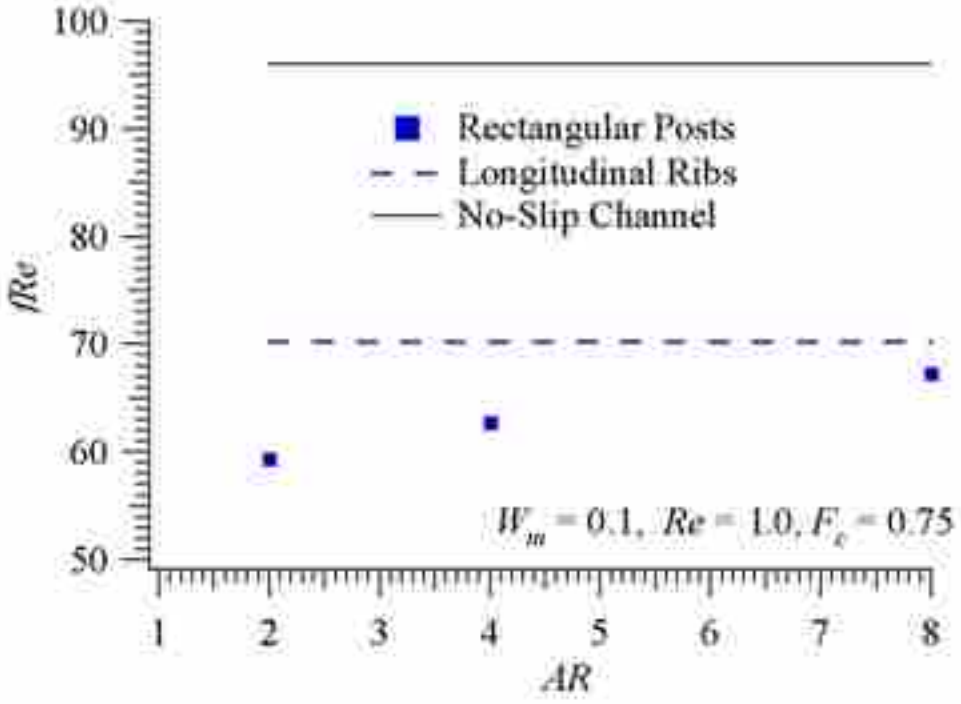

Figure 5.35: *fRe* as a function of *AR* for a pressure-driven flow over a superhydrophobic surface exhibiting rectangular micro-posts oriented parallel to the direction of the flow at $Re = 1$, $F_c = 0.75$, and $W_m = 0.1$. Longitudinal ribs and no-slip channel results are

Similar numerical analysis was performed for rectangular micro-posts at $F_c = 0.95$ and the results are illustrated in Fig. # 5.36. The *fRe* values of both the rectangular posts and the longitudinal ribs are less than the $F_c = 0.75$ case, as expected. As the *AR* increases the *fRe*

product also increases and similar to the F_c = 0.75 data, it approaches the longitudinal rib results for F_c = 0.95.

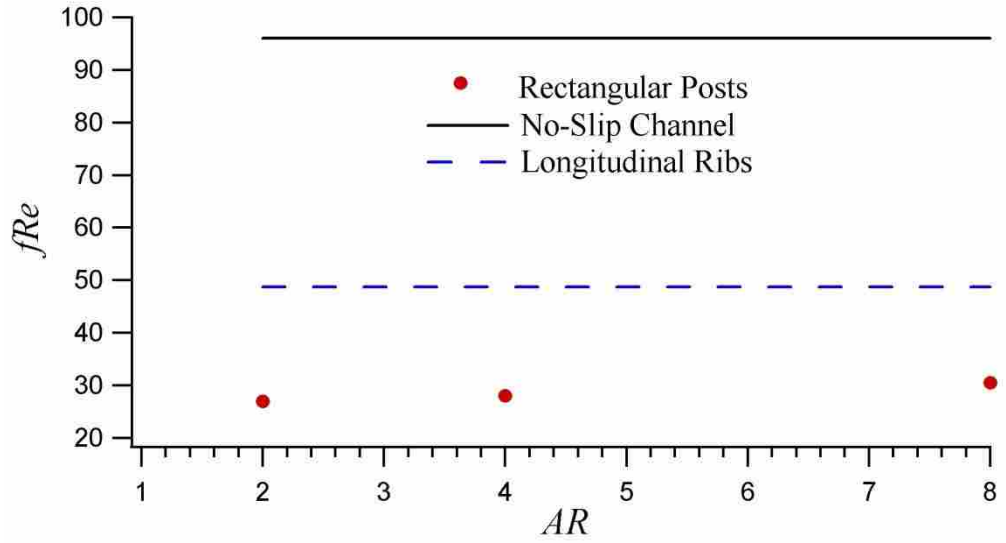

Figure 5.36: *fRe* as a function of *AR* for a pressure-driven flow over a superhydrophobic surface exhibiting rectangular micro-posts oriented parallel to the direction of the flow at *Re* = 1, F_c = 0.95, and W_m = 0.1. Longitudinal ribs and no-slip channel results are

However, the asymptotic approach at F_c = 0.95 to the longitudinal rib scenario occurs at a more moderate rate than the F_c = 0.75 scenario. This result is also not unexpected, since at high cavity fractions all influencing parameters on the frictional resistance reduction increase.

5.3.2 Rectangular Posts Oriented Transverse to the Flow

The phase (2) was comprised of two scenarios F_c = 0.75 and 0.95 each using *AR* = 1/8, 1/4, and 1/2. In order for the graphs to be consistent with phase (1) it was decided to use *AR* = 2, 4, and 8 for these scenarios while changing the direction of the liquid flow 90º with respect to the flow in phase (1). These two scenarios were referred to as the transverse rectangular posts. The relative module width for this phase was also defined as $W_m = W/D_h$, but here *W* was equal to the

total post/cavity width parallel to the direction of flow. The results are presented graphically in Fig. # 5.37 along with the results of transverse micro-ribs and the no-slip channel flow.

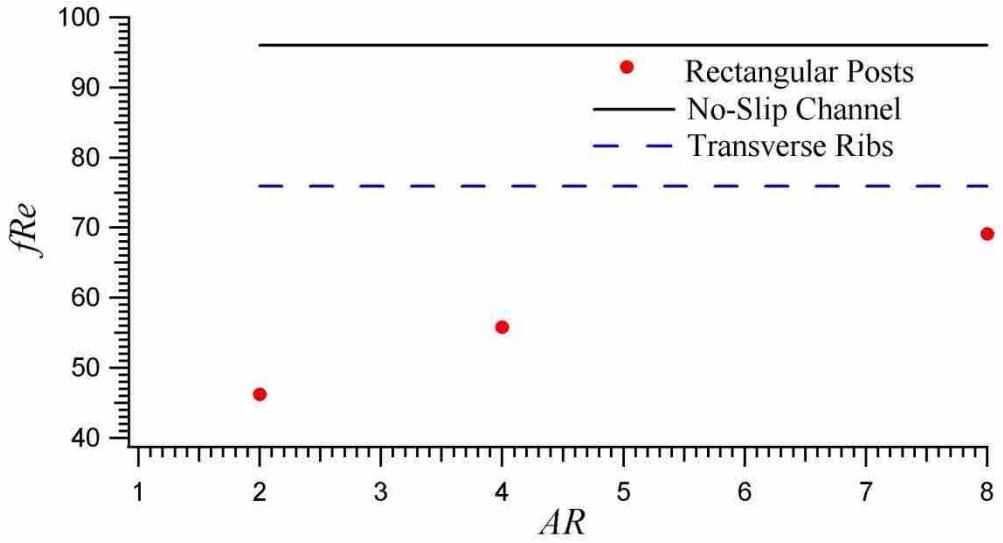

Figure 5.37: *fRe* as a function of *AR* for a pressure-driven flow over a superhydrophobic surface exhibiting rectangular micro-posts oriented transverse to the direction of the flow at $Re = 1$, $F_c = 0.75$, and $W_m = 0.1$. Transverse ribs and no-slip channel results are shown for comparison.

The behavior and general relationship between *fRe* and *AR* manifested here are very similar to those shown in Fig. # 5.35. Regarding frictional resistance, the rectangular micro-post performance becomes similar to the micro-ribs at high *AR*.

The result of the second scenario of the phase (2) was obtained at $F_c = 0.95$ and is illustrated in Fig. # 5.38. Included in this figure are the *fRe* values for the transverse micro-ribs and the no-slip channel flow. In this situation also the rectangular micro-posts approach the transverse ribs in performance with regard to frictional resistance.

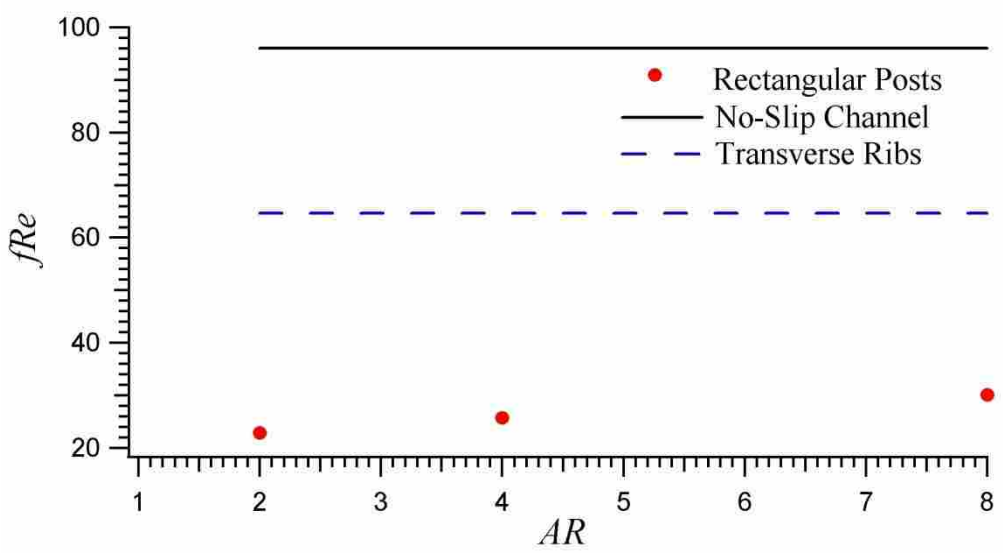

Figure 5.38: *fRe* as a function of *AR* for a pressure-driven flow over a superhydrophobic surface exhibiting rectangular micro-posts oriented transverse to the direction of the flow at $Re = 1$, $F_c = 0.95$, and $W_m = 0.1$. Longitudinal ribs and no-slip channel results are shown for comparison

Similar to the parallel rectangular micro-posts, this approach occurs at a lower rate compared with the previous scenario in which $F_c = 0.75$. At high F_c the micro-posts in general outperform the micro-ribs. As it was pointed out in Fig. # 5.13; at $F_c \geq 0.88$ micro-posts, in general, show increased reduction in frictional resistance than micro-ribs.

To recapitulate the phase (3) of this study, 3-D numerical solutions were obtained for liquid laminar flow through a channel with rectangular post patterned walls. Simulations were performed at $Re = 1$, $F_c = 0.75$ and 0.95 with the aspect ratios $AR = 1/8$, 1/4, 1/2, 2, 4, and 8. The results indicated that as the post *AR* is increased the effect of the superhydrophobic surfaces exhibiting rectangular posts on the frictional resistance reduction approaches those of the surfaces with rib configuration. When the liquid flow direction is parallel to the long side of the rectangular posts and as the *AR* increases, these effects become similar to those of the longitudinal ribs. On the other hand, as *AR* increases, while the liquid flow direction is

perpendicular to the long side of the rectangular posts, the results approach those of the transverse ribs.

6 CONCLUSIONS

A comprehensive numerical analysis of liquid laminar flow through micro-channels with non-wetting micro-post patterned superhydrophobic surfaces has been conducted in this study. A total of 144 independent scenarios were modeled using a classical Navier-Stokes CFD approach. The non-wetting, or Cassie state, is achieved when the channel pressure does not exceed the Laplace pressure and this state was assumed in this work. The research was conducted in three phases and for all scenarios the liquid vapor interface over the cavities was presumed to be flat with the Cassie state prevailing. Phase one consisted of pressure-driven laminar flow through channels with superhydrophobic walls exhibiting square micro-posts. In this phase the influence of the channel Reynolds number was also explored. Phase two addressed shear-driven laminar flow through channels with square post patterned superhydrophobic surfaces in the creeping flow regimes $Re \approx 1$. The last phase addressed pressure-driven channel flow with the superhydrophobic surfaces exhibiting rectangular posts.

The results suggest a strong relationship between the cavity fraction and frictional resistance reduction for all scenarios. In the case of pressure-driven creeping flow ($Re \approx 1$) over square post patterned walls, the results were similar to those found in the literature for rib patterned surfaces [14, 15]. The effect of cavity fraction F_c on the friction factor Reynolds number product fRe was investigated over the range of $0.0 \le F_c \le 0.9998$. As F_c increased the fRe decreased moderately for $0.0 \le F_c \le 0.88$, but a more siginificant decrease in fRe was

observed for $0.88 \leq F_c \leq 0.9998$. Careful examination of streamwise velocity contours at the superhydrophobic surface and streamwise velocity profiles normal to the surface provided an excellent view of physical variations in the velocity field. Slip flow prevails above the cavity regions at the surface of the channel, and the overall effect is apparent slip at the plane of the wall. The apparent slip velocity was obtained from the numerical results for all scenarios after which the apparent slip length λ was calculated. The results indicated that both the apparent slip velocity and the apparent slip length were directly affected by the cavity fraction. At large values of F_c greater apparent slip velocity and slip lengths were observed. Analysis of the average shear stress τ_w at the channel walls and its variation at the liquid solid interface on the post surfaces indicates a direct correlation between wall shear stress and cavity fraction. As the cavity fraction increased the average shear stress on the solid surface also increased. This increase in shear stress was very significant at very high F_c. Generally, a sharp peak in shear stress was observed along the edges and on the corners of the posts for all scenarios. Large velocity gradients are responsible for the high shear stress quantities at the edges and corners of the post surfaces. Since the overall drag force exerted by the liquid on the channel wall acts on a smaller area of solid as the post size decreases, the average shear stress on the post increases in magnitude. It was also observed that a net reduction in the average wall shear stress on the entire superhydrophobic surface (post and cavity) occurs and this is responsible for the decrease in overall frictional resistance (Eq. 3.6). The liquid flowing over the superhydrophobic surface experiences a vanishing shear stress at the liquid vapor interfaces giving rise to local regions of slip. It is the reduction in the average wall shear stress on superhydrophobic surfaces that is ultimately responsible for the decrease in the surface friction. For a relative module width of W_m

= 0.1 and *Re* = 1, the frcition factor Reynolds number product *fRe* was observed to decrease by 21% at F_c = 0.75, by 55% at F_c = 0.95, by 78% at F_c = 0.99, and by 97% at F_c = 0.9998.

The relative module width W_m was also shown to have a considerable influence on the overall reduction in frictional resistance for the pressure-driven creeping flow cases. An important result obtained from this study was that the slip length is independent of the relative module width and is only a function of the cavity fraction. Over the range of $0.01 \leq W_m \leq 1.5$, the results indicated that as $W_m \rightarrow 0$ the slip velocity, and the frictional resistance reduction decreased markedly. Such a result implies a reduction in the effectiveness of superhydrophobicity of the surface at very small values of W_m. From the definition of W_m, it can be inferred that for large values of hydraulic diameter D_h the reduction in frictional resistance provided by superhydrophobic surfaces diminishes. Thus, the use of superhydrophobic surfaces appears to be ineffective for macroscale channels, even if wetting is avoided. However, much different results were obtained at large values of W_m. For all cavity fractions ($0.0 \leq F_c \leq 0.9998$) considered, as W_m was increased the frictional resistance consistently decreased. It was concluded that as D_h is decreased, the superhydrophobic surfaces in channels yields a much greater effectiveness in reducing the overall frictional resistance. In other words, micro or nano-scale channels with post patterned superhyrophobic surfaces and high cavity fractions are the most effective in reducing the overall frictional resistance. At F_c = 0.95 the *fRe* decreases from the classical value by 92% for W_m = 1.0, by 55% for W_m = 0.1, and by 11% for W_m = 0.01. The results indicated that the apparent slip length is completely independent of W_m. According to the literature [27], the apparent slip length is only a function of F_c for parallel ribs, but it is dependent on both F_c and *Re* (over a limited range) for transverse ribs [14, 17]. In this regard, the slip length results from the present study for square posts were similar to the transverse ribs.

Since the available results in the literature were limited to $Re \leq 1$, the present study was extended to include a wide range of Reynolds number in the laminar flow regime, $1 \leq Re \leq 2500$. Previous investigators have shown that *fRe* for surfaces with longitudinal ribs is independent of *Re*, whereas significant dependence on Reynolds number for transverse ribs at $Re \geq 40$ has been reported. The present results for posts indicate very similar conclusions to transverse ribs. The *fRe* is unaffected by the Reynolds number for $Re \leq 40$ at all values of F_c and $W_m \leq 0.1$. At all values of *Re*, a more significant reduction in *fRe* was observed at large values of both F_c and W_m. In flow regimes with $Re \geq 40$, and especially as the flow approaches the transitional regime (Re = 2500) *fRe* was observed to increase with increasing *Re*. However, the rate of increase was observed to be less than previously observed for transverse ribs. This result indicates that superhydrophobic surfaces lose some of their effectiveness in reducing frictional resistance at very high Reynolds numbers. When the relative module width W_m was increased by a factor of 10 from 0.1 to 1, the influence of *Re* on *fRe* became more significant and departure from creeping flow behavior began to occur at $Re \approx 4$, as compared to $Re = 40$ for the $W_m = 0.1$ scenario.

For the Couette flow scenarios the influences of F_c and W_m were found to yield similar results as for pressure-driven flow scenarios. Namely, as F_c and W_m increase the frictional resistance on the superhydrophobic surface with micro-post configurations decrease. Also, *fRe* approached the classical Couette flow value of 32 when $W_m \rightarrow 0$ and $F_c \rightarrow 0$. Some significant differences between pressure-driven and Couette flow scenarios were observed. The results showed no discernable difference between the apparent streamwise slip for the prssure driven and the Couette flow scenarios, where greater apparent slip velocities exist for the pressure-driven flow than for Couette flow. A maximum difference of approximately 20% was obtained

between the normalized apparent slip velocities at $W_m = 0.1$ and $Re = 1$. The fact that the slip length of the channel surfaces was shown to be nearly identical for the two scenarios has been published before; however, no comprehensive study has proved this to be the case prior to this work.

Upon comparison of the results for the pressure-driven flow with rectangular post patterning and previously obtained results for rib patterning, it was determined that as the aspect ratio of the posts increased the results approached those reported for ribs. When the flow was perpendicular to the long side of the posts and as the post aspect ratio increased, the frictional resistance approached the transverse rib results. Similarly, when the liquid flow direction was parallel to the long side of the posts the *fRe* results approached the longitudinal rib results as the post aspect ratio increased.

6.1 Recommendations for Future Work

Future studies related to this topic could include a greater range of relative module width W_m in order to obtain more comprehensive results in both the pressure-driven and the Couette flow scenarios. The effectiveness of micro-posts with rounded edges and corners on reducing the peak values in the local wall shear stress could be investigated for both flow scenarios. Analyzing the effect of the cavity depth would be another important contribution to the literature. Of course, the cavity depth influence can be investigated only when the vapor in the cavity is modeled in the analysis. Since the present study assumed zero shear stress at the liquid vapor interface, implementation of the liquid-vapor cavity coupled model at the interface would quantify the accuracy of this assumption. Application of a non-flat liquid vapor interface by

taking into account the formation of meniscus is also recommended for comparative purposes. A more comrehensive exploration of the rectangular post geometry is also recommended.

REFERENCES

[1] **Woolford B. L.** Laminar and turbulent flow of a liquid through channels with superhydrophobic walls exhibiting alternating ribs and cavities, Brigham Young University, Provo, 2009.

[2] **Davies J.** Analysis of viscous drag reduction and thermal transport effects for microengineered ultrahydrophobic surfaces. *Brigham Young University*, Provo, 2006.

[3] **Chen W, Fadeev AY, Hsieh MC, Oner D, Youngblood J, and McCarthy JT.** Ultrahydrophobic and Ultralyophobic Surfaces: Some Comments and Examples. *Langmuir* 15, 3395-3399 (1999).

[4] **Dupuis A. and Yeomans J. M.** Modeling droplets on superhydrophobic surfaces: Equilibrium states and transitions. *Langmuir* 2005, 21, 2624-2629.

[5] **Kim J and Kim CJ.** Nanostructured surfaces for dramatic reduction of flow resistance in droplet-based microfluidics. *The 15th IEEE International Conference on Micro Electro Mechanical Systems* 479-482, 2002.

[6] **Oner D and McCarthy TJ.** Ultrahydrophobic Surfaces: Effects of Topography Length Scales on Wettability. *Langmuir* 2000: p. 7777-7782.

[7] **Zhu L, Feng Y, Ye X, and Zhou Z.** Tuning wettability and getting superhydrophobic surface by controlling surface roughness with well-designed microstructures. *13th International Conference o Solid-State Sensors, Actuators and Microsystems* 1481-1484, vol.2, 2005.

[8] **Miwa M., Nakajima A., Fujishima A., Hashimoto K., and Watanabe T.** Effects of the surface roughness on sliding angles of water droplets on superhydrophobic surfaces. *Langmuir*, 16. 5754-5760, 2000.

[9] **Philip JR.** Flows satisfying mixed no-slip no-shear conditions. *Z. Angew. Math. Phys.* 23, 353, 1972.

[10] **Lauga E and Stone H.** Effective slip in pressure-driven Stokes flow. *Journal of Fluid Mechanics* 489: 55-77, 2003.

[11] **Ou J, Perot B, and Rothstein J.** Laminar drag reduction in microchannels using ultrahydrophobic surfaces. *Physics of Fluids* 16: 12: 4635-4643, 2004.

[12] **Ou J and Rothstein JP.** Direct velocity measurements of the flow past drag-reducing ultra-hydrophobic surfaces, *Physics of Fluids* 17, 103606, (2005).

[13] **Choi CH, Ulmanella U, Kim J, Ho CM, Kim CJ.** Effective slip and friction reduction in nano-grated super-hydrophobic micro-channels. *Physics of Fluids* 18:087105, 2006.

[14] **Davies J, Maynes D, Webb B, and Woolford B.** Laminar flow in a microchannel with superhydrophobic walls exhibiting transverse ribs. *Physics of Fluids* 18: 8: 7110-1-7110-11, 2006.

[15] **Maynes D, Jeffs K, Woolford B, and Webb B.** Laminar flow in a microchannel with hydrophobic surface patterned microribs oriented parallel to the flow direction. *Physics of Fluids* 19: 9: 3603-1-3603-12, 2007.

[16] **Sbragaglia M. and Prosperetti A.** A note on the effective slip properties for microchannel flows with ultra-hydrophobic surfaces. *Physics of Fluids*, 2006.

[17] **Woolford B, Maynes D, and Webb BW.** Liquid flow through micro-channels with grooved under wetting and super-hydrophobic conditions. Microfluid Nanofluid Flow Journal, DOI 10.1007/s10404-008-0365-6, 2008.

[18] **Teo C. J. and Khoo B. C.** Analysis of Stokes flow in microchannels with superhydrophobic surfaces containing a periodic array of micro-grooves. *Microfluidics and Nanofluidics*, 7: 353-382, 2008.

[19] **Cheng Y. P., Teo C. J., and Khoo B.C.** Microchannel flows with superhydrophobic surfaces: Effects of Rey and pattern width to channel height ratio. *Physics of Fluids* 21,122004, 2009.

[20] **Gao P. and Feng J. J.** Enhanced slip on a patterned substrate due to depinning of contact line. *Physics of Fluids*, 21, 102102, 2009.

[21] **Choi CH and Kim CJ.** Large slip of aqueous liquid flow over a nano-engineered super-hydrophobic surface. *Physical Review Letters 96:6:6001-1-6001-4, 2006.*

[22] **Salamon T, Lee W, Krupenkin T, Hodes M, Kolodner P, Enright R, and Salinger A.** Numerical simulation of fluid flow in microchannels with super-hydrophobic walls. *Proceedings of the ASME Heat Transfer Division* 376: 819-829, 2005.

[23] **Ybert C, Barentin C, Cottin-Bizonne C, Joseph P, and Bocquet L.** Achieving large slip with superhydrophobic surfaces: Scaling laws for generic geometries. *Physics of Fluids* 19:12: 3601-1-3601-10, 2007.

[24] **Lee C, Choi CH, and Kim CJ.** Structured surfaces for giant liquid slip. *Physical Review Letters* 101: 064501, 2008.

[25] **Ng C. and Wang C. Y.** Apparent slip arising from Stokes shear flow over a bidimensional patterned surface. Microfluid Nanofluid, 8:361-371, 2009.

[26] **Govarhan R. N., Sinivas G. S., Asthana A., and Bobji M. S.** Time dependence of effective slip on textured hydrophobic surfaces. *Physics of Fluids*, 21, 052001, 2009.

[27] **Jeffs K. B**. Numerical study of fully developed laminar and turbulent flow through microchannels with longitudinal microstructures, *Brigham Young University*, Provo, 2007.